UNIVERSITY OF SOUTHAMPTON

FACULTY OF ENGINEERING AND THE ENVIRONMENT

Computational Engineering and Design Group

Mechanics of structured materials and their biomedical applications

by

Alessandra Bonfanti

Thesis for the degree of Doctor of Philosophy

10th December 2016

UNIVERSITY OF SOUTHAMPTON

ABSTRACT

Doctor of Philosophy

MECHANICS OF STRUCTURED MATERIALS AND THEIR BIOMEDICAL APPLICATIONS

by Alessandra Bonfanti

This work is concerned with the mechanics of periodic structures for biomedical applications. Classical work on the apparent elastic properties of infinite planar and cylindrical lattice structures is generalised to the non-linear elasto-plastic regime. The elastic recoil upon unloading is also assessed. Elastic instability behaviour of constrained perforated films upon stretching is studied.

The elasto-plastic response and recoil analysis of two-dimensional honeycomb is presented. The apparent non-linear structural response obtained analytically here is observed to be smooth, even though the material model of the constituent material is elastic-perfectly-plastic. We show that the Poisson's ratio in the non-linear deformation remains the same as that during the elastic phase. A non-trivial scaling transformation for apparent stress and strain, which separates the individual cell wall response from the mechanics of the overall honeycomb sheet, is identified. This leads to a non-linear master deformation profile that fully describes the plastic response of hexagonal honeycomb with different geometries. The effects of material hardening are introduced by using a novel hyperbolic hardening model. This is then generalised for lattices whom struts possess circular cross-section. Such analysis is relevant to lattice materials and scaffolds manufactured using 3D printing techniques, such as fused deposition modelling, that inevitably makes use of cylindrical filaments.

Analytical expressions for the elasto-plastic response of a sinusoidal structure wrapped over a cylinder, as a model of crown found within cardiovascular stents, is developed. The response of the cylinder under internal pressure is well approximated by that of the opened-up flattened configuration under remote stretch. A scaling ansatz that collapses the response for different geometries on a family of 'master-curves' is proposed. We show that the stiffness scales as the cube of the ratio between the amplitude and the wavelength of the sinusoid. Such analysis is then successfully applied to the development of two novel biodegradable stents.

Thin membranes with positive apparent Poisson's ratio wrinkle when stretched. Here we show that membranes with negative apparent Poisson's ratio are wrinkle-free upon stretching, except at the edges where localised wrinkling occurs. Here we develop a simple analytical kinematic model to characterise the amplitude and wavelength of the instability behaviour. The model is then validated experimentally and computationally.

Contents

List of Figures

List of Tables

Declaration of Authorship

I, Alessandra Bonfanti , declare that the thesis entitled *Mechanics of structured materials and their biomedical applications* and the work presented in the thesis are both my own, and have been generated by me as the result of my own original research. I confirm that:

- this work was done wholly or mainly while in candidature for a research degree at this University;
- where any part of this thesis has previously been submitted for a degree or any other qualification at this University or any other institution, this has been clearly stated;
- where I have consulted the published work of others, this is always clearly attributed;
- where I have quoted from the work of others, the source is always given. With the exception of such quotations, this thesis is entirely my own work;
- I have acknowledged all main sources of help;
- where the thesis is based on work done by myself jointly with others, I have made clear exactly what was done by others and what I have contributed myself;
- parts of this work have been published as: [1; 2]

Signed:.....

Date:.....

Acknowledgements

First and foremost I want to thank my supervisor Prof. Atul Bhaskar. It has been an honour to work with him during these years. He has taught me the *beauty of simple analytical analysis* to explain real complex phenomena. I would like to express my gratitude for his continued and enthusiastic support, for his patience, motivation and insightful comments. His hard-hitting criticisms and discussions have always been thought-provoking and extremely rewarding–although difficult to accept at the beginning. His advice on both research as well as on my career has been of great value. I would also like to thank Dr. Stavors Syngellakis, my co-supervisor, who has always been supportive. His guidance and encouragement helped me during the difficult times. Moreover, I am thankful for his constructive criticism during the writing of this thesis.

Beside my advisor, I would like to thank the ReBioStent consortium for their support and the opportunity to work with them on a really exciting and challenging problem. My sincere thanks also goes to Dr. Christophe Lecomte who supported me in the moments I felt discouraged or confused. His recommendations have been precious and I am grateful to his valuable comments on this thesis. I would also like to thank everyone at Computational Engineering and Design Group who are first friends, and secondly colleagues, for providing me a once-in-a-lifetime experience that I will carry with me forever.

A special thanks to my family. Foremost to my mother and father for all the sacrifices that you have made without which I would have not been able to achieve this result. I would also like to thank my sister for supporting me in the moments when there was no one to answer me or no one to understand the difficulties of this adventure.

Chapter 1

Introduction

Material arrangement has important implications to the response of structures. This motivates the study of matter with controlled architecture. Structures and materials with regular internal space configuration are frequently used in engineering (see figure 1.1 for example). Structures that show geometric periodicity include trusses and grillages, bridges, frameworks, supports for power transmission cables, etc. Sandwich constructions in aeronautical applications frequently use honeycombs in their core; they are designed to resist shear deformation. Several other materials such as those used in electromechanical sensors, automotive catalytic converters, as well as in impact and sound absorption applications [3; 4] make use of the cellular and porous internal geometry for specific functions. With the advent of acoustic meta-materials[1], the promise of tailoring acoustic waves has opened new possibilities in the area of structured materials [5]. In addition, their energy absorption capability makes them suitable for crashworthiness applications, such as helmets and sport protections [3]. More recently, scaffolds are used for biomedical implants, such as those for hip replacement, because they stimulate cell growth. Due to the wide use of such lattice and periodic structures, a sound understanding of their mechanical behaviour is critical for their design and holds the key to their industrial future. Here, a general overview of lattice materials and their application to biomedicine is introduced.

1.1 Cellular and lattice materials

Conventionally, in civil engineering, *lattice* refers to an array of trusses or frames pin-joined or rigidly connected to create a stiff structure with the least amount of material [12]. In crystallography, a lattice is a periodic arrangement of atoms, ions or molecules

[1] Materials that show properties unavailable in nature. With their unique arrangement, electromagnetic waves can be manipulated by blocking, absorbing or bending them to achieve benefits unattainable with conventional materials.

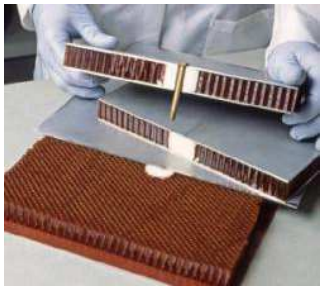

(a) Sandwich pannels [6]

(b) Wing of 3D printed UAV [7]

(c) Stretchable electrode [8]

(d) Airless tires [9]

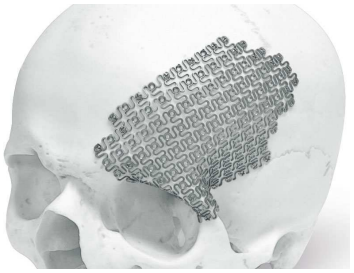

(e) Cranioplasty mesh [10]

(f) Cardiovascoular stents [11]

Figure 1.1: Examples of aeronautical, mechanical, electronic and biomedical structures with regular internal architecture.

in 3D [13]. There is a flurry of activities in the area of 2D lattices following the discovery of carbon nanotubes and graphene. Here, we are concerned with lattice *structures* or cellular *materials*. Like civil structures and crystals, they consist of an assembly of interconnected slender beams or plates repeated in the space. Lattice materials differ from the conventional engineering trusses and frames on account of their length scale. When the macroscopic length scale is comparable to that of the unit cell of the lattice, structural mechanics can be applied to analyse the *structure*. However, when the unit cell is much smaller than the macroscopic dimensions, the lattice structure behaves as a material. Its behaviour can be analysed using classical structural mechanics and it can be treated as homogeneous fully dense matter characterized by its own *effective* properties [12; 14].

Several materials show internal microstructure consisting of voids and slender beams randomly or periodically interconnected, commonly called struts. They are referred to as cellular materials–or foams, if they do not show regularity, or lattices if they are made of a unit cell that is translationally repeated in space. Foams can be classified into two types: *open*-cell or *closed*-cell. In an open-cell foam, the edges of the cell are the only solid part, whilst a closed-cell foam has solid membranes over the faces. In open-cell foams, voids are interconnected whereas in closed-cell foams, they are separated by the membranes. The main factors that dominate their mechanical properties are: (i) the constituent material of which the foam is made, (ii) the connectivity–or topology–of cell edges and faces, which is given by the number of struts joining at one node, and (iii) the

relative density $\overline{\rho}$–which is the volume fraction of the solid in the material–given by the ratio between density of the lattice and that of the corresponding solid [12]. Their main advantage lies in their high strength-to-density ratio. Therefore, while aiming to develop lightweight structures in several sectors, e.g. transport, aerospace, naval architecture and biomedical engineering [15–17], cellular materials have been extensively used.

The mechanical characterization of foams started long before that of lattice materials, because they are frequently found in nature, e.g. cork, bone, wood. Between the 1960s and 1970s, the first studies [18; 19] showed that most of the mechanical properties of foams do not linearly depend on the relative density. Since then, a large body of literature has been developed to enhance the understanding of mechanical, thermal and electrical properties of foams. The main results have been efficiently summarized and further extended in the monograph by Gibson and Ashby in *Cellular Solids* [3] and Ashby *et al.* in *Metal Foams: a Design Guide* [20]. Their primary aim was to apply the ideas developed for foams to the analysis of lattice materials with regular microstructure. Their findings lead to the conclusion that, by using a fixed amount of material, superior mechanical properties can be achieved by a regular lattice material, where the matter is systematically placed in space, compared to a material with a random internal configuration. As shown in figure 1.2, at the same value of relative density, both stiffness and strength of lattices are higher than those of foams.

Perhaps the most important concept in analysing the mechanical behaviour of periodic structures is the distinction between *stretch-* and *bending*-dominated architectures [12], which is based on the main deformation mechanism of the cell walls. Studies on open-cell foams have shown that cell walls mainly undergo bending deformation, as well as most of the closed-cell foams. Since cell faces buckle or rupture at low stress, cell edges carry most of the load; therefore, their behaviour resembles that of the open-cell configuration. Examples of lattice structures whose stiffness and strength are governed by the bending of the cell walls abound–for example, the benchmark honeycomb geometry. From beam theory [12], it follows that the effective Young's modulus $\langle E \rangle$ of the bending-dominated structure scales $\langle E \rangle \sim \overline{\rho}^{(2)} E_S$, where E_S is the Young's modulus of the constituent material. The yield strength of the structure $\langle \sigma_Y \rangle$ scales with the yield strength of the constituent material σ_Y according to $\langle \sigma_Y \rangle \sim 0.3\overline{\rho}^{(3/2)}\sigma_Y$. By contrast, when a triangulated 2D frame or a kinematically rigid 3D truss is loaded, the struts experience tensile or compressive loads; therefore, the topology is stretch-dominated [21]. The stiffness and strength of the stretch-dominated structures both linearly depend on the relative density, according to, $\langle E \rangle \sim 0.3\overline{\rho}E_S$ and $\langle \sigma_Y \rangle \sim 0.3\overline{\rho}\sigma_Y$ respectively. The linear dependence of $\langle E \rangle$ and $\langle \sigma_Y \rangle$ on the relative density for stretch-dominated structure is clearly captured by the material properties maps known as Ashby maps, plotted in figure 1.2. In contrast, stiffness and strength for bending-dominated structures degrade at a faster rate with a decrease in density. The topological criterion that dictates the

deformation mechanism of a cellular solid is the Maxwell's stability law[2], which is a necessary, but still not a sufficient condition to establish if a configuration is bending-dominated [21].

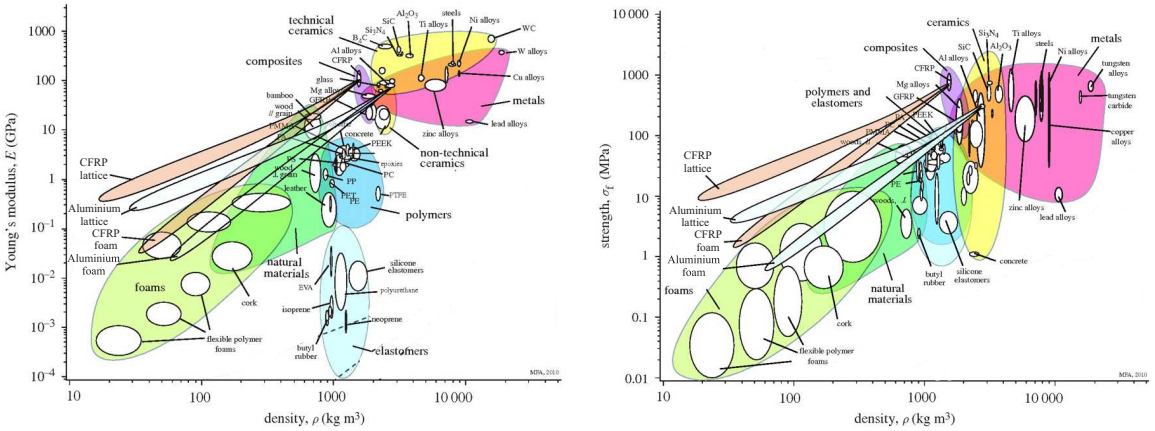

Figure 1.2: Bending-dominated foams and stretching-dominated lattice materials are displayed in property space–Ashby maps, using Young's modulus E and strength σ_f vs density ρ [14]. Bending-dominated foams and stretch-dominated lattices are plotted within more traditional materials. The two graphs show the linear dependence of E and σ_f on the density for lattices, in contrast with the non-linear dependence for bending-dominated foams.

The current knowledge on lattice materials mainly focuses on the linear elastic response and the calculation of the collapse point [3], thus the loading at which any further increment will cause the failure of the material. The next chapter exhaustively reviews the studies on their mechanical behaviour when subjected to pure elastic deformation. The transition between the yield point of the lattice, thus when the material has just undergone plastic deformation, and the final collapse is a non-linear structural problem. The non-linearity is introduced by the material constitutive relationship. The non-linear behaviour of structures is often analysed using numerical methods because only few non-linear systems that describe real problems can be solved analytically. Numerical methods construct successive approximations that converge to the exact solution; however, they still represent an estimate of the solution. The plastic response of lattice materials has been extensively studied both computationally, with the use of numerical approximation, and experimentally [22; 23]. However, no explicit and analytical solution has been derived yet. A lattice material that has undergone elasto-plastic deformation is such that it has permanently changed its shape. When the load is removed, the plastic deformation remains on the material, whilst the elastic part of the deformation is recovered. The structure tends to go back towards its initial configuration partially. This behaviour is well-known in the area of metal forming as elastic recoil or springback. However, it

[2] A statically and kinematically determinate pin-joined frame has $M = b - 2j + 3 = 0$, where b and j are respectively the number of struts and frictionless joints. If loaded, the members carry tension or compression; thus, the structure is stretch-dominated. When $M < 0$, the frame is a mechanism. If the joints are locked, the struts bend when loaded; thus, the structure becomes bending-dominated. [12]

has not been studied yet in the field of architectured materials, since it firstly requires the determination of the complete non-linear lattice response after yielding. Scaling relationships for the plastic response are still unknown and their identification is an important step while seeking a universal physical behaviour.

Bending-dominated materials possess lower stiffness than stretch-dominated architectures for the same relative density, but they can store a greater amount of energy [12]. This makes them suitable for crashworthiness applications, such as helmets and equipment for protection in sport [3]. When subjected to compressive load, bending-dominated structures linearly deform until the cell edges start yielding, following buckling or fracture. Beyond this, the structures accommodate large strain at an almost constant stress–known as "plateau region" of stress, until self-contact of cell walls occurs in the "densification phase" (see figure 1.3). When stretch-dominated structures are loaded beyond the yield point, struts start to buckle leading to a post-peak softening behaviour. While buckling has been mostly understood [24; 25], the post-yielding response of the cell edges needs to be taken up yet. This shows that the plastic analysis developed for lattice materials under tensile loading can be extended to the study of bending-dominated structures under compressive load, only until buckling or fracture take place.

Even though the linear elastic behaviour has been thoroughly studied [3], there are several unanswered questions. Elastic instabilities, such as buckling, become very important for 2D low-density lattice materials, widespread for energy absorption and structural protection applications. Recently, lattice films have attracted the attention in the biomedical field for several uses, such as biosensor and artificial skin. The interest in their properties has been enhanced by the advent of novel architectures that show the *auxetic* behaviour–structures with negative Poisson's ratio, when stretched they expand in the perpendicular direction. Designers often make use of the buckling behaviour to tailor mechanical, optical or electrical macroscopic properties of the lattice by modifying the microscopic architecture [26; 27]. By contrast, in biosensors and artificial implants such instability is highly undesired since it causes the biomechanical failure of the implants. This shows the value of predicting the instability of lattice materials when subjected to macroscopic state of stress. Buckling of 2D lattice structures subjected to uniform compression has been previously studied, numerically [28], experimentally [29] and analytically [30]. However, a complex stability problem arises when one constrains a two-dimensional lattice film that is remotely loaded. To the best of our knowledge, instability of stretched two-dimensional films has been studied for homogeneous continuous materials showing a positive effective Poisson's ratio, while explanation of the unusual behaviour observed for structured materials with negative Poisson's ratio is yet missing.

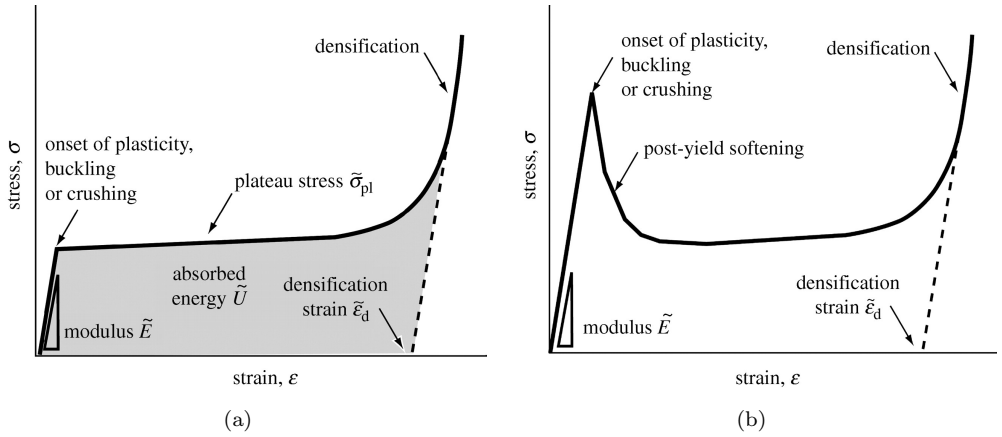

Figure 1.3: A schematic compressive response of (a) bending-dominated foam and a (b) stretch-dominated lattice [12]

1.2 Lattice structures in biomedical applications

The dramatic increase in life expectancy during the 20th century is one of the greatest achievements of the science [31]. However, the population is more exposed to risk of age-associated diseases [32]. The development of new strategies to counteract them is essential to maintain a high quality of life even for the elderly population. Changes in medicine and innovations brought by biomedical engineers have saved lives and improved the quality of life resulting in a greater life expectancy. In the recent years, engineering principles have been progressively applied to biological or medical problems. This has allowed the design of novel bioinstrumentations, biomaterials and implants.

Currently, engineers have started fabricating materials that mimic natural tissues for medical applications [15]. For example, orthopaedic metal implants are coated with tantalum foam since its properties are closer to those of the replaced bone. This limits stress shielding and promotes cell ingrowth. In tissue engineering, porous scaffolds are used as a support in which biological cells can grow to regenerate a wide range of tissues, such as bone, cartilage, tendon, nerves, liver and bladder. The most common methods to produce porous biomaterials are freeze-drying, fibre bonding, foaming, rapid prototyping and electrospinning. Since the microstructure of some biomaterials resembles that of foam-like structures, their mechanical behaviour can be described by the models developed for cellular solids [15]. Scaffolds with honeycomb-like lattice structure are highly attractive for regeneration of cardiac tissue (see examples in figure 1.4). The mechanical properties of such two-dimensional supports can be described by an analysis similar to that presented by Gibson and Ashby in the area of cellular materials [33].

The introduction of lattices to reduce structural weight has also been experienced in the medical area. They allow a reduction of the amount of external material into the human body that often causes infections and post-operation complications, while increasing

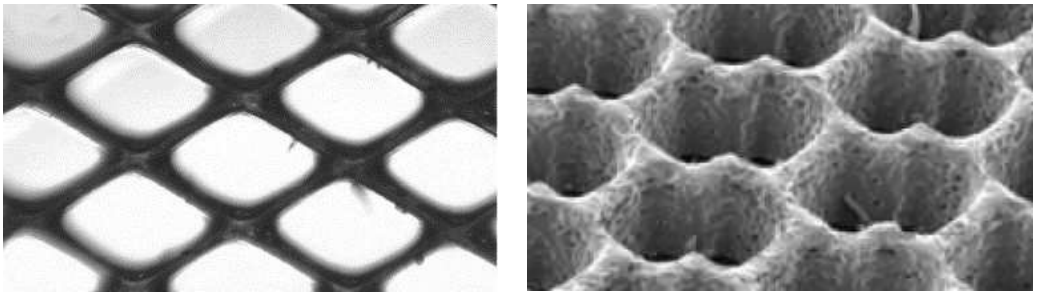

(a) Diamond honeycomb [34] (b) Accordion-like honeycomb [35]

Figure 1.4: Examples of honeycomb-like scaffolds for cardiac tissue regeneration.

the strength of the implant. Moreover, porous structures encourage cell proliferation and tissue regeneration. An important example of a biomedical implant that shows periodicity in its geometry is the cardiovascular stent, as shown in figure 1.1 (f). It has been estimated that the rate of deficiency of oxygen in patients, due to an obstruction (commonly known as stenosis), is more than one million per year only in the United Kingdom [36]. It is estimated that in the United States 610.000 people die of Coronary Artery Disease (CAD) [37]. The blockage is caused by plaque deposition on the inside of the artery walls. White blood cells accumulate on the artery as a response to chronic inflammation of the blood vessel. Surgeons treat most of the patients suffering such obstruction using the angioplasty procedure, a percutaneous intervention technique. Angioplasty is a minimally invasive procedure during which a scaffold, called stent, is implanted to restore the lumen size of the blood vessel and, therefore, the oxygenation of the body. The majority of stents are balloon expandable. A stent is firmly fixed on a folded angioplasty balloon. The balloon is attached at the end of a catheter that is used to deploy the stent, through the groin, to the injured area. Once the surgeon has located the stent, the balloon is gradually inflated until the targeted deployment diameter is reached (figure 1.5). At this point, the balloon is deflated and extracted by using the catheter. The stent has been plastically deformed at this stage to a size diametrically larger than its crimped state and, therefore, it will keep the artery open. Computational modelling is commonly used to assess the stent performance and to optimise them. A large amount of computational resources and time is required to simulate such a complex scenario. Therefore, there is a clear need of a simple model to estimate the stent response during the deployment and the elastic recoil for a quick and efficient preliminary stent design exploration. During ballooning, the implant goes through stages of deformation that highly resembles the stretch of a two dimensional lattice obtained by "cutting" the cylindrical device along a line parallel to the axis and opening it up flat. When the stent is pressurised, it experiences circumferential (or hoop) and radial stresses. This translates to the stretch of the flattened structure; the hoop stress acts as a tensile load. Therefore, the elasto-plastic and recoil analysis of lattice structures subjected to axial tensile load could be directly exploited to provide a

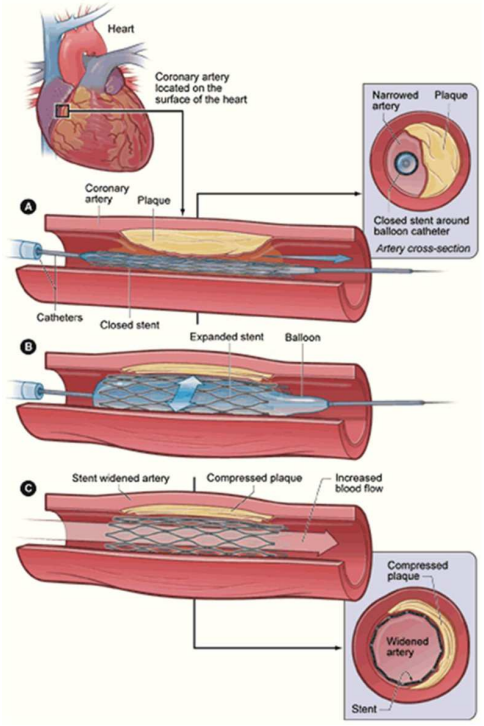

Figure 1.5: A schematic representation of the angioplasty procedure with stent placement [38].

validation of the results obtained using Finite Element Analysis for such implants and to give a high insight into the mechanical behaviour of this class of bio-structures.

Instrumentations, such as heart and blood pressure monitors, represent an important component in medicine to provide a constant and reliable status on people's health. As microelectronics has developed, biomedical instrumentation has become more sophisticated; the size of the instruments has reduced and their sensitivity has increased. This has made possible the manufacture of smaller and more reliable microchips, such as pacemakers and it has open up the field of electrical stimulators to treat neurological conditions, such as Parkinson's diseases [39]. The future in bioinstrumentation lies in implantable devices that can monitor internal tissues or functions and transmit meaningful information regarding variables that monitor human health. In order to make this possible, flexible and biocompatible electrodes that can simultaneously stretch in all directions are required [40]. A geometry that has shown high potential is the one obtained by introducing a set of simple cuts in a multilevel hierarchy, as shown in figure 1.1 (c). The rotation at the hinges gives the high flexibility while keeping the rigid square stress-free. This particular configuration is characterized by negative Poisson's ratio. Thus, when subjected to tensile remote loading, it expands in both directions. Such feature is strongly desirable in future implantable instruments when located on human tissues to monitor a wider area during distension and contraction of muscles. There is also a great interest in the development of film-like structures that exhibit negative Poisson's ratio

for applications such as artificial skin. It is important that such structures are not damaged when externally loaded–stretched, compressed, bent and twisted. The mechanics of such lattice structures resembles that developed for two-dimensional lattice materials. This highlights the importance of theories developed for foams and lattice materials. Therefore, the understanding of their mechanical response when subjected to external loading is closely related to the field of cellular materials. Because of their low bending stiffness, such biomechanical systems are prone to structural instability phenomena–e.g. localised buckling, wrinkling, folding. Although elastic instability is often associated to compressive loading, unusual behaviours occur when thin sheets are stretch. A full understanding of this unusual instability would be valuable for preliminary design of futuristic stretchable sensors and biomedical implants–i.e. artificial skin.

1.3 Aims and objectives

This thesis examines two types of highly non-linear behaviours of planar periodic structures: (i) elasto-plastic deformation of lattice materials and elastic recoil, where the non-linearity arises from the material constitutive law and (ii) instability of films made of lattice materials when subjected to tensile loading. With the exception of Chapter 7, the contribution of this thesis mostly addresses the first question.

The elasto-plastic behaviour of structured materials has been studied in the past both experimentally and computationally via the use of Finite Element Analysis. However, no analytical solution to the problem is available yet. We provide the first analytical model to predict the tensile non-linear response of two-dimensional honeycombs in terms of their bulk material and geometric parameters when loaded beyond the yield point until collapse. Analysis of the elastic recoil and the permanent plastic deformation of the structure when the planar lattice is unloaded is also presented. Initially, the analysis is performed assuming cell walls made of an ideal elastic-perfectly-plastic material. Next, the analysis is made more realistic by assuming a bulk material that shows non-linear hardening, which is described using a novel hyperbolic model. The overall response of the lattice material is derived from that of a single strut. Each cell edge is modelled as a beam under combined loading–axial stretch and bending moment. At first, struts with rectangular cross-section are assumed. Later the model is adapted to cell edges with circular cross-section. The latter geometry has attracted our attention because of the wide use of rapid prototyping for the manufacturing of lattice structures. Typically, the nozzle of 3D printers has a circular shape; therefore, the object of our study are filaments of circular cross-section. Such fundamental beam model has shown great applicability in other areas also, such as metal forming. Some remarks on the possibility to extend these results to other fields will be presented in the later chapters.

As emphasized in the previous section, stents are periodic structures radially expanded to open up obstructed blood vessels. In order to provide an efficient support to the blood vessels, the stent must deform permanently necessitating elasto-plastic analysis during design. Our objective is to exploit the analytical model developed in this project for a planar lattice structure to the study of the mechanical response of stent structures. Such elasto-plastic models are then directly applied to the design of a novel cardiovascular stent as part of the European project ReBioStent [41]. Stent geometries exhibit a remarkable structural periodicity: wavy crowns connected by straight or curved bridges, to provide flexibility during the deployment. By altering the connection between crowns, lattices with completely different apparent properties can be obtained–with positive or negative Poisson's ratio. A novel elasto-plastic analysis is developed for planar structures whose struts are not straight, but show a wavy configuration such that they appear like an opened-up stent configuration. By using this scenario, it is possible to demonstrate the usefulness and validity of the simplified analysis developed for ideal planar lattice structures to model real cylindrical structures of finite size. The elasto-plastic deformation of lattice materials was shown to resemble that undergone by the implant, providing a clear insight into the mechanical behaviour of these bio-structures.

The application of tensile load to constrained two-dimensional thin films leads to problems of structure stability. Under a remote tensile load, an internal localised compressive state of stress gives rise to localized wrinkling. The geometry plays an important role in such unusual and undesired (and possibly counter-intuitive) behaviour. By studying the influence of the internal architecture on the film instability, we aim to establish a membrane that overcomes such unwanted behaviour. The study of localised buckling under tensile loading for thin films made of bulk material with positive Poisson's ratio has shown that instabilities spread within the greater part of the film [42]. However, the changes of these phenomena observed when the film possesses auxetic behaviour–thus the Poisson's ratio is negative, have not been taken up. An experimental study and an analytical model to predict the wrinkling of such films are for the first time presented here. The results are also validated using finite element methods. Understanding this peculiar behaviour of thin sheets is extremely important for futuristic applications, such as stretchable bioinstrumentations and artificial skin, where auxetic structures have shown high potential. The study presented here is only a preliminary work and the developed theory only provides a simple yet interesting explanation of this unusual behaviour.

To summarize, the main aims and objectives of this work are:

- The study of the elasto-plastic deformation of lattice materials and elastic recoil with applications to biomedical implant:
  - to provide a benchmark analytical solution for the elasto-plastic response and recoil of hexagonal honeycomb sheet loaded past yielding;

  - to provide a realistic analysis for the elasto-plastic response by including the effects of material hardening;
  - to generalise the benchmark solution to lattice materials with cell walls possessing a circular cross-section, giving its importance to 3D printed scaffolds;
  - to develop structure-property relationship for a periodical cylindrical structure whose main geometric features resemble that of a cardiovascular stent;
  - to develop novel stent designs and prototypes for use with new biodegradable materials.

- The study of the instability behaviour of lattice films for futuristic biomedical applications
  - to experimentally compare and contrast the instability behaviour of thin lattice films with positive and negative effective Poisson's ratio;
  - to develop an analysis to explain the localised mechanical behaviour of stretched auxetic thin films at the constrained edges.

1.4 Outlines of the thesis

An outline of the dissertation is presented here. The thesis is organised in eight chapters. The existing scientific literature on elasto-plastic deformation of lattice materials is reviewed in Chapter 2. The final part of that Chapter is focused on biomedical applications where elasto-plastic analysis plays an important role. In Chapter 3, the benchmark elasto-plastic solution for honeycomb structures is developed assuming an elastic-perfectly-plastic material and lattice struts with rectangular cross-section. The material hardening effects of the constituent material and the effects of change in the cross-section shape of the struts onto the elasto-plastic response of regular lattices are taken up in Chapter 4. An analytical model to calculate the response of cylindrical periodic structures that resemble cardiovascular stents available on the market is presented in Chapter 5. Such model is then used in Chapter 6 to develop two novel stent prototypes for biodegradable devices. The analysis of elastic instability of thin film is presented in Chapter 7, together with simple experiments to validate the study. Finally, Chapter 8 summarises the main findings of this work together with future possible extensions.

Chapter 2

Micro-architectured materials and biomedical applications

A review of the current literature on lattice and cellular materials and stent implants is presented in this chapter. An in-depth revision on the elastic response of lattice structures and on the current knowledge on their mechanical behaviour when they undergo plastic deformation is presented here. The overall lattice response is inferred from that of a single strut, which is modelled as a beam subjected to complex loading, in conjunction with the lattice kinematic. The recent progress in the elasto-plastic analysis of beams under simultaneously bending and stretch are reviewed next. Following, the existing knowledge on the response of materials showing a random configuration in space under compressive and tensile loading is presented. The remaining part of the chapter focuses on the state of the art in the area of the mechanics of stents, a biomedical implants used during the angioplasty procedure. It also describes in detail investigations on the mechanical characteristics desired from the scaffold and the existing models used to study the mechanical response of stents during implantation.

Such review shows the lack of a complete elasto-plastic analysis for lattice materials. No studies on the elastic recoil are present in the area of lattice structures, because it appeared unnecessary for any real scenarios until now. The literature review on stents reveals the significance of the quantitative assessment of the mechanical response of these scaffolds during the deployment phase. Any analytical information, even though approximate, is particularly useful and valuable as quick and efficient tools at early stages of design search. The degree of springback of a lattice post-plasticity can be directly used to estimate the radial recoil of cardiovascular stents, which is a key performance parameter for such biomedical implant. This further highlights the importance of a complete plastic analysis, so far missing in the literature.

2.1 Periodic lattice structures

The design of mechanical parts is often driven by the need to reduce weight without compromising the mechanical performance. In many biomedical applications, such materials and structures often need to allow cell proliferation and growth, in addition to providing the mechanical function of the implant during the deployment and service. Interestingly, the mechanical properties possessed by the lattice structures are frequently superior to those of the corresponding constituent solid [3] and this is achieved by placing material where it is needed. Following the seminal work of Gibson *et al.* [33], a large body of literature on the mechanics and engineering of cellular materials has appeared. This includes linear and geometrically non-linear response calculations using exact and approximate analyses in addition to experimental work in the area of mechanical impact [43; 44]. A detailed elasto-plastic analysis, a necessary step for the calculation of recoil upon unloading, seems to be missing from the literature. A regular hexagonal honeycomb geometry has been considered here in order to facilitate calculations and also to present results for a benchmark lattice geometry.

When lattice structures are loaded, the response of the material is initially linear which is followed by plastic deformation when the load exceeds a certain limit. In this work, we ignore the geometric non-linearity due to large deflection of the cell walls. This choice is deliberate as the motivation of the present work is to study the role of structural and material parameters in the plastic response of honeycombs. We do acknowledge, however, that there may be significant geometric non-linearity present in certain circumstances. However, presently this is excluded from consideration. Besides the motivation to isolate the response due to material non-linearity, our confidence in the approach is supported by numerical examples in the subsequent chapters. Once the load is removed past yielding, the elastic deformation is recovered whilst the deformation associated with the plastic behaviour is permanent. This effect is known as elastic recoil or springback. The mechanics of springback has been extensively studied in the context of metal forming processes. However, for lattice structures, no analytical results, neither computational work nor experimental studies are available yet.

The lattice geometry when kinematically mobile lends itself to bending dominance and formation of plastic hinges upon loading which manifests into desirable properties, such as energy absorption capability [45; 46]. The honeycomb is perhaps the most frequently studied configuration over the years in the cellular materials field. A reason for this is the potential applicability of the results obtained from regular hexagonal honeycombs to other cellular structures that exhibit bending dominance. Due to its regularity, the mechanical properties can be easily described in a closed form. Methods have been developed previously to analyse honeycombs when they deform elastically. In the early 1980s, Abd El-Sayed *et al.* [47] studied hexagonal honeycombs analytically by using beam theory to model the cell walls. They calculated the in-plane Young's moduli,

Poisson's ratio and the plastic collapse load. The geometry they considered has vertical cell walls of double the thickness than those that are inclined. Gibson and Ashby [3] considered a hexagonal honeycomb with identical cell walls which leads to isotropic inplane bulk properties. They used a unit cell approach and derived apparent linear elastic properties there from. This was extended to geometrically non-linear behaviour at large deformations by Hu *et al.* [48]. In-plane mechanical properties of other geometries rather than hexagonal cell, e.g. square cell, triangles, mix of squares and triangles, Kagome cell, rectangular cell and diamond cell, have been investigated by Wang and McDowell [49]. The apparent properties of the lattices have been inferred from those of a single cell wall, as previously done for the honeycomb. Each strut has been modelled as a beam under combined bending and stretch. Expression for the mechanical properties obtained include Young's modulus, elastic shear modulus, effective Poisson's ratio and initial yield strength under uniaxial loading. In these works, the overall properties are obtained via discrete modelling of cell walls as beams or trusses. This approach gives an accurate stress and strain distribution within a structure; however, it is computationally expensive when a structure made of lattice material has to be modelled since each cell wall needs to be analysed. Continuum finite element approaches have been developed to obviate this problem and the constitutive matrix, the matrix of mass densities and the matrix of thermal coefficients have been generated for repetitive lattice structures [50; 51].

The plastic limit behaviour of cellular material subjected to in-plane compressive load has been extensively studied in the past using a combination of experimental and analytical approaches. When subjected to compression, the failure of the lattice can be due to elastic buckling or plastic collapse of the struts. Gibson and Ashby [3] used the plastic hinge theory to obtain the collapse limit of honeycombs. This approach is based on the mechanics of cell collapse, when the moment in a cell wall equals the fully-plastic moment of the cross-section. Menges and Knipschild [52] estimated the 'elastic' failure stress by assuming that the collapse of the cells corresponds to the buckling of the struts. However, such approach greatly overestimates the failure stress for crushed honeycombs [53]. Klintworth and Stronge [53] combined elastic buckling modes and plastic collapse modes, that are geometrically similar, to obtain the elasto-plastic crushing modes of honeycomb. Taking into account the interaction between these two phenomena allowed a more accurate estimation of the collapse stress. Before the fully plastic moment within a section of a strut is reached, the cell walls start to deform plastically, if buckling does not occur. An analysis of this process is missing in the Klintworth and Stronge model [53]. Zhu and Mills [54] studied the effects of the material parameters on the elastic and plastic collapse of honeycombs with different relative densities. Three plastic collapse modes are found by Karagiozova and Yu [55] in the deformation of regular hexagonal honeycombs. By using the plastic hinge theory, they studied the preferable deformation mode under prescribed loading conditions based on the principle of the lowest internal energy. Chuang and Huang [56] studied the yield surface for an hexagonal honeycombs

with plateau borders using the plastic hinge theory. They presented the combination of loading at which the material within the struts reaches its yield point. This was further extended for five other types of cell configurations by Wang and McDowell [57]. Crushing of honeycombs has been experimentally studied by Papka *et al.* [58] in order to examine the three regimes that honeycombs show during compression–linear, plateau and densification regions (as previously presented in figure 1.3). Such experimental results were compared with numerical simulations, which gave a higher stiffness and plateau stress. This can be due to geometric imperfections arising during the manufacturing process of honeycombs. Some years later, the same authors studied in-depth the influence of imperfections on the mechanical properties of honeycombs [23]. Using numerical simulation, Chen *et al.* [59] brought out the effect of defects on the hydrostatic yield strength of foams. A numerical study of plastic deformation of a honeycomb and Voronoi structures has been performed by Mangipudi *et al.* [60], who used the finite element approach to account for the gradual plasticisation of cell walls. They focused the analysis on the combination of material hardening and geometric hardening–due to the reorientation of inclined struts–on the plastic deformation during in-plane tensile loading.

The review above reveals that analytical studies to calculate the elasto-plastic response and recoil of honeycomb structures are missing. The same is true of elastic recoil upon unloading. Motivated by this, we present analytically obtained plastic response and recoil of a honeycomb lattice in the next chapter. The present work fills the gap between the known results for elastic response and the collapse limit via the intermediate stages of non-linear response due to plasticity. In this work, we will firstly ignore the kinematic non-linearity due to large deflection of the cell walls and the non-linearity introduced by the material hardening. These simplifications and idealisations will be lifted later, in order to obtain a general model which accurately describes the real behaviour of an hexagonal infinite sheet.

2.2 Elasto-plastic analysis of a cell wall

The analytical study of lattice structures, due to their periodicity, can be frequently reduced to the analysis of single structural elements that are repeated in the space to build the periodic configuration. In the case of two-dimensional honeycombs, the analysis focuses on the inclined cell walls which can be modelled as cantilever beams under combined bending and stretch. Bending analysis of a beam has been extensively studied since it is the basis of many engineering structures. Elastic bending of a beam has been fully developed and analytical solutions are available for both small and large deformations. Approaches to predict elasto-plastic response and recoil of elastic rods make use of various approximations in order to simplify the analysis [61–64]. The situation is particularly complicated when the stress-strain relationship in the plastic regime is complex.

Therefore, analytical results for elasto-plastic beam response are limited. Due to analytical difficulties in solving the equation governing the elasto-plastic problem, numerical and experimental techniques have been extensively used in the past [65; 66]. However, some closed form solutions are also available. Exact solutions are well-known for beams with rectangular cross-section subjected to constant bending moment. Only few closed-form analyses are known for non-constant bending moment distributions along the length of the beam, such as linear [67] or quadratic [64; 68; 69] distribution. In all these studies, elastic-perfectly-plastic material has been assumed. This idealisation is frequently used in analytical work as the starting point, since it simplifies the mathematics and includes most essential features of the plasticity problem. In order to obtain a more realistic description of the beam behaviour, the non-linear hardening effect must be taken into account during the plastic analysis. This work aims to provide such a generalisation and yet successfully affords closed form solution. Chapter 4 is concerned with developments along these lines.

Plastic deformation of rods is encountered in the manufacture of many components used in automotive, aerospace and transportation engineering sectors of the industry. Perhaps the most common example is forming of metal sheets and curved beams. Such components and processes are used in several mechanical engineering applications, such as load-bearing devices, steel wires for tyre manufacture or in civil engineering structures for aesthetic purposes. In many real scenarios, the beam is subjected to combined bending and tensile axial forces. The application of a longitudinal force affects the position of the neutral axis, which does not go through the geometric centroid of the cross-section any more. Therefore, the stress distribution in each cross-section is not symmetric, even if the cross-section is geometrically symmetric with respect to such axis. The most common cross-section shapes of rods encountered in engineering are rectangular and circular. The problem of plastic deformation of rods of rectangular cross-section under combined axial-bending loading was solved analytically for the first time by Yu and Johnson [67] sometime ago. Their solution was developed assuming a symmetric cross-section. Therefore, the beam does not possess bend-twist coupling and the neutral axis is perpendicular to the plane of geometrical symmetry. Later, they analysed the elasto-plastic response and springback for L-section beams under bending while accounting for the shift and the rotation of the neutral axis [70]. Stretch-bending analysis and springback of U-section beams was taken up by El-Domiaty and Elsharkawy a few years later [71]. Surprisingly, to the best of our knowledge, the case of elasto-plastic response and recoil analysis for rods of circular cross-section under combined loading seems missing from the literature. A source of mathematical difficulty for beams under combined loading is the lack of validity of the superposition principle because of the non-linearity introduced to the problem by plasticity.

In addition to metal forming, a problem that possesses very similar features, in terms of the mechanics and the geometry, also arises while dealing with the micro-mechanics of

many additively manufactured lattice materials such as those for biomedical implants. This is particularly true when fused deposition modelling (FDM) is the manufacturing process. This is because the material is dispensed in a semi-molten state as stacked cylindrical filaments from a circular nozzle. When such biomedical scaffolds undergo complex loading, individual filaments are often under combined stretching and bending [3]. The present work is inspired by a host of such practical problems, especially in the biomedical engineering domain. Here, the application is mainly focused on the elasto-plastic analysis of lattice structures. However, in the relevant chapter, a small section will be dedicated to stretch-bending of a single rod to show the applicability of these models to other engineering fields, such as that of metal forming.

The springback problem in plasticity is particularly critical in several industrial sectors. For example, the quantitative assessment of the recovery of the elastic deformation is extremely critical in biomedical applications, such as in stents technology. The implant is deformed after the yield point during the deployment such that the blocked blood vessel is permanently open. This relates closely to an important performance parameter the so-called radial recoil of the device. Such an analysis is also critical while assessing the mechanical response of stent structures during crimping–a phase of packaging the implant before deployment into blood vessels. Further, analytical prediction of the final manufactured shape after a process such as die-forming is challenging due to the non-linearities introduced by plasticity and the recovery of the elastic deformation upon unloading. Die geometry frequently dictates the presence of combined axial-bending loading. To the best of our knowledge, the commonly encountered problem of simultaneously bent-stretched circular rods, wires and filaments has not been solved in a closed-form yet, either in the metal forming area or in the rapid manufacture of lattice implants. During the manufacturing process, the material undergoes elastic deformation first,which is followed by plasticity. Due to recoverable elastic deformation, the final shape of the structure, following the forming process, is not the one imposed by the forming tool, but the recoverable elastic strain must be deducted. Several possible measures are taken in practice to account for the springback. For example, extra features in radii or variation in blank holder force are the corrective measures to ensure the shape of the formed part to be the same as intended after springback has taken place. In stretch-bending processes, rods are clamped and stretched from their ends and bent over a die [71]. The key problem encountered is the control of the effective residual curvature after the process. The application of a tensile load reduces the springback; however, the inevitable elastic recovery will always be observed which necessitates studies to quantitatively predict the same. Trial and error methods have often been used to establish the appropriate setting parameters during real manufacturing scenarios. Only recently researchers have started looking at the influence of cross-section shape on the final deformed shape after unloading using analytical approaches [72].

The model provided by Yu and Johnson [67; 70] for a rectangular cross-section and

that proposed by El-Domiaty and Elsharkawy [71] for a U-beam are the only known *analytical solutions* that consider the elastic springback once the structure is unloaded for beams under combined bending and stretch. However, the constitutive material law used by them is one of elastic-perfectly-plastic material for the rectangular beam and a simplified bilinear hardening model for the U-beam. Therefore, the solutions provided are idealisations and they give only an approximate solution for the real situation. A theoretical study on the non-linear bending of wires with rectangular and circular cross-section assuming three different types of material behaviour was presented by Baragetti [73]. They developed an analytical approach to predict the final shape of a wire without using finite element analysis. However, no stretch is included in his study [73]. The accurate description of the material plastic behaviour is important in order to obtain a reliable quantitative estimate of the mechanical behaviour. All the materials initially show an elastic behaviour, which can be more or less extended, modelled as a straight line in the stress-strain plane. When the yield point is reached, the material starts deforming along preferential planes through the movement of dislocations for polycrystalline materials. This results in a non-linear relationship between stress and strain. For polymeric materials, the origin of non-linearity lies in the physics and the chemistry of polymer chains. Several mathematical representations are available to model material hardening. Power law is a commonly used material constitutive law when the plastic strain is large [74; 75]. However, this representation introduces difficulties in the analysis later developed here. Therefore, a new mathematical model which captures both linear and non-linear behaviour is proposed here.

The purpose of Chapter 4 within this work is to extend the study of elasto-plastic bending of filaments and rods by providing a closed-form solution that describes the bent deformed shape of the filament, including the effects of the material hardening together with the stress stiffening effect due to the presence of an axial force. Chapter 4 is inspired by the need for a general analytical formulation for the calculation of the elasto-plastic deformation of roads and filaments under combined loading. Considering the thickness to be much smaller than the length of cell walls allows us to ignore the shear through the thickness. This condition is satisfied in several realistic situations without limiting the general nature of the solution. This new model will then be included into the study of periodic lattice structures in order to incorporate into the analysis the non-linear effects due to the material hardening and to study the influence of the cross-section shape on the mechanical response.

2.3 Elasto-plastic analysis of foams

Solid foams are an important class of materials in applications where low weight, but high strength are required. Their capability to absorb energy makes them appropriate

for impact absorption devices, such as personal protection systems for defence applications, helmets etc. Compared to the lattice structures described earlier, the solid foams possess a disordered micro structure, as the example shown in figure 2.1. During the design process of new engineering products, the structural analysis of components made of foamed material is often performed by replacing the detailed random micro structure by a homogenized material [76]. The material is modelled as a continuum to which macroscopic foam properties are attributed. A model to predict the macroscopic behaviour of solid foams is required to design materials with the desirable properties, which are determined by the final application. To this end, a new field of study has been developed for the prediction of the macroscopic effective properties. This can be approached either experimentally or analytically. The importance of a theoretical approach lies in the possibility of describing general features that can extensively reduce the experimental expenses due to testing. By identifying generic characteristics of the physics, it is possible to obtain a general result that can be extended to any structural foam by using the scaling analysis.

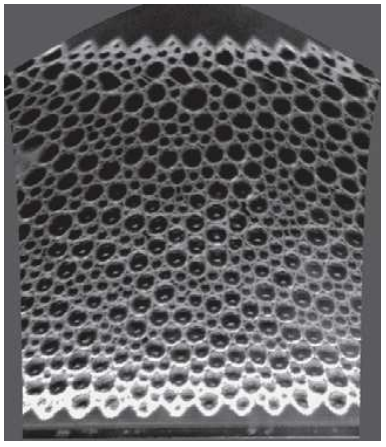

Figure 2.1: Bidisperse disordered monolayers foam obtained by bubbling nitrogen through the fluid [77].

The elastic properties of foams have been studied by Gibson and Ashby [3]. Analytical relationship between elastic properties and relative density of the foam were determined by studying the deformation mode–bending dominated or stretch dominated. The study of the effects of the micro structure variability on the elastic properties of two-dimensional foams with low relative density (≤ 0.25), presented by Silva *et al.* [78], has shown that the arrangement of cell walls does not significantly influence them–the coefficients of variation is about 4-9%. These results are in contrast with those obtained by Zhu *et al.* [79]. They showed that the Young's modulus and shear modulus of random bending dominated structure can be 25% greater than those of honeycombs with the same relative density. This inconsistency has been attributed to the different boundary conditions considered during the FEA analysis and to the larger level of irregularity considered by Zhu *et al.* [79] during the analysis. The assessment of the influence of relative density and cell wall shape on elastic properties of random two-dimensional foams was

recently improved by Harders *et al.* [80], who showed that the Young's modulus reaches its maximum when the cell wall shape is slightly concave.

It has been experimentally demonstrated that the foam yielding depends on both hydrostatic stress (stress responsible for the change in volume) and deviatoric stress (stress responsible for the change of the shape) [81]. The influence of six types of imperfections (waviness, non-uniform cell wall thickness, cell-size variations, fractured cell walls, cell-wall misalignments and missing cells) on the plastic deformation of two-dimensional foams has been studied using analytical and finite element approaches [59]. It has been shown that foams possessing imperfections yield at a lower hydrostatic stress compared to foams with regular and perfect microstructure. Later, Silva and Gibson [82] studied the effects of non-periodic micro structures and defects on the compressive failure behaviour of two-dimensional foams. They showed that random structures are roughly 30% weaker than regular hexagonal ones and the removal of cell walls at random location results in worsening of mechanical properties.

The plastic response of a two dimensional foam is influenced by the hardening law of the bulk material which constitutes the microstructure. Papka and Kyriakides [58] showed for the first time that the yield stress and the post-yield behaviour of the constituent material significantly affect the initiation and propagation of loads in honeycombs under compression. It has also been shown that the elastic properties and the onset of plasticity of the material within a periodic lattice can be evaluated by performing a simpler analysis on a representative section of the periodic structure. This demonstrates that the foam properties can be inferred from the local response of the material, after verifying that the micro and macro structural length scales differ by several orders of magnitude. Marchi and Mortensen [83] studied the open-cell aluminium foam under compression. They show that, at low strains, the hardening exponent of the foam corresponds to that of the bulk material. Later, this was reinforced experimentally by Amsterdam *et al.* [84]. They successfully predicted the collapse stress of open-cell aluminium foams using the yield stress and hardening exponent of the constituent material, as a function of the relative density. However, all these studies are not valid at large deformations due to the geometric non-linearities. Recently, the plastic deformation of random two-dimensional foams has been studied using finite element analysis including the geometric non-linearity by Mangipudi *et al.* [60]. The model takes into consideration the gradual plasticisation of the cross-section due to material non-linearity and the decrease in cross-sectional area. They show that foam hardening is a linear function of the bulk material hardening and geometric hardening [60].

The geometric randomness introduces into the system an uncertainty that results in disperse material properties. This limits the possibility to perform an exact analytical prediction. Mangipudi *et al.* [60] observed that the mechanical response of a random two-dimensional foam and that of a honeycomb show some similarities. This strongly suggest the possibility of inferring the stress-strain curve of a random bending dominated

foam using the analysis developed for regular hexagonal structures by using a statistical approach.

2.4 Applications in Biomedical Engineering

Although advanced technologies have been used in recent years to improve the angioplasty procedure, some clinical issues still affect the outcome of the stenting. Two main post-operative complications are frequently encountered–the in-stent restenosis [85] and the late stent thrombosis [86]. The former is a recurrence of stenosis and develops primarily within the first 6 months leading to the reclosure of the vessel [87]. The latter refers to the formation of blood clots that may, partially or totally, occlude the vessel. These issues are mainly related to the damage of the wall of the blood vessel during the deployment of the stent [88], the inflammation of the wall vessels [89], the presence of residual stresses inside the wall of the blood vessel [90] or the shear stresses due to the disturbance of the haemodynamics by the stent [91]. The in-stent restenosis ratio for Bare Metal Stents (BMS) is in the range 20-50%; this rate is also linked to the design of the stent [92; 93]. Restenosis rates have been reduced to 10% with the introduction of Drug Eluting Stents (DES), stents coated with a pharmacological drug gradually realised in the wall, that aims to reduce the inflammation of the vessel [94]. Even though a good improvement is associated with this new improvement in the implant, it is important to reduce it further since many patients are treated with DES. Late thrombosis is also a critical problem with the use of DES [95].

There has been a drive to replace BMS and DES by stents that are resorbable as this is expected to eliminate many of the post-operation complications associated with stenting. A motivation for this comes from the fact that the vascular support provided by stents is required only in the first few months after angioplasty as vascular remodelling takes place through normal physiological processes. The use of bioresorbable scaffolds represents the fourth generation of interventional treatments for cardiovascular diseases. The scaffold combines the three key requirements: (i) it provides support as a metal stent, (ii) it releases drug in order to prevent the risk or instant restenosis as DES and (iii) it disappears after six months of implantation, when the blood vessel has restored his original size [96]. Most of the current biodegradable devices are made of Polylactic Acid (PLA), even though other materials such as magnesium have been tried for the manufacture of bioresorbable stents. The polymer composition can vary significantly within this group of materials and hence their physico-chemical properties which determines the radial strength and loss of mass from the device. At present, there are only two biodegradable devices on the market: Absorb Bioresorbable Scaffold from Abbott [97] and DESolve scaffold from Elixir [98]. The ReBioStent project [41] aims to introduce a novel bioresorbable stent on the current market using a novel and multifunctional material.

In approximately the last two decades, computational models have become a fundamental tool to examine the mechanical performance of the stents, their mechanical properties and to optimise them. Many possible real situations can be analysed with the advantage of measured physical properties difficult to be tested *in vitro*. By contrast, numerical methods are approximations of real situations, therefore a clear validation must be undertaken. The following sections provide a brief review on the biomechanical modelling of stents available today and the possible future steps.

2.4.1 Numerical modelling of the mechanics of stents

An ideal stent should be easy to deliver and deploy and should provide adequate support while the interventional complications such as restenosis and thrombosis should be minimised. These qualitative requirements can be expressed in concrete quantifiable engineering terms. An ideal stent should possess the following properties:

- Good flexibility: the stent must be flexible when crimped on the balloon, since it has to be delivered to a damaged location through the vascular path, characterised by narrow and twisted sections.
- Uniformity of expansion: the technique used to implant the stent is an important parameter that influences injury of the vessel and, therefore, the occurrence of sides effects [99]. When the balloon is inflated, it assumes a dogbone shape which depends on both the balloon and stent design. The non-uniform expansion, particularly at the ends, generally results in a high degree of damage of the blood vessel.
- High radial strength: the stent is a scaffold that has to provide the support to the vessel in order to restore the lumen size. If enough radial strength is not provided, the post-stenting recoil (reclosure of the vessel after the stenting procedure) occurs, resulting in a failure of the implant.
- Low elastic recoil: the stent is plastically deformed during expansion to provide scaffolding. When a plastically deformed structure is unloaded, the elastic deformation is recovered. This effect is called elastic recoil or springback. The rate of restenosis is closely related to the elastic recoil [96]: the larger the recoil is, the more stretch must be applied to the vessel in order to obtain the final stent diameter equal to the vessel diameter. Moreover, during the elastic recoil, the shortening of the stent is observed. This effect influences the accuracy of the implant location and it may cause blood vessel injuries [96].
- Minimal hemodynamics alteration: a dependence between hemodynamics alteration (changes in the blood flow) and restenosis (the recurrence of the narrowing of the blood vessel) has been seen [91].

Measuring all these structural properties directly in different conditions and for different designs requires a lot of effort and it is not always possible to test *in vivo* since biomedical systems show high variability and complexity [100]. As a consequence, the numerical modelling using finite element analysis (FEA) is indispensable to investigate their mechanical behaviour. However, due to the high number of factors that influence the problem, simplifications are desirable at early stages of design. Simplifications necessarily introduce inaccuracies which means that there is a trade-off between realism and simplicity of the models.

The modelling of the stenting procedure consists of four main steps [100]: the construction of the vessel and stent model, definition of the constitutive laws for each component of the system (blood, balloon, stent, tissue), definition of appropriate boundary conditions to describe the real load and environment in which the stent is implanted and, finally, numerical simulation of the interaction between stent-vessel walls-fluid. The effect of blood vessels on the mechanical response of stents is frequently compromised in order to compare the mechanical performance of the stent alone.

2.4.1.1 Reconstruction of the vessel and stent model

In the past ten years, significant resources have been invested in the reconstruction of the coronary arteries using image-based models [101; 102]. Huge effort is required to achieve this since blood vessels are small, tortuous, they follow complex path and they are always in small amplitude motion. The image-based process is summarised in figure 2.2. Using medical images obtained from 3D imaging techniques (generally computed tomography angiography CTA or magnetic resonance imaging MRI) data are extracted to reconstruct the geometry of the vessel skeleton. This is done by aligning several 2D cross-sections of the vessel. For bifurcation, this process is more complicated as it requires the reconstruction of each vessel and a following merge. Once the 3D model is available, it can be meshed, normally using structured (for straight tube) or unstructured meshes. Due to their complexity, for bifurcations a tetrahedral mesh is required [103].

2.4.1.2 Structural models

A review of the existing FE studies of balloon-expandable stents reveals that the analysis can be classified in three main groups: a balloon-free analysis, cylindrical balloon and folded balloon. This classification also shows the chronological order followed during the development of numerical models. Firstly, the balloon is ignored in the model and only a uniform pressure is applied at the inner surface of the stent [104]. Dumoulin *et al.* [105] evaluated the mechanical properties of the balloon-expandable *P308 Palmaz* stent and stated that a balloon-free model is a good approximation of the central part of the stent. Recently, McGarry *et al.* [106] developed a numerical model for a stainless steel stent

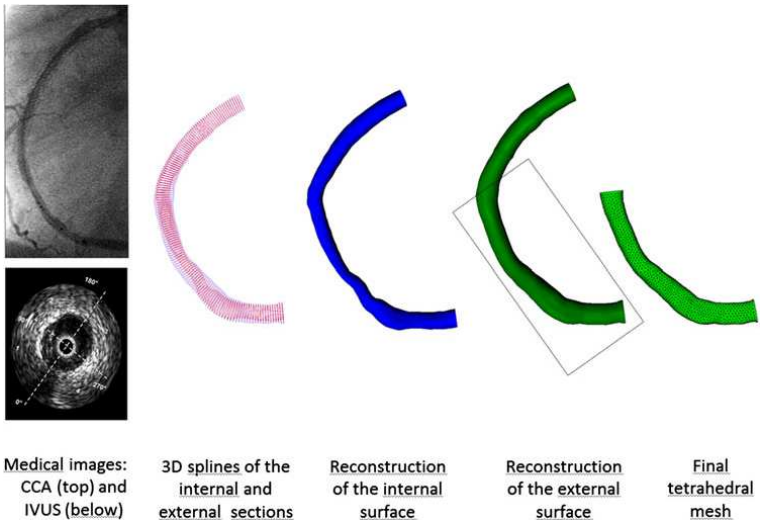

Figure 2.2: Main steps required to reconstruct the blood vessel [100].

using crystal plasticity theory since a continuum approach, due to the small dimensions of stent struts ($100\mu m$), is questionable. An elementary fatigue study is presented by them in the form of Goodman diagrams. Lally *et al.* [107] introduced the hyperelastic model to characterize the plaque. However, the expansion process is neglected which results in the impossibility to study the shear forces during the expansion. Magliavacca *et al.* [108] firstly studied the unloading process after the deployment. A difference between the experimental and computational results was observed and it was attributed to the absence of the balloon. In 1999, for the first time, a model that assumed a linear elastic balloon with a cylindrical shape was developed by Rogers *et al.* [109]. It was found that the presence of the balloon is indispensable to accurately describe the stent-artery interaction. In 2008, the model for a tri-folded balloon was presented by De Beule et *al.* [110]. They showed that this more realistic model is necessary in order to obtain a better agreement between experimental and computational results. The three different modelling strategies are illustrated in figure 2.3.

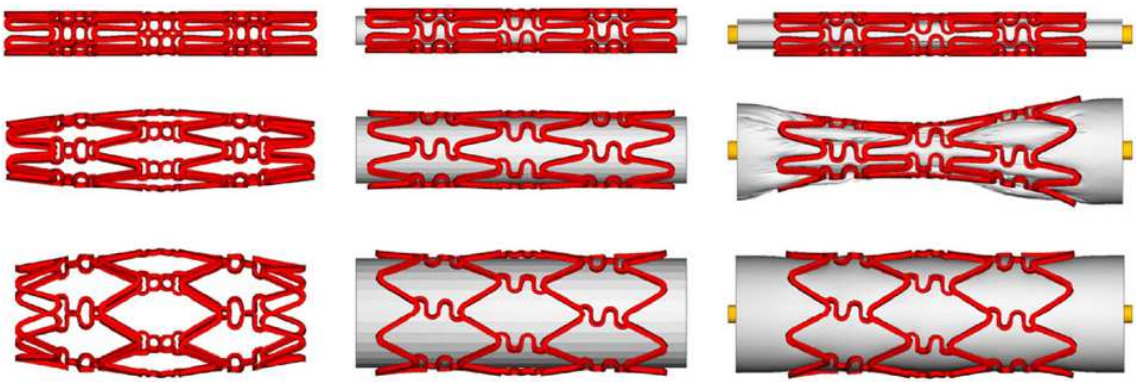

Figure 2.3: Application of internal uniform pressure (left) model of a rigid cylindrical balloon (middle) and model of a folded balloon (right) [100].

2.4.2 Future steps

As can be noticed from the previous section, further improvements of stent models can be performed by including more realistic materials or designs. Associated with the image processing currently available, more realistic and accurate blood vessel models can be obtained and they can be used within the numerical solution.

Predictive confidence and reliability of numerical results is possible only if a mathematical verification or validation against experimental data are available [100]. According to ASME Committee for Verification and Validation in Computational Solid Mechanics [111], verification is defined as "the process of determining that a computational model accurately represents the underlying mathematical model", while validation as "the process of determining the degree to which a model is an accurate representation of the real world". For the stenting procedure, the validation is time and money consuming since real experiments must be performed. Some experimental data are available in the literature [110; 112; 113]. However, the absence of standard results in the presence of high variability in the outcomes [100].

Nowadays only few analytical models can be found in the literature for the prediction of stent performance and they are limited to the elastic regime and the failure of the structure. Jie and Nan [114] presented an analytical approach to calculate the radial stiffness in the elastic regime of a tubular stent whose crown assumes a sinusoidal shape. Further, they [115] calculated the plastic limit for the same tubular structure, thus the pressure at which the ideal stent fails, assuming an elastic-perfectly plastic material. The collapse pressure is predicted by modelling the struts as strength beam under combined bending and stretch. They used the plastic model proposed by Yu and Johnson [67] for a cantilever beam under inclined tip loading to calculate the loading at which one section of the crown reaches the full-plastic bending moment [115]. By simplifying the crown using straight beam, the effects due to the curvature of the sinusoid are neglected. Depending on how the deployment is performed, available on the market there are also self-expandable stents. In this case, the stent is constrained at a smaller diameter using another tube which will be removed once in place. The implants are made of a shape memory alloy; therefore, it does not necessitate a plastic analysis. More analytical studies are available to predict the expansion properties of self-expanding metallic stents since the coiled helical springs of the implants undergo only elastic deformation. Therefore, complications due to plasticity are not involved in their analysis of the deployment procedure [116].

By contrast, analytical models to verify the full expansion procedure up to the non-linear behaviour due to the plastic deformation of the implant are missing in the literature. As emphasised in the previous paragraph, the stent is a periodic structure, therefore our objective is to exploit the models developed in the present work to this practical application in order to provide higher reliability to the FEA results. As a first approach,

we will focus on the model of a stent neglecting the presence of the balloon. Such approaches are invaluable at early stages of stent design. They provide closed-form analytical dependence of the response over the geometric and material parameters.

2.5 Conclusions

A review of the existing scientific literature shows that the available work on lattice materials is limited to the linear elastic response and the calculation of the collapse point. The transition between elastic regime and the collapse point of the structure has not been considered analytically yet. Likewise, the analysis of springback of a lattices post-plasticity is currently missing in the literature since it requires the knowledge of the full elasto-plastic response of the structure. The response of the lattice structure is inferred from those of a single strut which is modelled as a beam. The summary above shows that the solutions available for the analysis of beams under plastic deformation are limited. Therefore, new beam models accounting for material hardening and change in cross-section shape are required first.

Such an elasto-plastic model has shown high potential in the study of stent implants. The degree of springback of a lattice post-plasticity is critical for applications such as cardiovascular stents where permanent plastic deformation needs to be quantitatively assessed. The need of analytical approaches to estimate the mechanical response of such biomedical applications has been underlined. The benefits and effectiveness of mathematical analysis within a practical context will be further highlighted when the developed methodology will be directly applied to the design of a real stent which is currently being developed[1].

[1]Reinforced Bioresorbable Biomaterials for Therapeutic Drug Eluting Stents project–ReBioStent. The main aim of the ReBioStent project is the production of biodegradable and biocompatible resorbable stents [41].

Chapter 3

Elasto-plastic response and recoil of honeycomb lattices

Several practical engineering applications require elasto-plastic response and recoil calculations. An example of this is the stent structure which is expanded during the surgery post-plastic state in order to open blocked blood vessels permanently. Further, a quantitative prediction of recoil is also required in this context because one needs to know the diameter of the stent post-ballooning configuration. While the geometry under consideration is not very realistic for such biomedical implants, an abstraction such as the one considered here provides a benchmark for more complex architectures. Translational symmetry inherent in the geometry facilitates the analysis of such periodic structure in a closed form. In the present work, we make use of this periodicity in order to be able to calculate the response during loading and unloading of such lattice material past the yield. The material model used is one of elastic-perfectly-plastic which is an idealisation frequently used in analytical work. A review of the literature presented in the previous chapter reveals that analytical solutions for the elasto-plastic response and recoil of honeycomb structures are missing. The work presented in the following chapter is inspired by this need. The apparent behaviour of two-dimensional lattice structures is presented and a parametric analysis is performed.

When a cylinder is subjected to internal pressure, a hoop stress is produced in the wall. A stent is a cylindrically folded lattice structure which is pressurised internally during the deployment. If we neglect the curvature effects as a first approximation, the stress analysis problem becomes equivalent to one of a flat periodic structure under remote in-plane loading. We are, therefore, assuming the hoop stress as the dominant stress in the structure. We acknowledge the possible inaccuracy arising from such simplification; however, the simplification allows us to obtain a closed-form solution. A simplified honeycomb structure is analysed as it provides a benchmark to the behaviour of this class

of structures. All the generic features of stent structures undergoing plastic deformation and recoil are present in this lattice structure under consideration.

The chapter is organised as follows. An analytical method to calculate the non-linear response due to elasto-plastic cell wall bending is formulated in the next section. This accounts for partial plasticity through the thickness and along the length of a cell wall. Following this, a method of calculation of springback upon removal of external in-plane load is presented. Illustrative examples and the relevant discussions are taken up in Section 2. Finally, concluding remarks are made in Section 3.

3.1 Cell wall plasticity and the apparent response of lattices

Consider an infinite two-dimensional cellular sheet, which is loaded remotely by a uniaxial stress (σ_∞) as shown in figure 3.1 (a). While the state of stress in any real structure is three dimensional, it is reasonable to treat the problem as one of plane stress when the thickness direction is significantly smaller that the typical dimensions within the plane. Further, for thin cell walls, one-dimensional models are adequate. The constituent cell wall material is assumed to be elastic-perfectly-plastic, thus no hardening occurs beyond yield; the stress-strain relationship is idealised in figure 3.1 (b). Here E is the Young's modulus and σ_y the yield stress of the cell wall material. The geometric parameters of the honeycomb are defined in figure 3.1 (c). In many practical honeycombs, the thickness of the vertically aligned cell walls is $2t$ which results from manufacturing considerations, as such honeycombs are often fabricated by bonding several sheets of the material together with periodically placed gaps and pulling them apart to form honeycombs. However, we restrict our attention to honeycombs of equal cell wall thickness t, as also considered by Gibson and Ashby [33]; uniform cell wall thickness is also realistic for applications such as stents.

When a honeycomb is loaded with a uniaxial remote stress, the cell walls bend and stretch. A typical inclined cell wall before deformation is shown using the straight line AB in figure 3.2 (a). The stretch part of deformation is ignored here; the deformed shape taken by the cell wall is shown in figure 3.2 (a) using the curve AB'. This can be justified on the grounds that the topology of the lattice is kinematically mobile, leading to a bending dominated behaviour [21]. Significant stretch will be present for $\theta \to 0^\circ$; we have ignored such extreme cases and results are presented for $\theta > 15^\circ$. In the following sections, we obtain analytical results based on this simplification that agree well with computations which include stretch–thus justifying the approach. The so-called $P-\delta$ effect is also neglected. Its exclusion does not affect the results in the subsequent sections–this is confirmed by comparing analytical response against numerical computations, where this is account for.

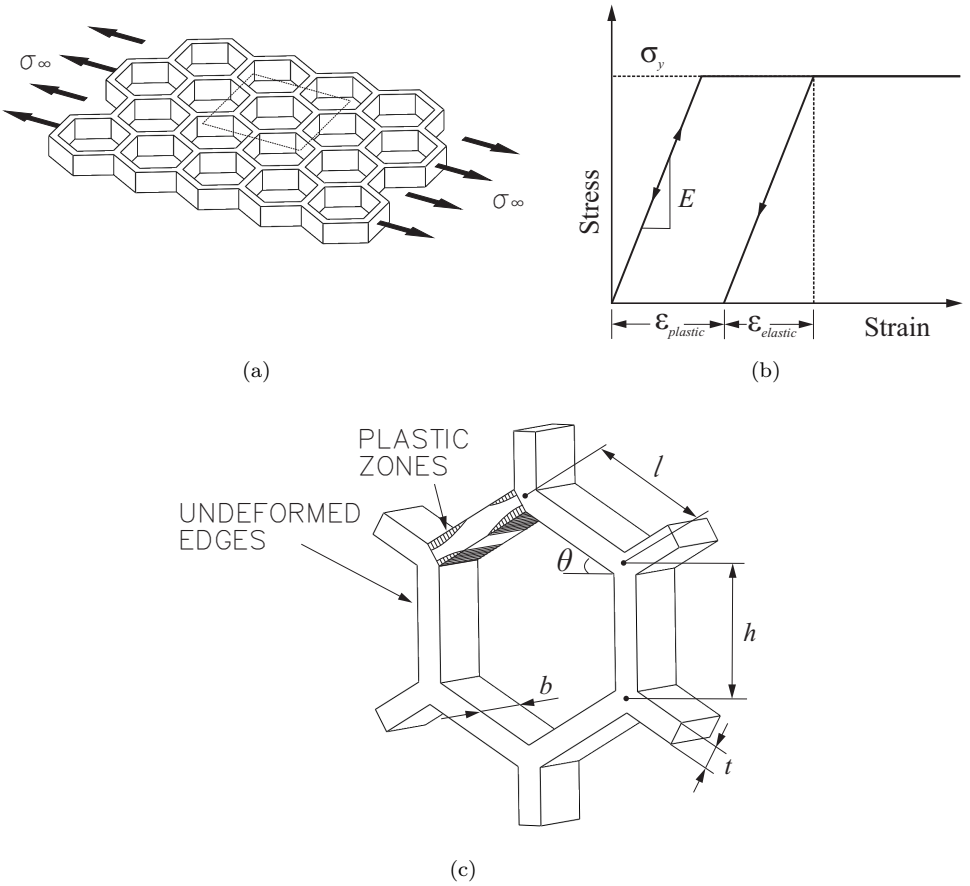

Figure 3.1: (a) An infinite honeycomb sheet, loaded remotely as shown, (b) Stress-strain relationship that describes the material behaviour of the cell walls (c) geometric parameters associated with a typical hexagonal cell.

The free body diagram of a typical inclined cell wall is shown in figure 3.2 (*b*). The remote stress σ_∞, parallel to the x-direction (horizontal), is applied to an infinite honeycomb sheet. Mirror symmetry about the vertical cell walls, combined with equilibrium, dictates that the force along the y-direction F_y must be equal to zero. The force along the x-direction F_x and the moment M at location ξ along the length are respectively given by [3]

$$F_x = \sigma_\infty (h + l\sin\theta)b \quad \text{and} \quad M = F_x \sin\theta l(\xi - 1/2). \tag{3.1}$$

Here, b is the depth of cell walls perpendicular to the plane of the honeycomb and $0 \leq \xi \leq 1$, $\xi = x/l$, is the non-dimensional coordinate along the cell wall.

Plasticity introduces non-linearity in the response. While many engineering problems require analysis to ensure stresses below the plastic limit, in applications such as the deployment of biomedical stents, or crash during impact, a detailed knowledge of the energy absorbed during the plastic phase of deformation is required. Further, there is

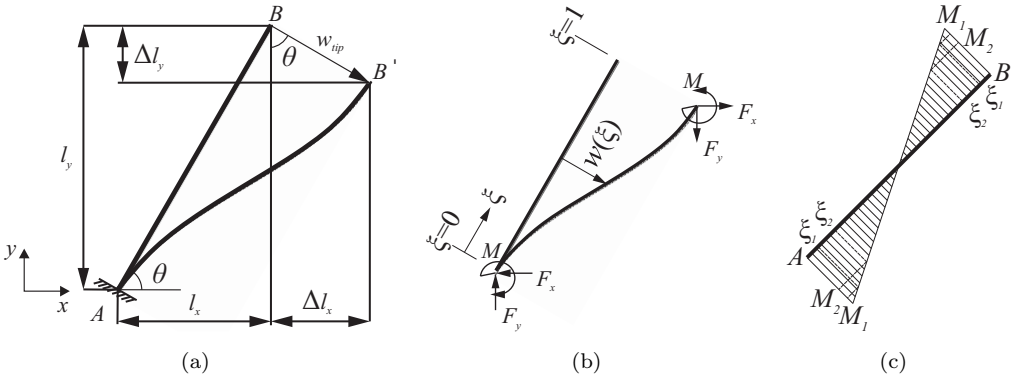

Figure 3.2: (a) Cell wall bending under remote horizontal stress applied in the x-direction. A typical undeformed cell wall is denoted by the inclined straight line AB. The deformed state of the same cell wall is shown by the curve $AB\prime$ when plotted in a coordinate system attached to the root; (b) Free body diagram of an inclined cell wall under remote stress; (c) Bending moment distribution along a cell wall AB.

no practical interest in response beyond collapse–the point when the cross-section of a cell wall becomes fully plastic. In case of tubular lattice structures such as stents, this corresponds to the collapse pressure: again beyond which there is no practical interest. Hence the analysis presented here is restricted up to the point when the collapse mechanisms are formed, and no further.

The usual assumptions of thin beam theory are accepted here. Firstly, plane cross-sections are assumed to remain plane upon bending. Secondly, the length of the cell wall l is much greater than the cross-section dimensions; therefore, shear deformation can be ignored. The current approach uses the stress distribution across each cross section to calculate the curvature, which is then related to the deflection. The symmetry of the geometry dictates that the deformed cell walls have a point of inflection at mid-length. Being an inflection point implies that $\partial^2 w/\partial \xi^2 = 0$ and, therefore, the absence of bending moment at the respective cross section. Here $w(\xi)$ is the deflection of the cell wall at ξ transverse to the cell wall orientation. Thus half of the cell wall reduces to a problem of elasto-plastic bending of a cantilever beam with tip loading which has both axial and transverse force components, but is moment-free. Again, the symmetry ensures that the cell wall joints do not rotate during the deformation due to the remote stress.

Cantilever beams under plastic deformation and springback have been previously studied by Yu and Johnson [67] in the context of forming of sheet metal parts. The calculation of the load-curvature relationship for a cantilever beam subjected to a tip load at arbitrary inclination, can now be adapted to obtain the response of lattice structures subjected to remote stresses. The distribution of the bending moment along the cell walls due to remote loading needs to be calculated first. The cell walls are subjected to a concentrated force and a flexural moment at the two ends, as shown in figure 3.2 (b). The bending

moment distribution along a cell wall AB caused by the applied loads is shown in figure 3.2 (c).

The maximum bending moment along the length of the cell wall appears at the two extremes and is given by

$$M^* = F_x \sin\theta(l/2) = \sigma_\infty bl \sin\theta(h + l\sin\theta)/2. \tag{3.2}$$

The shape of the plastic zone within the cell walls can now be analytically calculated, once we realise that there are three qualitatively different distributions over a cross-section possible (see e.g. Johnson [67]). The extent of plasticity depends upon the combinations of M, the bending moment at any cross-section along the cell wall, and N, the axial force. Figure 3.3 shows the three possible distributions of the elastic/plastic regions through the thickness of a cell wall: (1) completely elastic stress distribution, (2) primary plastic stress distribution: here yield occurs only on one side of the beam (PI), and (3) secondary plastic stress distribution: here yield occurs on both sides of the beam (PII).

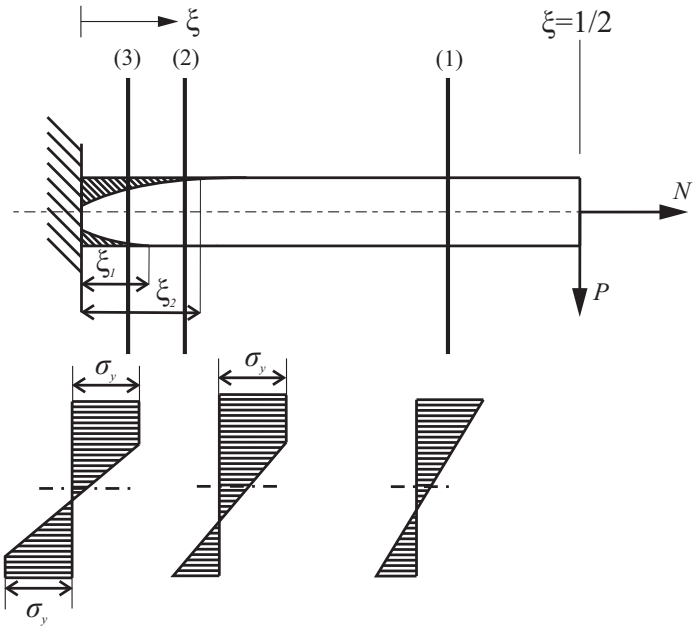

Figure 3.3: Half of a cell wall modelled as a thin beam simultaneously in flexure and axial tension. The coordinate system is attached to the left end. Note the depth of penetration of plasticity varies along the length and through the thickness of the cell wall giving rise to the shape of the plastic zone as schematically shown. The through-the-thickness stress distribution is shown at three cross-sections along the length at stations (1), (2) and (3).

All the fibres running parallel to the cell wall do not plastically deform simultaneously which leads to the formation of plastic zones of non-trivial shape within cell walls. When a cross-section is partially plastic, outer fibres plastically deform but the inner fibres remain elastic. The two plastic regimes can be identified in the cell walls via

cross-sections labelled (2) and (3) respectively, as shown in figure 3.3. Parts of the cell wall remain completely elastic–a typical section is denoted by (1) in the figure. Note that ξ_1 and ξ_2 represent the boundaries of the primary and secondary plastic regimes along the inclined cell wall. Thus $\xi > \xi_2$, $\xi_1 \leq \xi \leq \xi_2$, $0 \leq \xi \leq \xi_1$ are the regions of completely elastic, PI and PII deformations respectively. Since the force F_x is inclined at an angle θ to the horizontal, the shear and the axial components of the force at the end are given by

$$\begin{cases} P = F_x \sin\theta = \sigma_\infty \sin\theta (h + l\sin\theta) b \\ N = F_x \cos\theta = \sigma_\infty \cos\theta (h + l\sin\theta) b. \end{cases} \tag{3.3}$$

Having established the relationship between the lattice parameters and the remote stress with the forces and moments at the centre of the span of a cell wall, we are now in a position to work out the elastic and plastic response.

Since the centre of a cell wall, at $\xi = 1/2$, is a moment-free point, the analysis of [67] becomes applicable. The load-curvature relationship is given by [67]

$$\begin{aligned} \phi &= m && \text{for fully elastic} \\ \phi &= 4(1-n)/\left(3 - \frac{m}{1-n}\right)^2 && \text{for } PI \\ \phi &= 1/\sqrt{3(1-n^2) - 2m} && \text{for } PII \end{aligned} \tag{3.4}$$

where $m = |M|/M_e$ is the non-dimensional moment, $n = |N|/N_e$ is the non-dimensional axial force and $\phi = |\kappa|/\kappa_e = \left|\partial^2 w/\partial\xi^2\right|/\kappa_e$ is the non-dimensional curvature. $M_e = \sigma_y b h^2/6$, $N_e = \sigma_y b h$, $\kappa_e = 2\sigma_y/(Eh)$ are the reference quantities for moment, axial force and curvature. Expressions for n and m^*, the dimensionless value of m at the root of a cell wall, are given by

$$\begin{aligned} n &= (\sigma_\infty/\sigma_y)\,[1 + (l/h)\sin\theta]\cos\theta \\ m^* &= 3(\sigma_\infty/\sigma_y)(l/h)\sin\theta\,[1 + (l/h)\sin\theta] \end{aligned} \tag{3.5}$$

which depend on the remote stress and the geometry of the lattice as well as that of cell walls. The value of the axial force n remains unchanged along the length of a cell wall. Equation (3.4) represents a set of three second order linear differential equations due to the presence of the term $\phi = \left|\partial^2 w/\partial\xi^2\right|/\kappa_e$, each valid for the three separated regions. In order to calculate the cell wall deflection, the above expressions in equation (3.4) must be integrated in each region and the boundary conditions at the left end need to be used to solve the differential equations. The stress distribution is asymmetric with respect to the centre of the beam. Therefore, the deflection along the whole beam under elasto-plastic loading can be obtained by integrating equations (3.4) along half of the beam and then reflecting the solution onto the remaining half, noting the two-fold rotational symmetry of the deflected shape.

Having considered the mechanics of an individual cell wall, the apparent elasto-plastic response can now be calculated analytically for the complete lattice. Apparent properties of a porous or lattice material are those that describe the behaviour of structural material as if the lattice were filled with homogeneous matter possessing these properties. Such properties are denoted within angular brackets in subsequent discussions. The change in the overall vertical and horizontal dimensions, when a uniaxial load is applied at infinity, are related to the projections of the tip displacement along the horizontal and vertical directions of cell walls, as shown in figure 3.2 (a). The horizontal and vertical projections of a cell wall, before the application of remote stress, are l_x and l_y, respectively. The changes in projections of the deformed cell wall upon the application of remote stress are denoted respectively by Δl_x and Δl_y. The stretch deformation is ignored, therefore the length of the cell wall is unchanged. Axial stretch of the cell walls is ignored even though the effect of axial force in shifting the neutral axis is included in our subsequent calculations. Therefore the segment BB' in figure 3.2 (a) is perpendicular to the undeformed cell wall orientation. As stated in the introductory section, geometric non-linearity resulting from non-linear strain displacement relationship in the cell wall bending kinematics is ignored too. When verified numerically, this approximation turns out to be good.

Using the tip deflection expression developed in [67], changes in the projections of an inclined cell wall, along and across the application of the load, can be calculated as

$$\begin{aligned}
\Delta l_x &= \frac{4l^2\sigma_y}{hE}\left\{\frac{1}{6}m^*[2-\xi_2^2(3-\xi_2)] + \left\{\tfrac{m^*}{2}\left[1-\left(\frac{1-n}{m^*}\right)^2\right] + \left(\frac{\mathrm{d}\eta}{\mathrm{d}\xi}\right)_2\right\}(1-\xi_2)+\eta_2\right\}\sin\theta \\
\Delta l_y &= \frac{4l^2\sigma_y}{hE}\left\{\frac{1}{6}m^*[2-\xi_2^2(3-\xi_2)] + \left\{\tfrac{m^*}{2}\left[1-\left(\frac{1-n}{m^*}\right)^2\right] + \left(\frac{\mathrm{d}\eta}{\mathrm{d}\xi}\right)_2\right\}(1-\xi_2)+\eta_2\right\}\cos\theta
\end{aligned} \tag{3.6}$$

where η_2 and $\left(\dfrac{\mathrm{d}\eta}{\mathrm{d}\xi}\right)_2$ represent the normalised transverse displacement and rotation of a cell wall at ξ_2, where $\eta = wtE/(2l^2\sigma_y)$ is the non-dimensional transverse displacement. These changes in the projection of the cell wall along and across the loading, given by Δl_x and Δl_y respectively, are implicit functions of the remote stress σ_∞ via expressions (3.5) for n and m^*.

An expression for the displacement transverse to a cell wall can be found for each point along the cell wall. Each combination of n and m results in a different cell wall stress distribution. Therefore, a different load-curvature expression from the three cases in equation (3.4) must be used while integrating the curvature relationships. The change in the overall dimensions of the lattice is completely determined by the tip displacement of the inclined cell wall and the lattice geometry. Thus, the calculation of the tip displacement of an inclined cell wall is a crucial part of the present analysis. The apparent strains in directions parallel and perpendicular to loading, as functions of the

remote stress σ_∞ and the lattice parameters, are given by

$$\epsilon^{\parallel}_{\text{app}} = \sqrt{\Delta l_x^2 + \Delta l_y^2}\tan\theta/l \quad \text{and} \quad \epsilon^{\perp}_{\text{app}} = 2\sqrt{\Delta l_x^2 + \Delta l_y^2}\cos\theta/(2l\sin\theta + h). \tag{3.7}$$

Here $\sqrt{\Delta l_x^2 + \Delta l_y^2} = w_{\text{tip}}$ is the deflection of the tip of a cell wall with respect to the root. The above is a closed form analytical expression for the functional form $\epsilon^{\parallel}_{\text{app}}(\sigma_\infty)$ and $\epsilon^{\perp}_{\text{app}}(\sigma_\infty)$ which relates remote stress σ_∞ to the components of the apparent strain of the cellular sheet, in the direction of, and lateral to, loading. The remote stress implicitly appears inside the expressions for $\Delta l_x(m^*, n)$ and $\Delta l_y(m^*, n)$ which, in turn, contain the remote stress within the expressions for $m^*(\sigma_\infty)$ and $n(\sigma_\infty)$.

The above development is generic for any lattice having the geometry of a cell described by figure 3.1 (c). This includes negative angle θ which provides us with the interesting opportunity to examine the elasto-plastic response of lattices with apparent auxetic behaviour in the post-plasticity regime of deformation.

The springback behaviour of infinite lattices can now be analytically assessed by considering the unloading scenario. The elastic recovery is via a linear path parallel to the loading curve on the stress-strain plane. Since different points within the lattice are at different levels of plasticity, the residual plastic deformation has a spatial distribution within the honeycomb. In order to calculate the springback of lattice materials analytically, unloading of the bent cell walls must be taken into consideration to determine their final curvature. As previously done for the loading calculations, the unloaded configuration of the key points on the lattice can be calculated by focussing the attention to the tip deflection of a bent cell wall upon elastic recovery. The elastic deflections corresponding to the moment applied at a section must be subtracted from the deflections before unloading. The x- and y-components of the permanent tip deflection of the cell wall with respect to its root are thus given by

$$\begin{aligned} w_x^{\text{permanent}} &= \Delta l_x - 2/3(m^* l^2 \sigma_y)/(tE)\sin\theta \\ w_y^{\text{permanent}} &= \Delta l_y - 2/3(m^* l^2 \sigma_y)/(tE)\cos\theta \end{aligned} \tag{3.8}$$

where the first term in each of the two expressions is given by equation (3.6). After removal of the external load, the residual stress distribution over a cross-section must be self-equilibrated.

3.2 Results and discussions

Graphical presentation of analytical results as well as computational verifications for response in the plastic range, springback and recoil, lateral response leading to apparent Poisson's contraction for elasto-plasticity, parametric trends, and generic scaling

arguments are provided in this section. The effect of ignoring stretch deformation, in order to facilitate analysis in the previous section, is also brought out. These results are organised into several subsections with relevant discussions contained there in.

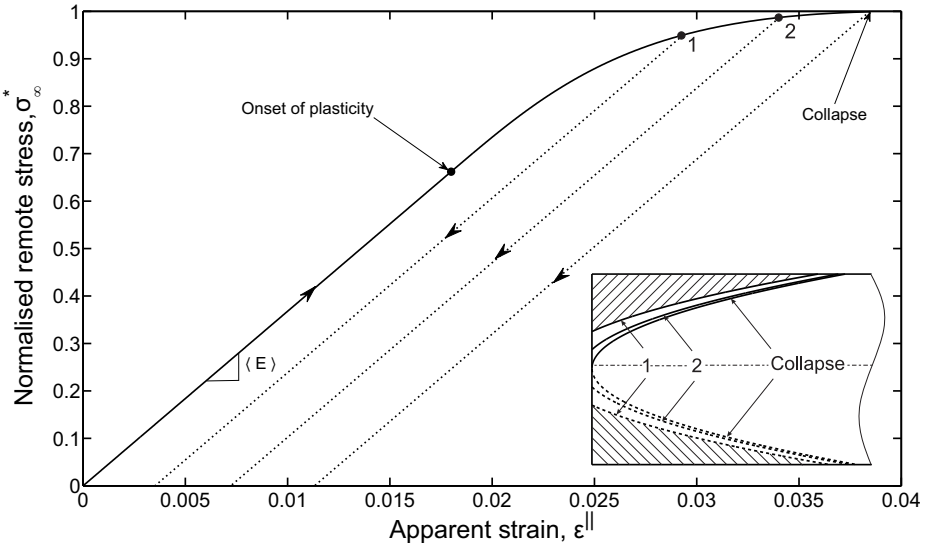

Figure 3.4: Tensile stress-strain curves for an infinite honeycomb sheet subjected to a remote uniaxial stress along the x-direction. The normalised stress $\sigma^*_\infty = \sigma_\infty/\sigma_{\text{Collapse}}$ is plotted against the apparent strain parallel to the direction of the application of the load. The slope of the apparent stress-strain curve equals the apparent Young's modulus $\langle E \rangle$ of the lattice; the tangent modulus diminishes beyond yielding.

3.2.1 Non-linear elasto-plastic response of honeycombs

Having developed analytical expressions for the response of a honeycomb sheet beyond yielding–by incorporating elasto-plastic response of thin cell walls into the calculation, we are now in a position to quantitatively present the apparent non-linear response of such structured material. When remote stress is applied, the initial phase of the response will be purely elastic, as the cell walls are under completely recoverable elastic deformation. In this phase, remote stress varies linearly with the apparent strain in the direction of the applied loading–the slope being a measure of the apparent Young's modulus $\langle E \rangle$ of the honeycomb. This behaviour is well documented and thoroughly studied in the past by Gibson *et al.* [3; 33]. The apparent modulus of elasticity was calculated using the implicit but closed form equation (3.6) for low values of remote stress such that all material points on the honeycomb are within the elastic limit. The response in this part is expected to be non-linear due to plasticity and is reported here for the first time. This requires turning the displacements into apparent strain quantities (using equation (3.7)). The values thus obtained for the apparent modulus match extremely well (up to 4 significant figures) with the well known benchmark results (Gibson and Ashby [33]).

This provides a validation for the more general expression developed in this chapter up to the point of transition to plasticity. The part of the curve in figure 3.4 from the origin up to the point labelled 'onset of plasticity' represents this validation.

Consider now an infinite regular lattice shown in figure 3.1 (a) subjected to a remote in-plane stress along the x-direction such that cell walls yield beyond the elastic limit. Equation (3.6) together with equation (3.7) can be taken as the apparent stress-strain relationship for the honeycomb under plastic deformation. This implicit but analytical relationship requires eliminating Δl_x and Δl_y. The remote stress σ_∞ enters (3.6) *indirectly* via the terms m (whose maximum value along the cell wall length is m^*) and n according to the expressions in equation (3.5). The results of these calculations are shown in figure 3.4, where the stress at infinity has been normalised with respect to the collapse stress $\sigma_\infty/\sigma_{\text{Collapse}} = \sigma^*_\infty$; the collapse stress is the value of the remote stress which corresponds to the cell wall cross-section at the joints becoming fully plastic. The generic feature of this curve is an initially linear elastic phase extending up to the onset of plasticity followed by a non-linear regime. Note also that the tangent modulus at the onset of plasticity shows continuity, i.e. the apparent stress vs apparent strain curve is smooth at the transition from elasticity to plasticity. This is in contrast with the constitutive law for the parent material which shows discontinuity of tangent modulus at the point of yielding. This is because, while the material stress-strain curve is not differentiable at the point of elastic-to-plastic transition, the strain energy density is continuous with respect to material strain and the evolution of plastic zone is without a jump. This leads to smoothness (hence differentiability) of the remote stress with respect to apparent strain for the lattice. In other words, the whole structure does not become plastic simultaneously; so despite discontinuity in the tangent modulus of the parent material, the apparent modulus of the cellular solids is continuous.

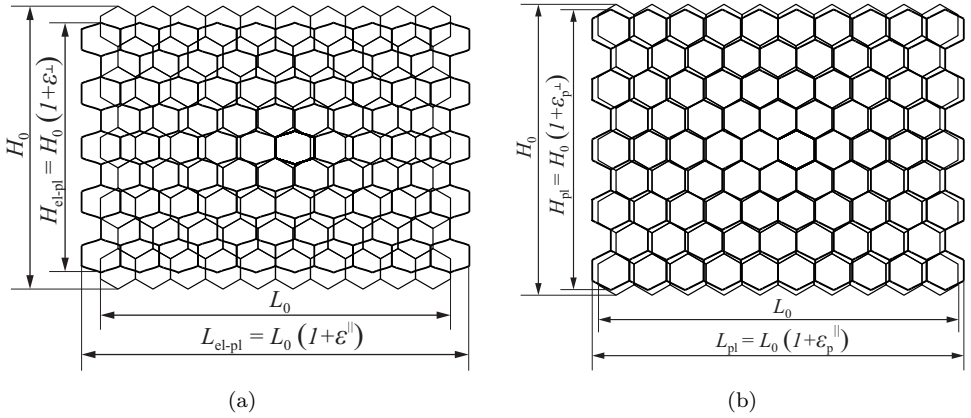

Figure 3.5: (a) Elasto-plastic deformation of an infinite honeycomb sheet subjected to a remote tensile stress along the x direction. (b) Spring back of the same sheet as in (a)–note that the horizontal shrinkage is accompanied by a lateral extension during springback.

Two arbitrary points along the apparent stress-strain curve are marked in figure 3.4 (labelled '1' and '2'). The corresponding contours of elastic-plastic region boundaries are shown in the inset for a section of the cell wall. The three sets of contour lines labelled '1', '2', and 'Collapse' correspond to the corresponding labelled points on the apparent stress-strain curve. The solid lines in the inset are associated with tensile stress whereas the dotted lines with compressive stress. These lines denote the boundary between the elastic region and the plastic region for different phases of plasticity. All points between these curves and the outermost fibres are plastic. Curves above and below the neutral axis show a minor asymmetry which is apparent on closer inspection–the reason for asymmetry being the presence of axial loading on the compressive side and the tensile side of flexural response, thus changing the stress distribution over the cross-section that lacks symmetry with respect to loading. The deformed shape of the lattice as calculated for the non-linear plastic regime is shown in figure 3.5 (a).

When the remote stress is further increased, the apparent tangent modulus continues to decrease until the cross-section at the root of a cell wall becomes completely plastic. The total moment at this cross-section equals that corresponding to a plastic hinge. We would refer to this remote stress as the collapse stress because the lattice is unable to resist any greater remote stress. The remote stress corresponding to collapse was given by Gibson and Ashby [3] and the values obtained here confirm this. However, the non-linear curve bridging the linear part of the response to the point of collapse has not been reported before. The present work fills the gap between the previously known elastic limit and the completely plastic extreme via new results in the non-linear response range as well as recoil. This is further characterised qualitatively and quantitatively in the subsequent sections. Further, the non-linear part of the curve is critical in the determination of springback, also reported here for the first time.

3.2.2 Unloading and recoil

Consider now the unloading problem from the post-plasticity phase. Frequently one needs to quantitatively assess the permanent strain and deformation after a piece of lattice material has undergone plastic deformation. For example, for repetitive structures such as cardiovascular stents, there is a need to know the recoil of the structure post-plastic phase in order to know the shape of the medical device after its deployment. The apparent stress-strain curve of the lattice is dependent on the unloading path on the material law of the parent material as well as the lattice geometry. Assuming the strain recovery to be linear and parallel to the loading path on the material curve, the residual apparent plastic strain and springback of the lattice are calculated here. They are shown using dotted lines with an arrow in figure 3.4. The return shows a path parallel to the loading curve with a slope equal to the apparent modulus of elasticity. This is expected because the recovery has been assumed to follow a linear stress-strain

law with the modulus of elasticity the same as that of a the parent material in the cell walls. Consider that the remote stress is now removed. The deformation related to the elastic part is recovered; therefore only the permanent plastic deformation remains within the structure. The final shape after the springback is shown in figure 3.5 (b).

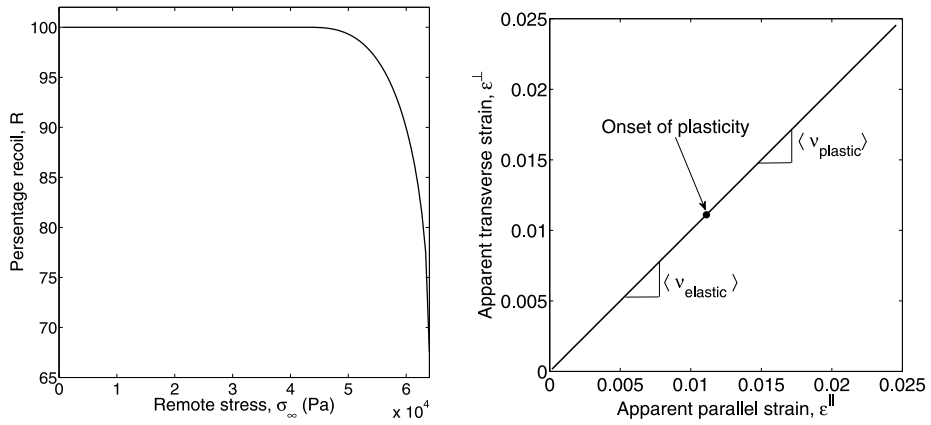

(a) (b)

Figure 3.6: (a) Percentage recoil for a honeycomb sheet loaded remotely along the x-direction. (b) The dependence of the apparent lateral strain $\epsilon^{\perp}$ on the apparent longitudinal strain $\epsilon^{||}$. The slope that represents the apparent Poisson's ratio $\langle\nu\rangle$ of honeycomb is same and constant in elastic and plastic regimes. The geometric parameter of the lattice are $h/l = 1$ and $t/l = 0.02$ where $l = 1$m, $\theta = 30°$, $E = 209$ GPa, $\sigma_y = 240$ MPa.

In order to quantify the springback of a lattice, it is useful to define the percentage recoil R for a lattice as

$$R = \left(\frac{L_{\text{el-pl}} - L_{\text{pl}}}{L_{\text{el-pl}} - L_0}\right) \times 100. \tag{3.9}$$

Here L_0 is the initial length of the sheet, $L_{\text{el-pl}}$ the length of the hexagonal sheet when loaded at infinity and L_{pl} its length upon removal of the load, thus only plastic deformation remains within the structure. Having taken a unit cell approach, the expression for R obtained here is valid for an infinite lattice. This parameter has been plotted in figure 3.6 (a). Recoil is observed along as well as across the loading-unloading directions. Lateral response and recoil are discussed next.

3.2.3 Apparent Poisson-contraction during plastic deformation

The longitudinal and lateral responses, as well as percentage recoil, are found to be equal for a regular hexagonal lattice. This is a manifestation of the fact that the apparent Poisson's ratio equals 1 for regular hexagonal honeycombs. The apparent stress-strain curve along the direction perpendicular to the application of the load is not shown here

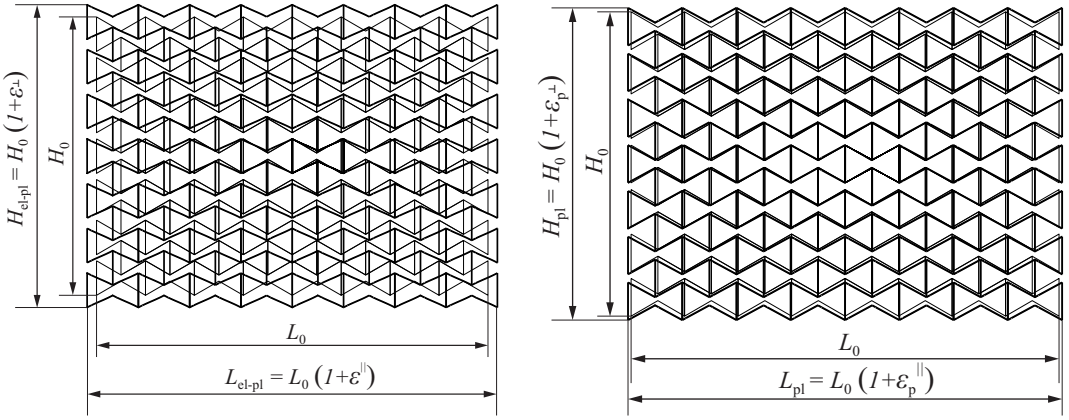

Figure 3.7: (a) Deformation of an auxetic lattice structure through plastic phase when tensile loading is applied in the horizontal direction. Note the accompanying lateral expansion. (b) Spring back upon release of load showing longitudinal as well as lateral contraction.

as it shows a behaviour very similar to that of figure 3.4, except that the strain is negative indicating that the structure *shrinks* laterally.

The apparent Poisson's ratio is defined as the negative of the ratio of the lateral strain to the the applied strain

$$\langle \nu \rangle = -\frac{\epsilon^{\perp}}{\epsilon^{\parallel}} = -\frac{\Delta l_y}{l_y}\frac{l_x}{\Delta l_x}, \tag{3.10}$$

where the changes in the projection of the inclined cell wall Δl_x and Δl_y in the x- and y-directions are respectively given by

$$\Delta l_y = w_{\text{tip}} \cos\theta \quad \text{and} \quad \Delta l_x = w_{\text{tip}} \sin\theta, \tag{3.11}$$

where w_{tip} is the deflection of an inclined cell wall relative to its root transverse to the inclination of the cell wall (figure 3.2 *a*)–the common leading terms between the two expressions in equation (3.6). Gibson *et al.* [3] showed that the apparent Poisson's ratio $\langle \nu \rangle$ during linear elastic response equals 1 for regular hexagonal honeycombs. Under elastic deformation, the apparent Poisson's ratio is completely independent of the constituent material properties for thin walled cellular solids as argued by Bhaskar [117]. It is not obvious as to how the apparent Poisson's ratio $\langle \nu \rangle$ would change in the non-linear plastic regime of deformation.

Dimensional and scaling arguments, in situations where exact answers are difficult to obtain, are often very effective [118; 119]. Following the approach in [117], the tip

deflection of a cell wall with respect to its root w_{tip} has the functional form

$$w_{\text{tip}} = f(\text{geometry}, E, \nu), \tag{3.12}$$

while the lengths along the x- and the y-direction are dependent on the lattice geometry, i.e.

$$l_x = f(\text{geometry}) \quad , \quad l_y = f(\text{geometry}). \tag{3.13}$$

From equations (3.10) and (3.11), it is apparent that the tip displacement w_{tip}, which depends on the material properties, is cancelled out from the expression of $\langle\nu\rangle$. Therefore the apparent Poisson's ratio becomes a function entirely of geometric parameters l_x, l_y, $\sin\theta$ and $\cos\theta$. Thus the dimensional argument combined with the kinematics and mechanics of cell wall deformation dictate the apparent Poisson's ratio should be the same as that for the elastic limit lattice response, which is known to be equal to 1. This is confirmed by the detailed calculations as shown in figure 3.6 (b) which shows the transverse strain as a function of the longitudinal strain–the slope of this curve being unity for the entire range of elasto-plasticity.

3.2.4 Plastic response and springback of *auxetic* lattices

Most real materials exhibit positive Poisson's ratio as the material shrinks in the direction lateral to the that of loading. However, there has been recent interest in structured material that show apparent negative Poisson's ratio. Such material, when loaded in one direction, respond by expanding in the lateral direction and are known as *auxetic* [120; 121]. Simple models of auxetic planar material can be constructed by rendering the hexagons to be non-convex. This is easily achieved by allowing the angle θ in figure 3.1 (c) to be negative. When such a structure is subjected to tensile remote stress, it will simultaneously extend along, and lateral to, the direction of loading. The elastic response of such auxetic material can be predicted using the theory previously presented by Gibson and Ashby [3], later enhanced by Masters and Evans [122]. Here we present the *elasto-plastic response* of such auxetic lattice in figure 3.7 (a). The apparent stress-strain curve can now be calculated analytically (not shown for sake of brevity); it has trends similar to those of non-auxetic lattices–there is a proportional regime of completely recoverable elasticity followed by a softening part that is continuous and differentiable, despite the constitutive relationship for the parent material of the cell walls being piece-wise linear. Upon release of the remote stress, the springback also shows auxetic behaviour in that the lattice shrinks in *both* directions simultaneously (see figure 3.7 b).

When auxetic honeycombs are stretched or compressed in a given direction, the apparent lateral strain is tensile or compressive respectively. This does not mean that each cell

wall is in axial compression. Hence buckling of cell walls is not considered as bending continues to be only dominant mechanism of cell wall deformation. This would not be the case, however, if the material is laterally constrained. Constraint can lead to structural buckling–a situation kept out of consideration in the present work, but analysed in the last chapter.

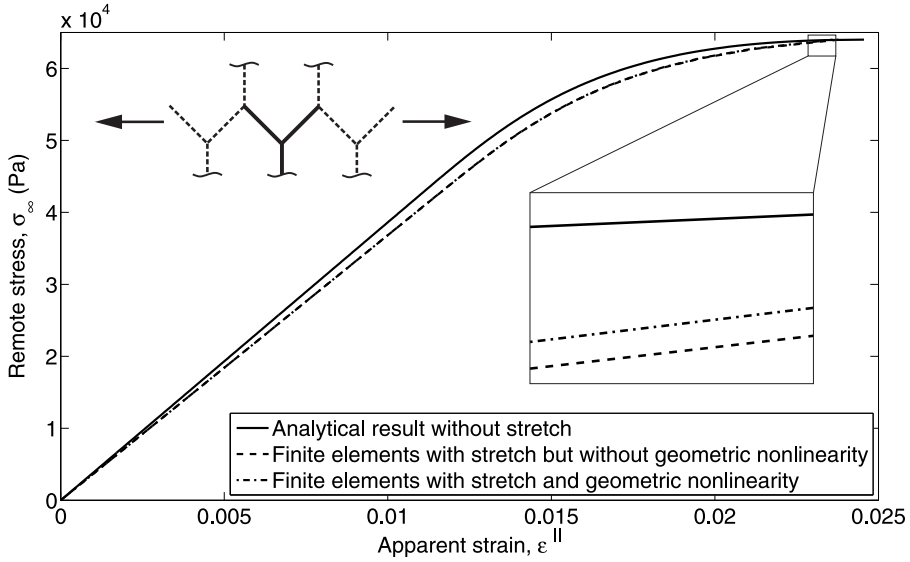

Figure 3.8: Remote stress as a function of the apparent lattice strain. The solid line refers to the analytical results which ignore the stretch and the geometric non-linearity. The effect of stretch (dashed line) and the geometric non-linearity (chain line) are negligible for thin cell walls.

3.2.5 The effect of cell wall stretch and geometric non-linearity

The model of cell wall plasticity developed here ignores stretch. It proves to be technically cumbersome to include the stretch deformation when the deformation is plastic because of the invalidity of the superposition principle for non-linear response. However, the effect can be easily assessed computationally and this is presented in figure 3.8. The solid line represents the analytically calculated plastic response of a lattice for the elastic-perfectly-plastic material model ignoring stretch and geometric non-linearity. The dashed line in the figure represents computational results based on a unit cell (as shown in the inset; note that hexagon is not a unit cell). The agreement between the analytical results presented here and the computational results which make use of finite elements is excellent for the whole range of elasto-plastic response up to the point of collapse. The unit cell has been modelled as a 3D structure using the element type C3D8I (8-node brick element) within the commercial code ABAQUS. This element has geometric as well as material non-linearity capability which could be switched on or off at will. The number of degrees-of-freedom per node is 3 and the total number of elements over 25,000 which was arrived systematically by increasing this till convergence

was achieved well within 1%. The geometric parameters of the lattice are $h = l = 1$ mm, $b = t = 0.02$ mm, $\theta = 30°$. The material parameters are $E = 209$ GPa and $\sigma_y = 240$ MPa. It is interesting to note that the absence of stretch in the model overestimates the apparent stress required for the specified value of apparent strain up to the collapse.

Consider next the role of geometric non-linearity as it may be argued that it could have impact on the response of lattice structures loaded remotely. An overall stiffening of the structure due to geometric non-linearity is observed in the inset of figure 3.8 as the curve corresponding to the inclusion of geometric non-linearity *in addition to* stretch is slightly higher than that when only stretch is considered (the chain line). These calculations are carried out on a unit cell. For the lattice parameters considered here (cell wall length to thickness ratio approximately equal to 25), stretch appears to have a far greater influence on the response than the geometric non-linearity. This justifies our initial assumption of ignoring geometric non-linearities from the analysis.

Having briefly considered higher order effects and their role in lattice elasto-plastic response, we now return to the main purpose of the chapter which is to study in detail the plasticity of such structured material.

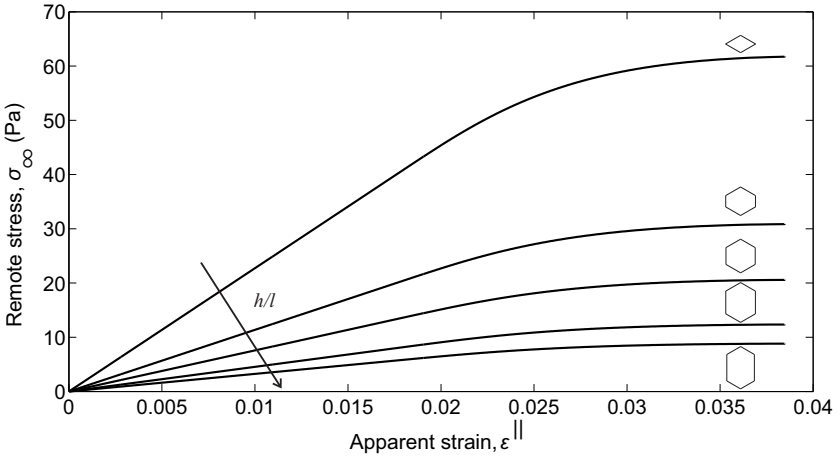

Figure 3.9: The effect of h/l ratio on the elasto-plastic response of hexagonal lattices.

3.2.6 The dependence of plastic behaviour on lattice parameters

The analytical approach developed here affords results for lattice structures in a closed form. A reward of such an analysis is not only to have a benchmark result (under the assumptions of the model), but also the ability to infer trends of the behaviour and their dependence on the parameters of the problem–as opposed to computations and laboratory experimentation that obscure this insight. On the other hand, both computational and physical experiments are extremely useful in suggesting the dominant

features of the behaviour, in addition to guiding the analysis, in order to retain the most significant aspects of a problem within a model. In this spirit, we carry out numerical calculations first and then propose a scaling ansatz which unifies the bending dominated lattice behaviour under plastic deformation.

The influence of the ratio of the height h and the length of the cell wall l is now studied while keeping all other material and geometric parameters held constant. By increasing the h/l ratio in steps of $h/l = 0, 0.5, 1, 2, 3$, while other material and geometric parameters of the lattice are held constant at $t/l = 0.012$, $\theta = 30^o$, $E = 209$ GPa, $\sigma_y = 240$ MPa, we observe that the stiffness of the lattice structure decreases, which is evident from figure 3.9. This provides us with design guideline for energy absorption applications that straight members should be minimised for greater energy dissipation. By contrast, the plastic deformation of rhomboidal cells occurs at a higher load, therefore in order to obtain the same amount of deformation as for honeycomb with longer straight vertical members, a higher load is required. Thus higher energy absorption comes with a price: the stiffness of the lattice becomes greater which is undesirable from the point of view of dynamic energy absorption because this leads to higher dynamic peak forces during impact. The trade-off between peak loads and the plastic energy absorption, that one frequently encounters in many crashworthiness application, is evident here too.

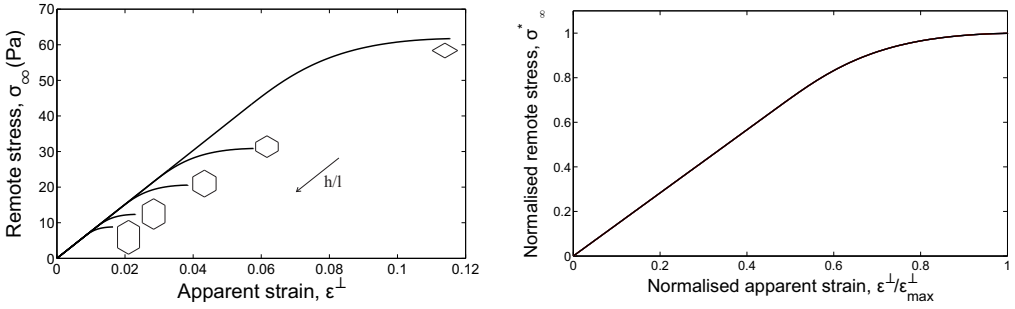

(a) (b)

Figure 3.10: (a) Plot of the remote stress σ_∞ against the lateral strain $\epsilon^\perp$ for increasing values of the non-dimensional ratio h/l. (b) The curves have been scaled with respect to their collapse stress and maximum strain–all the curves in (a) collapse to a single master curve in (b).

The effect of h/l ratio on the lateral response is shown in figure 3.10. Clearly, the apparent lattice properties are no longer isotropic. In the linear elastic range of deformation, the apparent Poisson's ratio and the apparent Young's modulus both scale similarly with (h/l) according to $(\langle\nu\rangle, \langle E\rangle) \sim (hl^{-1} + \sin\theta)^{-1}$. Thus, the ratio $\sigma_\infty/\epsilon^\perp$ becomes independent of h/l leading to a common slope for all the curves in the linear range in figure 3.10 (a). However, in the plastic regime, this is not valid. Cell wall yielding takes place at a lower level of apparent remote stress because a lower remote stress corresponds to a similar cell wall stress for greater h/l. This behaviour is observed from the numerical calculations and is presented in figure 3.10 (a). The shape of the curves in figure 3.10 (a)

appear to be similar. This is confirmed upon scaling the variables with respect to the maximum values of the lateral strain and the remote stress for each curve. The results are presented in 3.10 (b) which shows collapse of all the data on a single curve.

The role of thickness to length ratio of a cell wall t/l is investigated next. The ratio $h/l = 1$ is held constant, $\theta = 30°$, $E = 209$ GPa, $\sigma_y = 240$ MPa. The thickness to cell wall length ratio is now varied as $t/l = 0.0088, 0.0120, 0.0177, 0.0243$. For linear elasticity, it is well known that the apparent modulus scales according to $\langle E \rangle \sim (t/l)^3$. When non-linearity due to plasticity is present then this becomes non-trivial except for the collapse calculation where remote stress corresponding to collapse scales as per $\sigma_{\text{Collapse}} \sim (t/l)^2$. For the non-linear elasto-plastic phase the behaviour appears to be complex and the parametric dependence showing the effect of (t/l) on the apparent response is shown in figure 3.11 (a). The family of curves are drawn up to the point of collapse. As for the case of (h/l) ratio, the shape of the curves appears to be similar. Normalising the variables with respect to the values at collapse for each curve results in nearly identical curves–when superposed (see figure 3.11 b) the slight difference being attributed to the stretch deformation in cell walls.

3.2.7 Separation of lattice geometry from cell wall properties, scaling arguments and data collapse

Having considered hexagonal lattices for lattice geometries that differ in their lattice parameters such as l, h, and θ, we are now in a position to separate the cell wall mechanics from the kinematics of the lattice deformation. The similarity in the parametric trends of the apparent stress vs apparent strain of the elasto-plastic response of such structured material, as observed previously, suggests the existence of scaling of variables and an appropriate renormalisation. For the linear response of bending dominated cellular solids, the scaling of the apparent modulus of elasticity as per $\langle E \rangle \sim E(t/l)^3$ is not enough to collapse the non-linear deformation profiles to a single curve. The process of identifying *new stretch variables* for the apparent strain and the apparent stress is non-trivial. Because of a greater number of variables (e.g. the yield stress), this requires further arguments beyond dimensional homogeneity such as subtle physical reasoning and reasonable approximations. In a general situation, there is no guarantee that one would be able to be successful to obtain such renormalisation: when this is possible, it is both practically useful and theoretically unifying. Indeed, this is the case here as we will discover later in this section–the appearance of terms involving σ_y, t, l on scale factors for the apparent stress as well as apparent strain linked by *a complex non-linear relationship* highlights the need for aspects of physics of plastic deformation to be invoked in order to arrive at a scaling ansatz.

To develop scaling variables that collapse the non-linear response curves onto a single master curve, consider a cantilever beam with transverse tip force P, axial force N,

length L, thickness t and depth in the direction perpendicular to the plane of deformations b (see inset in figure 3.12). The elastic-perfectly-plastic constitutive relationship is described by *two material parameters*: the Young's modulus E and the yield stress σ_y. The tip deflection for this beam flexure problem is given by δ. The scaling arguments for linear elasticity of cellular solids with beam-like cell walls is straightforward and has been previously presented by Gibson and Ashby [3], Ashby [12], and Warner *et al.* [123]. Here we develop scaling relationships further for elasto-plasticity.

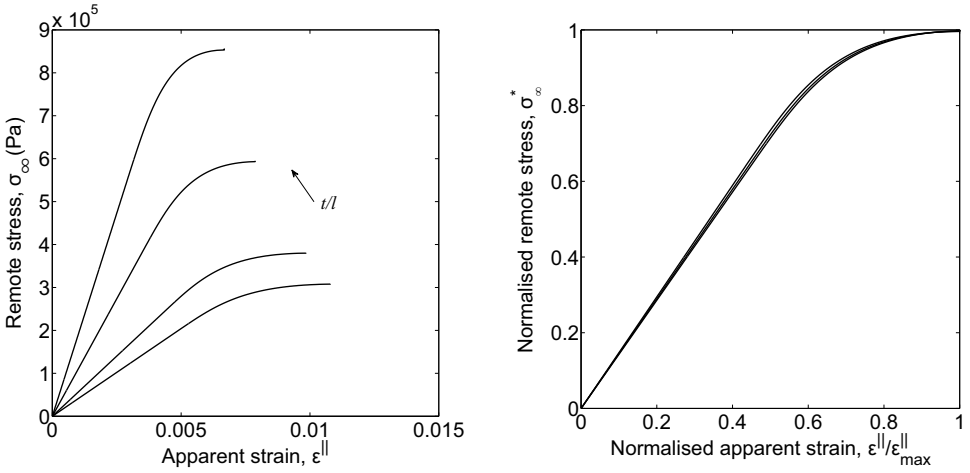

(a) (b)

Figure 3.11: (a) Effects of the ratio between cell wall thickness t and strut length l on the mechanical response of the lattice structure. (b) The curves have been scaled with respect to their collapse stress and maximum strain they approximately overlap onto each other.

Consider the functional relationship $\delta = \delta(P, N, E, \sigma_y, L, t, b)$, for a regular hexagonal honeycomb so that $h = l$, which is an 8-variable problem while applying Buckingham's π-theorem. The reduction in variables is by just two here (since the variables that do not form a π-group themselves are length and mass $\times$ length^{-2} which occurs in exactly the same form 4 times: in P, N, E, σ_y and must be counted just once). Therefore, the above functional relationship takes the following non-dimensional form

$$(\delta/L) = f_1\left((P/EL^2), (N/EL^2), (\sigma_y/E), (t/L), (b/L)\right). \tag{3.14}$$

Dimensional homogeneity cannot take us any further. We need simplifications, assumptions, and further physics in order to discover scaling laws–we will make use of them, in turn, now. (i) The assumption of bending dominance of the lattice architecture leads to δ/L becoming a weak function of (N/EL^2), i.e. $(\delta/L) = f_2\left((P/EL^2), (\sigma_y/E), (t/L), (b/L)\right)$. (ii) The scenario in the depth direction is identical in all the planes (i.e. the displacement field is independent of the depth direction for beam mechanics), therefore (P/b) determines the deflected shape completely. This requirement is satisfied by combining

the first and the last non-dimensional terms such that P/b appears together as a single π-number. This results in $(\delta/L) = f_3\left((P/bLE), (\sigma_y/E), (t/L)\right)$.

We still need further information to find t/L scaling. This is afforded by the beam curvature-bending-moment relationship

$$\kappa = \frac{\partial^2 w}{\partial x^2} \sim \frac{\sigma_y}{Et}\left[1 - \frac{Px}{bt^2\sigma_y}\right]^{-1/2} \tag{3.15}$$

where x is the local coordinate measured from the loaded end (see inset in figure 3.12). Since curvature $\kappa \sim \delta/L^2$ and the term inside the brackets on the right side $\sim PL/\left(bt^2\sigma_y\right)$, it suggests the following scaling ansatz

$$\frac{\delta}{\sigma_y L^2/(Et)} = F\left(\frac{P}{\sigma_y bt^2/L}\right), \tag{3.16}$$

where the unknown non-linear functionality F is yet to be determined. The nature of this unknown function must be such that it is linear up to the point of onset of plasticity.

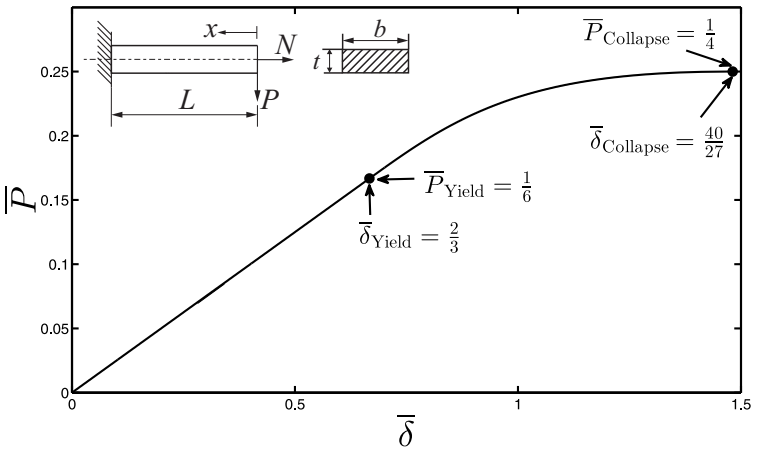

Figure 3.12: Plot of the non-dimensional force $\overline{P}$ against the transverse deflection $\overline{\delta}$ of a cantilever beam subjected to transverse tip loads P and N. With a suitable scaling of variables *all* the $\overline{P}$-$\overline{\delta}$ relationships collapse to a single master curve–thus providing us with the unknown functionality F. The point $(\overline{P}_{\text{Yield}}, \overline{\delta}_{\text{Yield}})$ corresponds to the onset of plasticity, whilst $(\overline{P}_{\text{Collapse}}, \overline{\delta}_{\text{Collapse}})$ to the collapse of the beam when the cross-section at the root is fully plastic.

Clearly, in linear elasticity, $\delta \sim P$ and $\delta \sim (bt^3)^{-1}$, the tip force for yielding scales according to $P_{\text{Yield}} \sim \sigma_y bt^2/L$, and the tip force for plastic collapse scales as $P_{\text{Collapse}} \sim \sigma_y bt^2/L$. So we could have alternatively sought a scaling ansatz of the form

$$\frac{(\delta/L)}{(\sigma_y/E)} = \left(\frac{t}{L}\right)^{\alpha} f\left(\frac{P}{\sigma_y bt^2/L}\right). \tag{3.17}$$

Since, the above has to be valid for the linear elastic part of the curve dimensional homogeneity results in $\alpha = -1$, whence we arrive at the sought scaling law (3.16).

Thus we renormalise the variables according to $\overline{\delta} = \delta/(\sigma_y L^2/Et)$ and $\overline{P} = P/(\sigma_y bt^2/L)$ so that we get a 'master-curve' describing the non-linear elasto-plastic behaviour of beams subjected to tip loads. This proposed master-curve now includes *all* geometric and material parameters relevant to the mechanics of such a cantilever beam and is presented in figure 3.12. All the curves for various geometric and material data collapse to this line. This functionality can be conveniently expressed via the inverse relationship of (3.8) as

$$\overline{P} = G(\overline{\delta}); \tag{3.18}$$

as it was convenient to treat the elastic response δ as the dependent variable whereas the force at the tip P as the independent variable to develop the relationship (3.16), but the curve in figure 3.12 and the stress-strain curve are frequently presented with the response variables (defection or strain, respectively) as the independent variable.

Consider salient points on the non-linear functional relationship between the applied force and the tip deflection. Smooth transition to plasticity is observed in the functional relationship $\overline{P}(\overline{\delta})$. We will denote this relationship via a generic function $G(x)$.

The non-linear part of the sought functionality $G(x)$ in equation (3.16) is analytically tractable and is implicitly available via the relationships such as equation (3.6) which could be specialised for zero axial force, as shown in figure 3.12. Two critical points on the curve (i) transition to plasticity when the first outer fibre of a cell wall yields and (ii) plastic collapse when a cross-section becomes wholly plastic can be analytically derived with relative ease. At the onset of yielding, one obtains

$$\overline{P}_{\text{Yield}} = \frac{1}{6}, \quad \text{and} \quad \overline{\delta}_{\text{Yield}} = \frac{2}{3} \tag{3.19}$$

as the non-dimensional force and the deflections at the onset of plasticity. The corresponding value for collapse are calculated for the completely plastic state of the cell wall cross-section as

$$\overline{P}_{\text{Collapse}} = \frac{1}{4}, \quad \text{and} \quad \overline{\delta}_{\text{Collapse}} = \frac{40}{27} \tag{3.20}$$

which highlights that the collapse force is 50% higher than the force at which yielding takes place. This value of the tip response of the cantilever beam is obtained from the analytical expression for beam elasto-plasticity discussed in Section 2 when the axial force is set to zero.

Following a successful scaling analysis of tip deflection in non-linear elasto-plastic deflection of a cell wall, we can infer the apparent elasto-plastic response of infinite lattices subject to remotely applied stress. The apparent strain of lattices scale as $\langle\epsilon\rangle \sim \delta/L$, the apparent stress scales as $\sigma_\infty \sim P/bL$. This suggests the functional relationship of the form $\langle\epsilon\rangle/\langle\epsilon\rangle_{\text{ref}} \propto F(\sigma_\infty/\sigma_{\infty_{\text{ref}}})$ where the reference values for the apparent strain and the remote stress need to be established. The proportionality constant would depend on the lattice geometry alone (i.e the length, angle etc. associated with cell walls, but

not thickness or material properties). For a lattice of characteristic cell wall length l, we have $l \sim L$. Therefore, the functional form of the remote stress vs apparent strain curve must be similar to that of the $\overline{P} - \overline{\delta}$ curve up to a yet to be determine scaling of the two stress and strain variables. This can be mathematically expressed as

$$\beta\overline{\sigma}_\infty = G\left(\alpha\langle\overline{\epsilon}\rangle\right) \tag{3.21}$$

where scale factors α and β are still to be determined. Here, the scaled remote stress $\overline{\sigma}_\infty$ and the scaled apparent strain $\langle\overline{\epsilon}\rangle$ are defined as

$$\overline{\sigma}_\infty = \frac{\sigma_\infty}{\sigma_y t^2/l^2}, \quad \text{and} \quad \langle\overline{\epsilon}\rangle = \frac{\langle\epsilon\rangle}{\sigma_y l/Et}, \tag{3.22}$$

respectively. Note the presence of the terms σ_y, t, l within the scaling parameters of *both* remote stress σ_∞ and the apparent strain $\langle\epsilon\rangle$ that are related non-linearly via the function G. With the help of the scaling suggested by equation (3.15) and hence equation (3.16), this has been possible. Note that scaling such as apparent modulus $\sim E(t/l)^3$, well known in linear elasticity of cellular solids, is unable to provide the scaling arrived at here. Further, for the linear part of G, terms cancel out in a way that the commonly used non-dimensionalisation of the apparent modulus reappears naturally.

Given the limits of the $\overline{P} - \overline{\delta}$ curve, we conclude that $0 \leq \alpha\langle\overline{\epsilon}\rangle \leq 40/27$ and $0 \leq \beta\overline{\sigma}_\infty \leq 1/4$. Similarity between the $\overline{P} - \overline{\delta}$ and the $\overline{\sigma}_\infty - \langle\overline{\epsilon}\rangle$ curves suggests that there must be correspondence between *physically corresponding* point on the two curves. One such point is that of onset of yielding, characterised on the $\overline{P} - \overline{\delta}$ curve by equation (3.11). Therefore, we must have

$$\alpha\langle\overline{\epsilon}\rangle_{\text{Yield}} = 2/3, \quad \text{and} \quad \beta\left(\overline{\sigma}_\infty\right)_{\text{Yield}} = 1/6. \tag{3.23}$$

We are now able to develop analytical functional relationship which would make used of the functionality of the master curve $G(x)$ for lattices. To illustrate this for the regular hexagonal lattices, consider the maximum bending moment in the cell walls due to remote stress σ_∞ as $M = 3\sigma_\infty bl^2/8$. Equating this to the fully plastic moment $\sigma_y bt^2/6$, we obtain $\left(\overline{\sigma}_\infty\right)_{\text{Yield}} = 4/9$. Substituting this into (3.23), we obtain $\beta = 3/8$. In the proportional range, the stress-strain relationship for regular hexagonal lattices is given by $\sigma_\infty = 4\langle E\rangle/\sqrt{3}$ which, upon non-dimensionalisation, results in

$$\frac{\left(\overline{\sigma}_\infty\right)_{\text{Yield}}}{\langle\overline{\epsilon}\rangle_{\text{Yield}}} = \frac{4}{\sqrt{3}}, \tag{3.24}$$

whence $\langle\overline{\epsilon}\rangle_{\text{Yield}} = 1/(3\sqrt{3})$. Substituting this into (3.23), we obtain $\alpha = 2\sqrt{3}$. Thus we have an analytical response relationship for the lattice in terms of the beam defection function $G(x)$ as

$$\frac{3}{8}\overline{\sigma}_\infty = G\left(2\sqrt{3}\langle\overline{\epsilon}\rangle\right). \tag{3.25}$$

This curve is found to be very close to that obtained numerically (not shown for brevity), the difference being mainly attributable to the neglect of stretch deformation in the analysis.

The approach presented here is general with the potential for application to the response calculation of more complex lattice architectures. One of the important implications of equation (3.21) is that one is able to calculate the complete non-linear response of a complex elastic lattice which is bending dominated by carrying out a linear analysis, provided one is able to analytically calculate another point (but not the whole curve) on the $\overline{\sigma}_\infty - \langle\overline{\epsilon}\rangle$ relationship. One such point is the onset of yield, as used above. Another possibility is that of the collapse point. The rest of the non-linear functionality is given by the function $G(x)$. In this manner, the argument developed in this section enables us to obtain analytical stress-strain curves for any lattice, in principle, as long as we are able to calculate certain identifiable points on the apparent stress-strain curve. Thus, we are able to separate the cell wall mechanics characterised via figure 3.12 from the kinematics of cell walls that depend on the lattice geometry. The two together afford the apparent stress-strain relationship such as the one above in equation (3.25).

Correspondence of points on the $\overline{P} - \overline{\delta}$ and the $\overline{\sigma}_\infty - \langle\overline{\epsilon}\rangle$ curves allows us to obtain other interesting pieces of information without extra effort. For example, equation (3.25) implies that the stress at collapse would given by $3(\overline{\sigma}_\infty)_{\text{Collapse}}/8 = 1/4$ and $2\sqrt{3}\langle\overline{\epsilon}\rangle_{\text{Collapse}} = 40/27$. The first of these for regular hexagonal lattices results in the well known formula for collapse [3] as $(\sigma_\infty)_{\text{Collapse}} = (2/3) \times \sigma_y t^2/l^2$, whereas the apparent strain at the point of collapse is given by

$$\langle\epsilon\rangle_{\text{Collapse}} = \left(\frac{20}{27\sqrt{3}}\right)\frac{\sigma_y l}{Et}, \tag{3.26}$$

a result not previously known. Note that the determination of the scale factors α or β did not make use of the collapse values on the $\overline{P} - \overline{\delta}$ curve. In spite of this, the corresponding values on the $\overline{\sigma}_\infty - \langle\overline{\epsilon}\rangle$ curve can now be predicted. Numerically obtained value of 0.41 for the coefficient within the parenthesis in equation (3.26) agrees very favourably with the theoretically predicted one of $20/27\sqrt{3}$. Of course, these analytical formulas are approximate up to ignoring shear, axial strain, geometric non-linearity etc. as stated earlier. Also the analytical knowledge that strain at collapse scales linearly with the yield stress and the lattice characteristic length whereas it is inversely proportional to the Young's modulus and the cell wall thickness are very useful pieces of design information.

3.3 Conclusions

Honeycomb lattices are analysed here for plastic response and recoil starting from transition to plasticity up to collapse. The simplification of the cell wall mechanics using a beam idealisation coupled with lattice kinematics enables us to obtain analytical results. The underlying material behaviour is assumed to be elastic-perfectly-plastic which leads to a smooth apparent stress-strain relationship for the lattice.

The main contributions of the present work within this chapter are summarised as follows. (a) A *benchmark analytical solution* for honeycomb plastic response was provided for the first time. Such problems have been studied computationally and experimentally before, but without any *analytical success*. (b) On the basis of the analytical framework developed in (a), we have obtained results, also analytically, for recoil of honeycombs post-plastic deformation. These calculations are not only theoretically significant, they are critical in many applications such as the assessment of recoil in stents. (c) The present work provides a framework to obtain *design sensitivities* analytically for a complex non-linear response. This are present in the dimensional groups used for the renormalisation of the apparent strain and the remote stress. (d) Scaling transformations that are non-trivial as they require physical arguments in addition to dimensional homogeneity, were developed successfully. This affords a '*non-linear master deformation profile*' –thus collapsing data for all the combinations of lattice and material parameters. (e) A separation of the non-linear mechanics of the cell wall and the lattice kinematics is achieved. This, together with the scaling transformations, enables response curves to be transformed to a single curve for various parametric changes. (f) The 'master curve' was fully characterised for critical points such as those at transition to plasticity, collapse, relevant slope and shape, via non-dimensional numbers and non-dimensional functions describing shapes. (g) Using a kinematic argument, we show that the apparent Poisson's ratio of the honeycomb during the plastic phase of deformation remains the same as that during the elastic phase. (h) The response of auxetic lattices under plastic deformation is presented for the first time.

In summary, here we provide a benchmark analytical solution in the area of non-linear plastic response of hexagonal honeycombs with potential applications to a range of problems in applied mechanics, engineering and design. These could span applications from biomedical devices to crash and impact studies.

Chapter 4

Elasto-plastic response and recoil of lattices with circular cross-section and under hyperbolic hardening

Periodic structures are made of a unit cell that is translationally repeated in space. By making use of this periodicity, the apparent response of an infinite honeycomb sheet, during loading and unloading, was analytically calculated in the previous chapter. The analysis was based on the response of one inclined cell wall, which was modelled as a thin beam of rectangular cross-section simultaneously under bending and stretch. The material model for the honeycomb considered in Chapter 3 was elastic-perfectly-plastic. Because of the idealised constituent material, the non-linear effects due to the material hardening and the effects of cross-section shape were not taken into consideration, since only the rectangular case was analysed.

Recently, additive manufacturing (AM) has become a promising alternative for the fabrication of this class of materials because it gives the opportunity of the controlled deposition of matter in the 3D-space. There is a current drive to print such honeycomb films and lattices for biomedical applications. 3D printed honeycombs with bespoke tool path planning are printed in a manner that the nozzle traverses the lattice along the cell wall direction. In this manner, filaments that can be mechanically modelled as beams of *circular* cross-section are deposited to form the honeycomb lattice (see figure 4.1). This shows the need of an elasto-plastic model for thin circular beams under complex loading first, from which the response of the 3D-printed lattice material can be later inferred. To obtain more realistic results, the effects of the non-linear hardening of the constituent material must be included. This will be possible by introducing a novel hyperbolic model to describe the non-linear post-yielding behaviour of the bulk material.

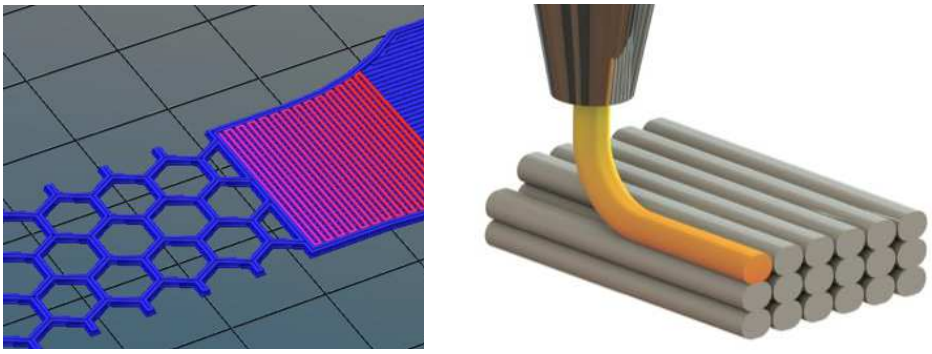

(a) (b)

Figure 4.1: (a) 3D printed honeycombs with the nozzle moving along the cell walls [124]. (b) This gives rise to cell walls of circular cross-section [125].

The purpose of this chapter is to present an extensive study on the mechanics of a beam with a circular cross-section subjected to elasto-plastic bending and axial force which is currently missing in the literature. The analysis also includes the springback upon unloading. The final aim is to provide an accurate theoretical model that can be used for the calculation of the elasto-plastic response of lattice materials. Two different types of material behaviours are considered: (a) elastic-perfectly-plastic, (b) elasto-plastic with hyperbolic hardening–a novel model that will be developed in this chapter. Finally, a new analytical model to calculate the transverse deflection of a beam with rectangular cross-section, which takes into consideration the non-linear effects due to the material hardening and the stiffening effects due to the application of an axial load is developed. This aims to make the results presented in the previous chapter more realistic. The model can be also extended to the area of metal forming processes, as it will be briefly shown in the last section of this chapter.

4.1 Plastic analysis and springback of beams under combined axial and bending loading

An initially straight beam of circular cross-section of radius r is loaded by a constant bending moment M and a tensile force N, as shown in figure 4.2. Small deformations are assumed here so that the deflection of the beam is small compared to the cross-sectional dimensions. Also, it is assumed that the cross-sections of the beam remain plane during the elasto-plastic deformation (Bernoulli's hypothesis). As a result, strain is linearly related to the distance from the neutral axis. The beam is also assumed stress-free before loading.

When a bending moment is applied to a beam (as shown in figure 4.2), the top fibres are extended–thus subjected to tensile stress, whilst the lower compressed. The bending stress varies smoothly between the maximum positive stress (tensile) and negative

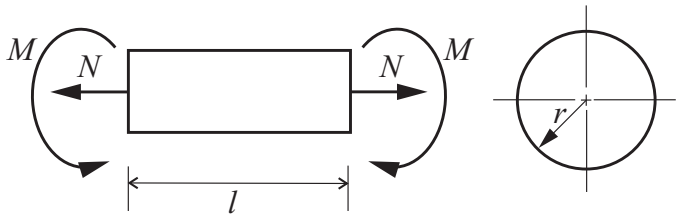

Figure 4.2: Initial straight beam of circular cross-section loaded with axial force N and bending moment M.

(compression). The neutral axis is the location where the stress is zero–thus there are no strains. For symmetric, isotropic and straight beams, the neutral axis is at the geometric centroid of the cross-section. However, its location changes if an axial load is applied. Due to this shift, the two parts of the sections do not experience a symmetric state of stress. For different combinations of M and N, the stress distribution over a cross-section can be one of the three types (see figure 4.3):

1. Wholly elastic stress distribution: no fibre parallel to the longitudinal axis of the beam undergoes plastic deformation;
2. Primary plastic stress distribution, *PI*: only part of one side of the beam, either above or below the neutral axis, is plastically deformed;
3. Secondary plastic stress distribution, *PII*: the cross-section is partially plastically deformed above and below the neutral axis. However, the extent of the two plastic zones is asymmetric due to the presence of axial load.

An ideal elastic-perfectly-plastic material model is considered first. The study is then extended for an elasto-plastic material model with non-linear hardening. The following dimensionless variables for axial force N, moment M and curvature κ of the section are now defined as

$$n = |N|/(\sigma_y r^2), \quad m = |M|/(\sigma_y r^3) \quad \text{and} \quad \phi = |\kappa|/\kappa_e, \tag{4.1}$$

where σ_y is the yield stress, r is the radius of the cross-section and κ_e is the initial yield quantity for the curvature under pure bending, given by

$$\kappa_e = \sigma_y/(rE), \tag{4.2}$$

where E is the Young's modulus of the constituent material.

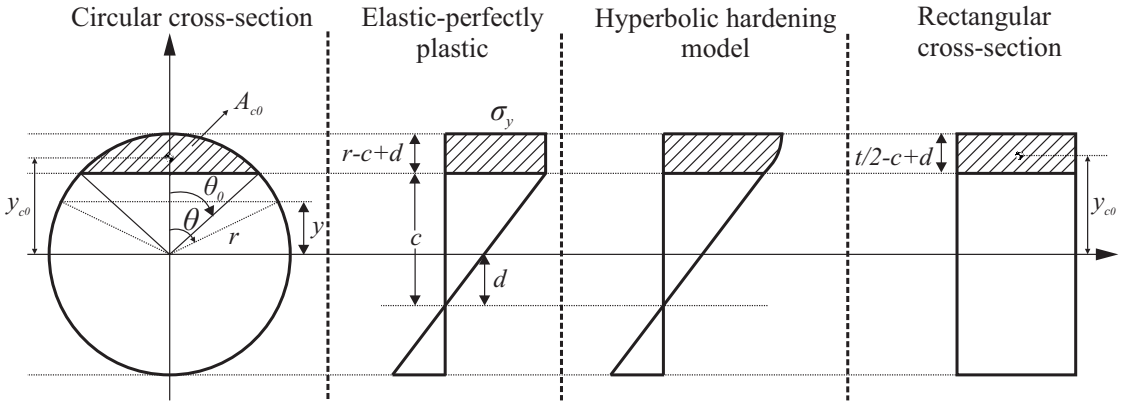

(a) Primary plastic regime PI

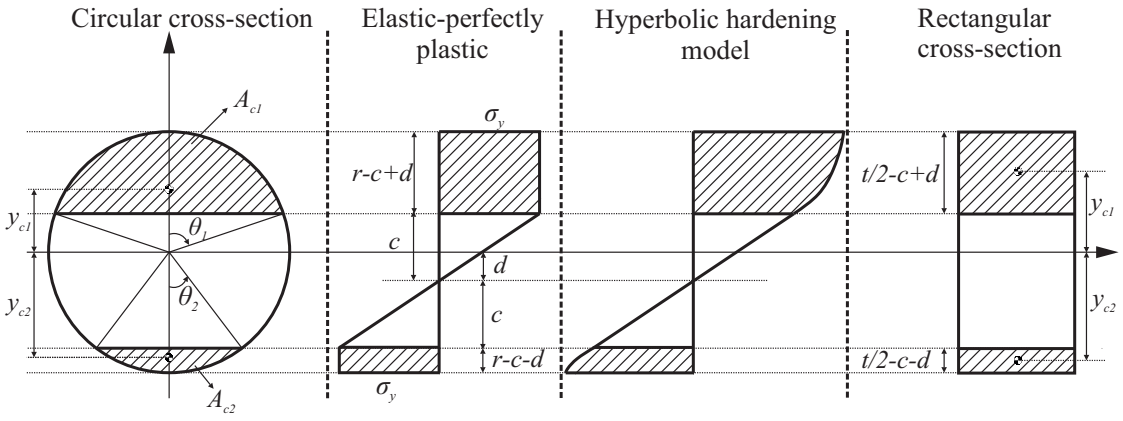

(b) Secondary plastic regime PII

Figure 4.3: (a) Stress distribution across the circular and rectangular cross-section: PI regime. The circular segment area is denoted by A_{c0} and the location of its centroid by y_{c0}.(b) Stress distribution across the circular and rectangular cross-section: PII regime. The circular segment areas are denoted by A_{ci} and the location of its centroid by y_{ci}. The first stress profiles are those obtained for the elastic-perfectly-plastic case and the second ones these for hyperbolic hardening.

4.1.1 Elastic-perfectly-plastic material behaviour

Consider isotropic and homogeneous material that exhibits elastic-perfectly-plastic behaviour so that the stress-strain relationship can be expressed as

$$\sigma = \begin{cases} E\epsilon & \sigma < \sigma_y \\ \sigma_y & \sigma \geq \sigma_y \end{cases}. \tag{4.3}$$

For a combination of M and N, the stress distribution over each cross-section can be qualitatively classified in one of the three categories listed before. By setting up the equations for force and moment equilibrium for each category, the load-curvature relationship is derived in the following analysis.

Elastic-perfectly-plastic material: the elastic regime E_r

In this regime, the deformation is purely elastic; therefore, the final stress distribution is obtained by superposing the effects of separately applied axial force and bending moment. Note that under this loading state the longitudinal axis of the beam and the neutral axis do not coincide, in contrast to the pure bending case usually studied.

Using the superposition principle, it can be shown that the load-curvature relationship in the elastic regime is

$$\phi = m \tag{4.4}$$

for $m + n \leq 1$ [67]. Hence, the boundary of the onset of plasticity for this regime is $m + n = 1$, beyond which the treatment must account for plasticity.

Elastic-perfectly-plastic material: the primary plastic regime PI

Due to the asymmetric stress distribution relative to the centroid, upon simultaneous application of N and M, one side of the beam undergoes plastic deformation as loading is increased. This is shown in figure 4.3 (a). The non-linearity of the problem introduced by yielding now prohibits the use of the superposition principle. Therefore, the load-curvature relationship can only be calculated by imposing the force and moment static equilibrium conditions at the cross-section.

The cross-section is assumed to be circular having radius r in which a circular segment of area A_{c0} has undergone plastic deformation. The second figure within 4.3 (a) refers to the stress profile for PI regime when elastic-perfectly-plastic stress-strain relationship is used. Let θ_0 be half of the central angle of the circular segment in radians and y_{c0} the position of its centroid with respect to the centre of the circle. The position along the circumference is described using the angle θ, measured from the vertical axis. It turns out that parametrising the plastic zone in the polar co-ordinates using θ_0 facilitates calculations greatly.

Static equilibrium of the axial force over the cross-section leads to

$$\left(\theta_0 - \frac{1}{2}\sin 2\theta_0\right) - \frac{2}{c}\left[\frac{r}{3}\sin^3\theta_0 + \frac{d}{2}\left(\theta_0 - \frac{1}{2}\sin 2\theta_0\right) - \pi\frac{d}{2}\right] = n, \tag{4.5}$$

where d is the shift of the neutral axis from the centre of the section and c is the distance of the first yielded fibre from the neutral axis (figure 4.3 a). Equilibrium of the bending moment due to stress distribution over the cross-section results in

$$\frac{2}{3}\sin^3\theta_0 - \frac{2}{c}\left[\frac{d}{3}\sin^3\theta_0 + \frac{r}{8}\left(\theta_0 - \frac{1}{4}\sin 4\theta_0\right) - \pi\frac{r}{8}\right] = m. \tag{4.6}$$

A detailed derivation of this can be found in the Appendix A. Substituting from

$$(c - d)/r = \cos\theta_0 \tag{4.7}$$

for d into equations (4.5) and (4.6), we obtain a pair of simultaneous equations

$$\begin{aligned} \cos\theta_0\left(\pi-\theta_0+\tfrac{1}{2}\sin 2\theta_0\right)+\tfrac{2}{3}\sin^3\theta_0 &= (\pi-n)\,\tfrac{c}{r} \\ \tfrac{1}{4}\left(\pi-\theta_0+\tfrac{1}{4}\sin 4\theta_0\right)+\tfrac{2}{3}\cos\theta_0\sin^3\theta_0 &= m\tfrac{c}{r} \end{aligned} \tag{4.8}$$

in variables θ_0 and c/r. The unknown c/r can be eliminated leading to a single equation in terms of θ_0 only. Substituting this into one of the equation in (4.8), we determine the value of c. Once the value of c is known, then the dimensionless curvature ϕ can be calculated from

$$\phi = r/c. \tag{4.9}$$

Elastic-perfectly-plastic material: the secondary plastic regime PII

When the axial force and bending moment, N and M respectively, are further increased, both sides of the beam undergo plastic deformation, as shown in figure 4.3 (b). As for the case of primary plastic regime, the load-curvature relationship is found by imposing the static equilibrium since the non-linearity due to plasticity forbids the application of the superposition principle.

When plastic deformation develops on both sides of the longitudinal axis, the two yielded segments have a different area, A_{c1} and A_{c2} above and below the neutral axis respectively, because of the asymmetric distribution with respect to the centre of the section. The locations of the centroids of the plastic regions are, respectively, y_{c1} and y_{c2} and the central angles of the two plastic regions are θ_1 and θ_2, as shown in figure 4.3 (b). The central figure within 4.3 (b) refers to the stress profile for PII regime when the elastic-perfectly-plastic stress-strain relationship is used.

The axial force equilibrium now requires summing contributions from the two outer plastic regions and the elastic core. The result is expressed as

$$\begin{aligned} \left(\theta_1-\frac{1}{2}\sin 2\theta_1\right)-\left(\theta_2-\frac{1}{2}\sin 2\theta_2\right)-\frac{4}{3}\frac{\sin^3\theta_1-\sin^3\theta_2}{\cos\theta_1+\cos\theta_2}+\frac{\cos\theta_1-\cos\theta_2}{\cos\theta_1+\cos\theta_2}\left(\pi-\theta_1-\theta_2\right)+ \\ +\frac{1}{2}\sin 2\theta_1+\frac{1}{2}\sin 2\theta_2 = n. \end{aligned} \tag{4.10}$$

Similarly, the moment equilibrium now requires integrating contributions over the cross-section leading to

$$\begin{aligned} &\frac{2}{3}\left(\sin^3\theta_1+\sin^3\theta_2\right)-\frac{2}{3}\frac{\cos\theta_1-\cos\theta_2}{\cos\theta_1+\cos\theta_2}\left(\sin^3\theta_1-\sin^3\theta_2\right)+ \\ &+\frac{1}{8}\frac{1}{\cos\theta_1+\cos\theta_2}\left[-4\left(\theta_1+\theta_2-\pi\right)+\sin 4\theta_1+\sin 4\theta_2\right] = m. \end{aligned} \tag{4.11}$$

A detailed derivation of (4.10) and (4.11) is presented in the Appendix A. Equations (4.10) and (4.11) constitute a non-linear system of trigonometric equations that cannot

be reduced further. From the values of θ_1 and θ_2 obtained, the distance c of the fibre first yielded from the neutral axis is obtained as

$$c = r/\left[2(\cos\theta_1 + \cos\theta_2)\right], \tag{4.12}$$

from which the curvature is derived using equation (4.9).

4.1.2 Hyperbolic hardening model

Engineering design requires realistic constitutive models that relate stress and strain within materials. Mathematical description of constitutive behaviour frequently requires a compromise between realism and simplicity of the model for the given purpose. Material plasticity is an important non-linear response of engineering materials. At microscopic level, for polycrystalline material, crystal planes slip in the direction of the largest shear stress. This slip is possible because of the motion of dislocations of atom planes. For polymers, the origin of material non-linearity lies in the physics of the polymer chains and their response to mechanical stimulus. The two commonly used mathematical descriptions employed to model the macroscopic hardening behaviour of materials are Hollomon's equation and Ludwik's equation [74]. Since these power law expressions introduce mathematical difficulties in the plastic beam bending analysis and also lack a linear elastic regime, a new mathematical representation of the stress-strain curve is sought here. A very wide range of engineering materials show a linear response for low strain followed by a plastic region of hardening where the tangent modulus of the material monotonically reduces upon increased strain. Inspired by the constitutive law used for soil and polystyrene geofoam [126], a linear model followed by an hyperbolic stress-strain relationship is proposed here (figure 4.4). The stress-strain behaviour of several materials can be separated into the linear elastic behaviour and the non-linear behaviour due to plasticity. The linear behaviour is observed until the yield point is reached and it is modelled using a straight line which passes through the origin and of which the slope is the Young's modulus. The plastic behaviour is described here by a rectangular hyperbola with asymptotes translated with respect to the reference system. Here we propose a constitutive relationship of the form

$$\sigma = \begin{cases} E\epsilon & \sigma < \sigma_y \\ \dfrac{B\epsilon + D}{A - \epsilon} & \sigma \geq \sigma_y \end{cases}, \tag{4.13}$$

where A, B and D are the coefficients of the hyperbola and $\sigma_B = -B$ and $\epsilon = A$ are the asymptotes. The parameters are calculated by imposing the continuity and differentiability at the interface of the elastic and the plastic regimes.

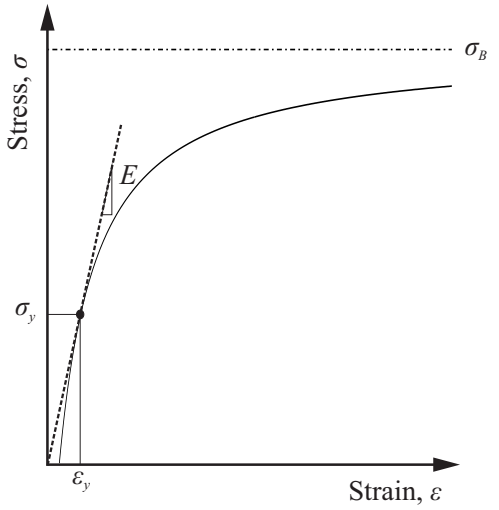

Figure 4.4: Proposed stress-strain relationship with hyperbolic hardening

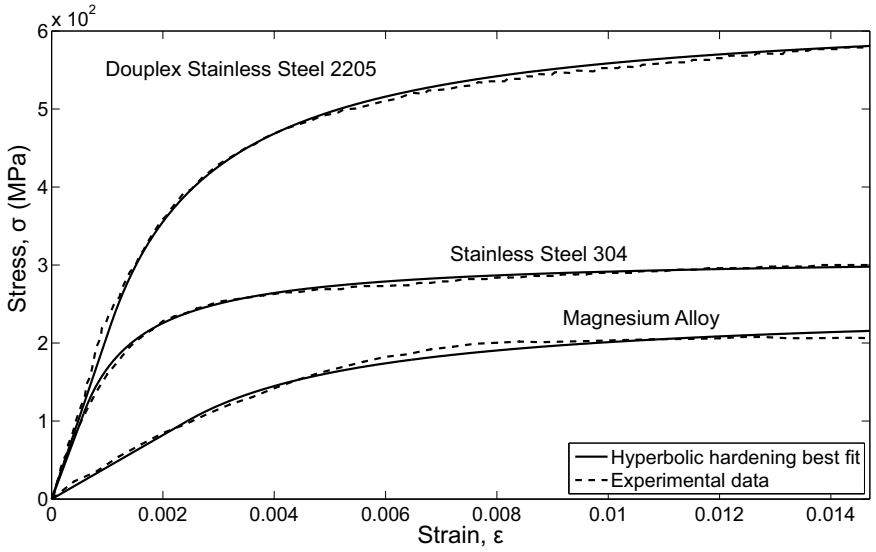

Figure 4.5: Hyperbolic interpolation for Douplex stainless steel 2205, Stainless steel 304 and Magnesium alloy (Original data from [127; 128]).

The first requirement of continuity at the yield point is expressed as

$$\sigma(\epsilon = \epsilon_y) = \sigma_y. \tag{4.14}$$

The gradient continuity between the hyperbola and the straight line at the yield point provides a second condition

$$\left.\frac{\mathrm{d}\sigma}{\mathrm{d}\epsilon}\right|_{\epsilon=\epsilon_y} = E. \tag{4.15}$$

The material parameters most readily available from the experiments are the Young's modulus E, yield stress σ_y, yield strain ϵ_y and the parameter B which is the σ asymptote.

To test how realistic the proposed hyperbolic hardening model is, here we compare the best fit to experimentally obtained data ([127; 128]). For this, the difference between the data and the model was treated as error to facilitate curve fitting. The sum of square of the error was minimised by the use of a Genetic Algorithm (GA). The process of curve-fitting was thus treated as an error minimisation problem by a GA. The $\sigma - \epsilon$ relationship (4.13) was fit to previously published data for three different real materials (figure 4.5). The hyperbola parameters estimated for the set of trial materials shown in the figure are summarized in Table 4.1.

Material	A (10^{-4})	B (MPa)	D (MPa)
Douplex Stainless Steel 2205	-8.98	-6.32×10^{2}	2.34×10^{-1}
Stainless Steel 304	-4.84	-3.12×10^{2}	6.37×10^{-2}
Magnesium Alloy	-0.122	-2.50×10^{2}	2.44×10^{-1}
Elastic-perfectly plastic	-0.111	-2.20×10^{2}	2.32×10^{-2}

Table 4.1: Hyperbola coefficients obtained from the genetic algorithm for the real materials shown in figure 4.5 and the ideal elastic-perfectly-plastic material.

The experimental data and the hyperbolic hardening model are found to be in good agreement. Note that a somewhat similar representation has been recently used for cast iron ([129]). There, the hyperbolic model has been used to describe the whole constitutive material law because the cast iron shows non-linearities also at low stresses. Unlike the model proposed by Rajani [129], the one proposed here has a linear part which simulates the behaviour of many real material more faithfully.

4.1.2.1 Beam with circular cross-section

Filaments of circular cross-section used for 3D printing of lattices can be modelled as beams. The analysis for the elastic-perfectly-plastic material in the three regimes of plasticity (on the lines of Section 4.1.1) is now carried out for the hyperbolic hardening model. An initially straight beam with circular cross-section made of an isotropic and homogeneous material that exhibits non-linear hardening is considered here.

Hyperbolic hardening: the elastic regime E_r

The stress distribution over the cross-section remains the same as that previously discussed in Section 4.1.1 for the elastic-perfectly-plastic case. Therefore, all the relationships developed there stay unchanged.

Hyperbolic hardening: the primary plastic regime PI

When a cross-section starts yielding under combined axial loading and flexure, the plastic deformation takes place only on one side of the beam as for the elastic-perfectly-plastic material. The presence of the axial force shifts the neutral axis away from the centroid, causing an asymmetric stress distribution whose qualitative behaviour is illustrated in

figure 4.3 (a). The stress profile for hyperbolic hardening is shown in the third figure from left to right within 4.3 (a). Whilst for the elastic-perfectly-plastic material model the maximum stress remains constant, once the yield stress σ_y is reached, for the hyperbolic hardening material, the post-yielding stress distribution is non-linear and requires a new analysis.

Johnson and Mellor [61] presented the stress distribution over each cross-section by re-drawing the material stress-strain diagram from the neutral line. Therefore, the shape of the non-linear stress profile over the cross-section is known. By using this argument, the axial force equilibrium yields

$$\frac{1}{\sigma_y}\int_0^{\theta_0} 2\sigma(\theta)\sin^2\theta \mathrm{d}\theta - \frac{2}{c}\int_{\pi}^{\theta_0}(r\cos\theta + d)\sin^2\theta \mathrm{d}\theta = n, \tag{4.16}$$

and similarly the moment equilibrium results in

$$\frac{1}{\sigma_y}\int_0^{\theta_0} \sigma(\theta)2\sin^2\theta\cos\theta \mathrm{d}\theta - \frac{2}{c}\int_{\pi}^{\theta_0}(r\cos\theta + d)\sin^2\theta\cos\theta \mathrm{d}\theta = m \tag{4.17}$$

where

$$\sigma(\theta) = \frac{B(\epsilon_y/c)(r\cos\theta + d) + D}{A - (\epsilon_y/c)(r\cos\theta + d)}. \tag{4.18}$$

The first integral in equation (4.16) and (4.17) is the contribution of the stress over the circular segment having undergone plastic deformation, whilst the second integral is that corresponding to the area where the deformation is still elastic. A detailed derivation of $\sigma(\theta)$ is presented in the Appendix A. The three unknowns c, d and θ_0 are related by equation (4.7). By substituting one variable from equation (4.7) into (4.16) and (4.17), a system of two equations in two unknowns is obtained. The nondimensional curvature is finally calculated using equation (4.9). The curvature relation can then be integrated to determine the transverse deflection.

Hyperbolic hardening: the secondary plastic regime PII

Increasing N and M further leads to plastic deformation on both sides of the beam as shown in figure 4.3 (b). The corresponding stress profile for the hyperbolic hardening model is shown in the third from left to right figure of 4.3 (b) In a manner similar to that applied for the PI case, the stress profile after yielding shows a non-linear behaviour. In the current model, the hyperbolic function introduced here is used to describe the post-yield stress distribution.

The equilibrium along the axial direction can be expressed as

$$\int_0^{\theta_1} \sigma(\theta)2\sin^2\theta \mathrm{d}\theta + \int_0^{\theta_2} -\sigma(\theta)2\sin^2\theta \mathrm{d}\theta - \frac{2}{c}\int_{\pi-\theta_2}^{\theta_1}(r\cos\theta + d)\sin^2\theta \mathrm{d}\theta = n, \tag{4.19}$$

which is obtained by summing the contributions of fibres under tension and compression over the circular cross-section. Similarly, moment equilibrium leads to

$$\int_0^{\theta_1} \sigma(\theta) 2\sin^2\theta\cos\theta \mathrm{d}\theta + \int_0^{\theta_2} -\sigma(\theta) 2\sin^2\theta\cos\theta \mathrm{d}\theta - \frac{2}{c}\int_{\pi-\theta_2}^{\theta_1} (r\cos\theta + d)\sin^2\theta\cos\theta \mathrm{d}\theta = m, \tag{4.20}$$

where the moment over the cross-section is calculated via the sum of the integrals above. The first two integrals are the stress contributions from the upper and lower circular segment undergone plastic deformation, whilst the last integral is attributed to the area under elastic deformation. A non-linear system of two equations, (4.19) and (4.20), involving four unknowns c, d, θ_1, θ_2 is obtained. Two further conditions that relate these four unknowns are given by $\cos\theta_1 = (c-d)/r$ and $\cos\theta_2 = (c+d)/r$. Finally we have a pair of non-linear trigonometric equations in terms of two unknowns which can be solved.

4.1.2.2 Beam with rectangular cross-section

The analysis of plastically deformed structures is an old branch of mechanics. The problem of plastic deformation of rods of rectangular cross-section under combined axial-bending loading was solved analytically by Yu and Johnson [67] while assuming an elastic-perfectly-plastic constituent material. For completeness, we extend their study by developing a new model that takes into consideration the hyperbolic material hardening proposed here. Consider a beam with rectangular cross-section of width b and thickness t which is subjected to a pure bending moment M and an axial force N, as shown in figure 4.6. The beam is made of an elasto-plastic material with non-linear hardening. The plastic behaviour of the bulk material is described by the translated rectangular hyperbola. The constitutive relation is given by equation (4.13). The cross-section stress distribution is obtained by redrawing the stress-strain curve of the constituent material from the neutral axis [61]. The stress distribution is qualitatively similar to the one plotted for the circular cross-section in figure 4.3. The dimensionless parameters for moment, axial force and curvature are now given by

$$m = |M|/M_e, \quad n = |N|/N_e, \quad \phi = |\kappa|/\kappa_e. \tag{4.21}$$

Note that $M_e = \frac{1}{6}\sigma_y b t^2$, $N_e = \sigma_y b t$, $\kappa_e = 2\frac{\sigma_y}{tE}$ are respectively the initial yield quantities for moment, axial force and curvature.

Hyperbolic hardening: the elastic regime E_r

For the elastic regime E_r, the superposition principle can be used and the stress distribution over the cross-section remains the same as discussed for the circular cross-section. Since the analysis has been carried out using non-dimensional analysis, the change in

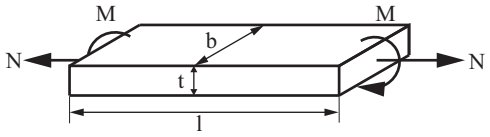

Figure 4.6: Straight beam with rectangular cross-section, subjected to pure bending moment and tensile axial force.

cross-sectional shape does not invalidate the previous results and all the relationships developed before stay unchanged.

Hyperbolic hardening: the primary plastic regime PI

The analysis for the rectangular cross-section while using hyperbolic hardening closely resembles that for the circular cross-section. The stress distribution through the thickness in the primary plastic regime is shown in figure 4.3 (a), the second stress distribution drawing. The axial force and moment equilibria equations are imposed to determine the values of the two unknowns, c and d. By requiring the axial equilibrium, the relation

$$n = \left[(\sigma_y c)/2 - \sigma_y \left(t/2 - d\right)^2 /(2c) + \int_c^{t/2+d} \frac{B\left(z\epsilon_y/c\right) + D}{A - \left(z\epsilon_y/c\right)} dz \right] \frac{b}{N_e} \tag{4.22}$$

is obtained. The first two terms are the contributions given by the two triangular areas under linear deformation, while the integral represents the total axial force given by the area under plastic deformation. Similarly, the moment equilibrium over the cross-section is imposed,

$$\begin{aligned} m = \Bigg[\sigma_y c \left(2c/3 - d\right)/2 - \sigma_y \left(t/2 - d\right)^2 /(2c) \left[\frac{t}{2} - \frac{1}{3}\left(\frac{t}{2} - d\right) \right] \\ + \int_c^{t/2+d} \frac{B\left(z\epsilon_y/c\right) + D}{A - \left(z\epsilon_y/c\right)} z dz \Bigg] \frac{b}{M_e}. \end{aligned} \tag{4.23}$$

By solving the non-linear system given by equations (4.22) and (4.23), the values of c and d shown in figure 4.3 (a) are obtained. Once the value of c is known, then the dimensionless curvature ϕ can be calculated from

$$\phi = (t/2)/c. \tag{4.24}$$

It can be shown that the beam will start yielding on both sides when $c + d = t/2$. This condition represents the boundary between the primary plastic regime and secondary plastic regime.

Hyperbolic hardening: the secondary plastic regime PII

If we further increase the loading, both sides of the beam undergo plastic deformation. The corresponding stress profile is qualitatively shown in figure 4.3 (b), the third figure

from the left. The force and momentum equilibria are imposed to determine the geometric parameters needed to describe the stress profile, as done in the previous section for *PI*. Such calculations are carried out by knowing that the non-linear stress distribution is described by the hyperbola function. By summing the contribution given by the two plastically deformed part of the cross-sections, the axial equilibrium results in

$$n = \frac{b}{Ne}\left(\int_c^{t/2+d} \frac{B\left(z\epsilon_y/c\right)+D}{A-\left(z\epsilon_y/c\right)}dz - \int_c^{t/2-d} \frac{B\left(z\epsilon_y/c\right)+D}{A-\left(z\epsilon_y/c\right)}dz\right). \tag{4.25}$$

Note that the contributions given by the two areas under elastic deformation are equal and opposite in sign. Therefore, the effects compensate and they do not generate any curve in the above equation. Similarly, the moment equilibrium given by the upper and lower part of the cross-section under plastic deformation leads to

$$m = \frac{b}{Me}\left(\int_c^{t/2+d} \frac{B\left(z\epsilon_y/c\right)+D}{A-\left(z\epsilon_y/c\right)}zdz + \int_c^{t/2-d} \frac{B\left(z\epsilon_y/c\right)+D}{A-\left(z\epsilon_y/c\right)}zdz\right). \tag{4.26}$$

As before, the system of equations (4.25) and (4.26) is solved for the unknowns c and d. By applying equation (4.24), the dimensionless curvature is obtained.

4.1.3 Springback of a beam following simultaneous application of bending moment and axial force

We will first present the results for the springback of a single beam followed by that for lattices in the next session. When the applied moment M and axial force N are removed, the elastic deformation is recovered but the plastic deformation remains permanently within the material. If the unloading is assumed to be linearly elastic, the final residual non-dimensional curvature is given by

$$\phi^F = \phi - m. \tag{4.27}$$

For all combinations of bending moment and axial force, the expression above provides the springback.

The numerical results for the elastic-perfectly-plastic material and a material showing hyperbolic hardening, whose horizontal asymptote σ_B corresponds to the yield stress of the elastic-perfectly-plastic material, are plotted in figure 4.7. Since these figures are in a non-dimensional form, they may be used for beams of any dimensions and hence to micro-filaments or macroscopic beam structures under elasto-plastic deformation. The shaded regions show the combination of normalised axial force and bending moment that lead to primary plastic state of stress. Figure 4.7 (a) relates to elastic-perfectly plastic case whereas 4.7 (b) to hyperbolic hardening for a beam with a circular cross-section. For the same combination of m and n, the final curvature ϕ_F is lower for

the material showing non-linear hardening. When an elastic-perfectly-plastic material undergoes plastic deformation, the hardening rate (measured by the tangent modulus) is equal to zero. Thus, the plastically deformed material no longer resists if any additional strain is applied. By contrast, to further deform a material showing a hardening rate different from zero, an increasing stress is required. Figure 4.7 (c) relates to the final curvature of a beam with rectangular cross-section made of a material showing hyperbolic hardening–with the same area of the circular cross-section. If the same axial force n and bending moment m are applied to the beam, the rectangular cross-section shows a lower springback and, therefore, a higher final curvature. As measured by the shape factor η, that is the ratio of the collapse moment and the plastic moment, the circular cross-section ($\eta = 1.70$) can store more energy than the rectangular cross-section ($\eta = 1.50$).

4.2 Elasto-plastic analysis of lattice structures

The analysis developed above can be now applied to many engineering problems. Here we now focus on a remarkable practical case: the model of periodic lattice structures under plastic deformation. Consider an honeycomb sheet loaded uniaxially along the $x-$ or $y-$direction, as presented in Chapter 3. The study of the overall structure response subjected to elasto-plastic deformation, due to symmetry can be reduced to the study of a single inclined cell wall, as explained in detail in the previous chapter. Each point along the strut experiences a different state of stress. Some cross-sections may be fully elastic, while others may be partially plastic. Plastic zones spread along the struts, lengthwise as well as thickness wise, when the remote stress is increased. The plastic zone is depicted by the hatched area in figure 3.3 and it shows asymmetric distribution due to the presence of the axial force. Note that tensile or compressive N results in the same final curvature because both tend to the same departure in stress distribution from the elastic case, but on the opposite sides of the centre line. The extent of plasticity on the top fibre is given by $0 \leq \xi \leq \xi_1$ and that for the bottom fibre by $0 \leq \xi \leq \xi_2$, where ξ is the non-dimensional co-ordinate along the beam. PI regime spans $\xi_1 \leq \xi \leq \xi_2$ and PII regime spans $0 \leq \xi \leq \xi_1$. Finally, $\xi_2 \leq \xi \leq l$ corresponds to the elastic part of the structure.

Consider first a cantilever beam with inclined tip load which has axial as well as transverse components. Two cases of the material behaviour are considered: that of elastic-perfectly-plastic and the one with hyperbolic hardening. To simplify the analysis, the maximum bending moment at the root of the beam is expressed in the non-dimensional form $m^* = Pl/(\sigma_y r^3)$ for a beam with a circular cross-section, and $m^* = Pl/M_e$ for a beam with a rectangular cross-section, where P is the transverse load. Introduce the non-dimensional co-ordinate ξ along the beam and the non-dimensional transverse deflection η as $\xi = x/l$ and $\eta = w(x)rE/(l^2\sigma_y)$ for a circular cross-section and $\eta = w(x)tE/(2l^2\sigma_y)$ for a rectangular cross-section, where $w(x)$ is the beam deflection and l the length of

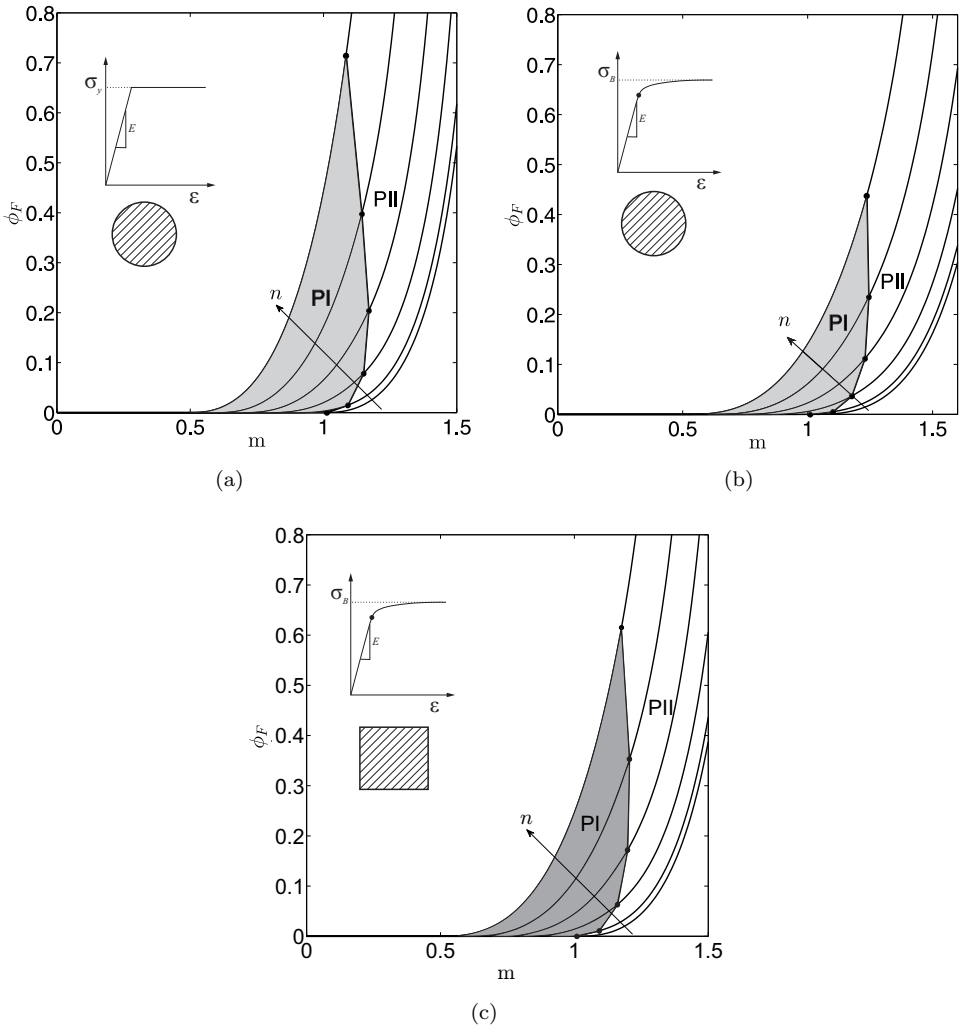

Figure 4.7: Non-dimensional curvature after the unloading for different combinations of m and n. The non-dimensional axial force, n, is 0.0, 0.1, 0.2, 0.3, 0.4 and 0.5, respectively from the right to the left lines. The primary plastic region and the secondary plastic region are demarcated by the dark solid lines. (a) Elastic-perfectly-plastic material ($E = 209$ GPa, $\sigma_y = 240$ MPa) with circular cross-section(b) Hyperbolic hardening material with circular cross-section ($E = 209$ GPa, $\sigma_B = 240$ MPa), yielding for this occurs at 200 MPa shown by a dot and (c) Hyperbolic hardening with rectangular cross-section, using the same material parameters.

the beam. The non-dimensional curvature is now given by

$$\frac{\mathrm{d}^2\eta}{\mathrm{d}\xi^2} = \phi. \tag{4.28}$$

The complete beam deflection is obtained by integrating the curvature expressions derived in the previous sections, and applying the geometric boundary conditions at the fixed end, thus $\eta = 0$ and $\mathrm{d}w/\mathrm{d}x|_{x=0} = 0$. The final deflected shape of the cantilever

beam after the unloading is found by subtracting the elastic deflection from the expression of η, leading to $\eta_F = \eta - m^*(1-\xi)$. The integration was performed by using the left-sided difference scheme for second order derivatives.

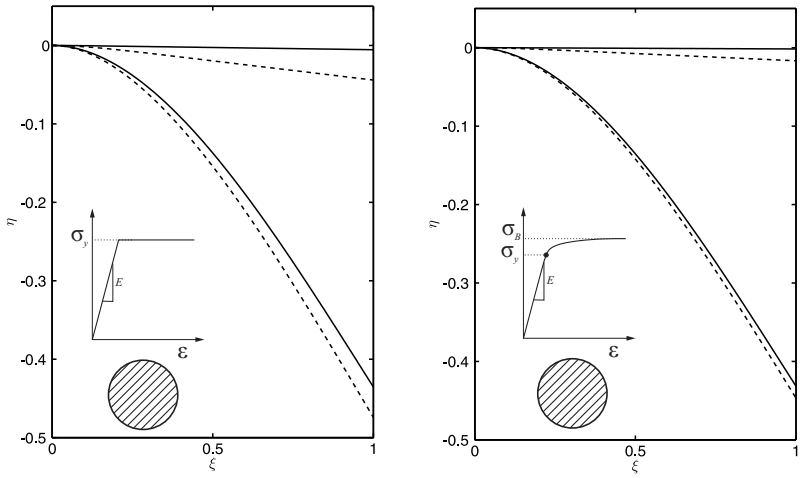

Figure 4.8: Deflection of the cantilever beam with circular cross-section. The results are presented for both elastic-perfectly-plastic material and elasto-plastic material with hyperbolic hardening. Different combinations of n and m^* are examined to study the influence of the axial force on the deformed shape: the solid line refers to $n = 0.0$ and $m^* = 1.3$, whilst the dash line to $n = 0.3$ and $m^* = 1.3$.

Two loading conditions were considered. The first assumes a cantilever beam subjected to pure bending, while the second example considers a cantilever beam subjected to a combined loading: bending moment and axial force. The deformed shapes for a beam with a circular cross-section are presented in figure 4.8. As expected, for the same loading state, the non-dimensional deflection obtained using an elasto-plastic material with non-linear hardening is lower. This is due to the increased strength of the material attributed to the strain hardening. A smaller elastic recoil is observed when an axial force is applied. In manufacturing processes, like metal forming, the estimation of the elastic recoil is fundamental in determining the load to which the solid must be subjected so that the desired final shape is obtained. The results obtained using the analytical model are compared here against those obtained using a finite element approximation. The analysis has been performed using the Finite Element Analysis commercial code Abaqus®. The cantilever beam is discretised using the beam element B23, which does not allow for shear deformation, but has stretch degrees-of-freedom. The beam is fixed at its left end and it is loaded by prescribing a compressive axial force and shear force at the right end. The analytical (solid lines) and computational (dashed lines) results are in good agreement, as shown in figure 4.9 (a). The application of the axial force results in the shift of the neutral axis and axial strain. The analytical model takes into consideration only the change of position of the neutral axis; therefore, the slight

difference between analytical and FEM results can be attributed to the absence of the stretch in the model earlier developed.

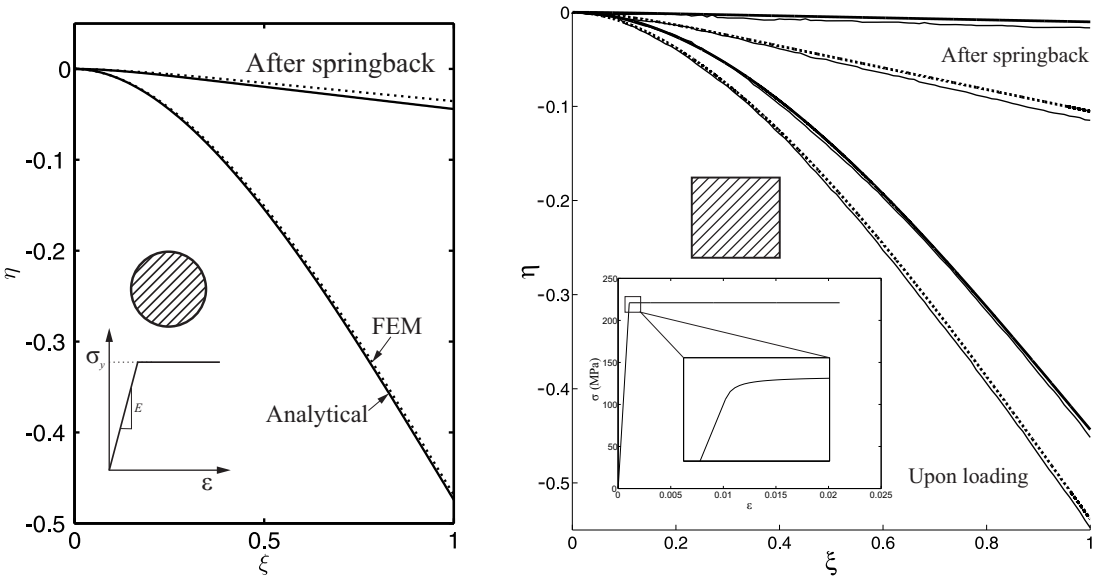

Figure 4.9: (a) Comparison of the elasto-plastic deformed shape and spring-back obtained using the analytical model (solid lines) developed here and the commercial Finite Element software Abaqus (dash lines) for $m^* = 1.3$ and $n = 0.3$ for a circular cross-section. (b) Comparison deflections of the cantilever beam with rectangular cross-section between the current model (thick lines) and Yu and Johnson model (thin lines) [67]. The thick solid lines correspond to $m^* = 1.3$ and $n = 0.3$, while the thick dash lines to $m^* = 1.3$ and $n = 0.0$. The beam is made of an elastic-perfectly-plastic material, which is modelled using the hyperbola. Note the sharp corner that gives the visual appearance of the elastic-perfectly-plastic material, however this is deceptive (see inset).

The validation of the mathematical model for a beam with a rectangular cross-section has been performed by comparing the current results with those obtained by Yu and Johnson [67], which used an elastic-perfectly-plastic model. This ideal material cannot be exactly simulated since a singularity appears in the stress-strain curve. However, a really good approximation is obtained (see inset of figure 4.9 *b*). The parameters of the hyperbola obtained from the genetic algorithm for the interpolation of an elastic-perfectly-plastic materials are $A = -0.111 \times 10^{-4}$, $B = -220$ MPa and $D = 2.32 \times 10^{-2}$ MPa. Note that the parameter $-B$ represents the horizontal asymptote and for an elastic-perfectly-plastic ideal material it corresponds to the yield stress σ_y. The deformed shape during the loading and unloading for two different combinations of m^* and n have been plotted, as shown in figure 4.9 (*b*). The thin lines are the results obtained by Yu and Johnson model [67], while the thick solid and dash lines are those obtained using the model developed here. The deformed shapes obtained by applying the current model closely resemble those of Yu and Johnson. The difference is due to the slightly imprecise approximation of the constitutive material law using the hyperbolic model. When no

axial force is applied, the neutral axis is located at the middle of the section; therefore, primary and secondary plastic regimes start simultaneously. This results in an equal value of x_1 and x_2. When $m^* = 1.3$ and $n = 0$, $\xi_1 = \xi_2 = 0.2308$ which exactly matches Yu and Johnson result [67].

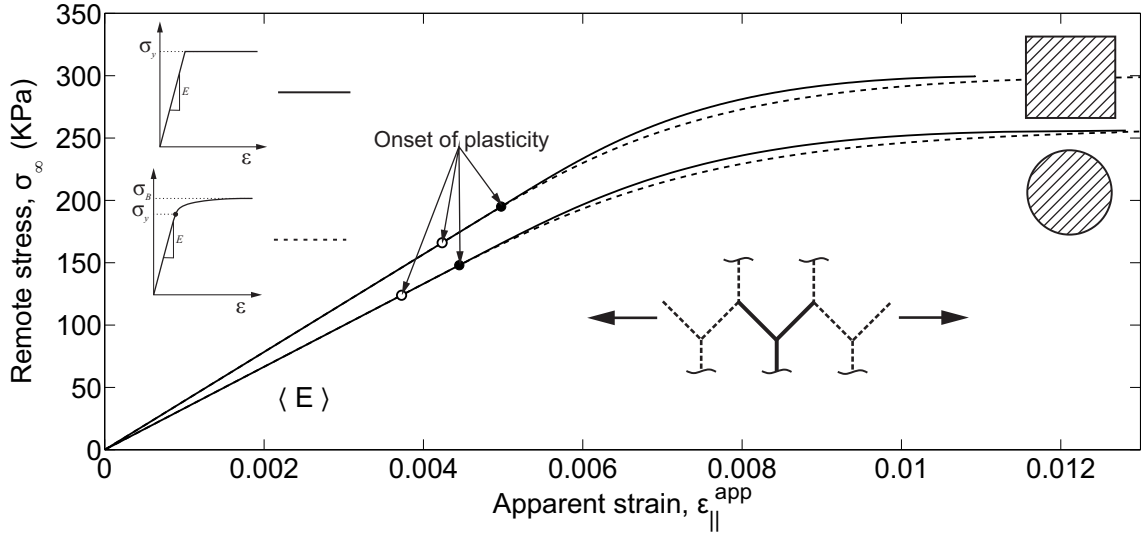

Figure 4.10: Remote stress as a function of apparent strain. The solid lines are those obtained assuming an elastic-perfectly-plastic constituent material ($E = 209$GPa and $\sigma_y = 240$MPa). The dash lines are obtained when a material with hyperbolic hardening is considered ($E = 209$GPa, $\sigma_y = 200$MPa and $\sigma_B = 240$MPa). A regular hexagonal cell is assumed, therefore $l = h$ and $\theta = \pi/6$. The two cross-sections have the same total area.

The effective elasto-plastic properties of the lattice structure can be inferred from the response of the tilted struts. A comprehensive study of this subject for two-dimensional lattice structures has been carried out in Chapter 3. However, the effects of material hardening were not taken into consideration. The cell walls (or filaments for a 3D printed lattice) can be adequately modelled as a cantilever beam when they are thin. The mechanical response of a lattice sheet is related to the strut response through the geometric parameters. For a hexagonal cell of edge length l, height h and internal angle θ (see, figure 3.1), strain along and across the direction of the load application are given by $\epsilon^{||}_{\text{app}} = w_{tip} \tan\theta / l$ and $\epsilon^{\perp}_{\text{app}} = 2 w_{tip} \cos\theta / (2l \sin\theta + h)$, where w_{tip} is the deflection of the tip of inclined members with respect to their roots, measured transverse to them. Having developed the response of a beam, we are now in a position to quantitatively present the apparent non-linear response of such structured material. The relation between remote stress and the load applied at the end of the strut has been extensively presented in the previous chapter and it is given by equations (3.1) and (3.3). When remote stress is applied, the initial phase is purely elastic. Gibson *et al.* [3] studied the apparent modulus of elasticity $\langle E \rangle$ when the cross-section of the struts is rectangular. The values thus obtained for the apparent modulus match up to 4 significant figures with the well known benchmark results of Gibson and Ashby [33], as previously stated in Chapter 3.

By using beam theory to model the cell walls, we are able to calculate the apparent modulus of elasticity when the struts have a circular cross-section. The expression is given by $\langle E \rangle = (3\pi E/2)(r/l)^3 \cos\theta/(h/l+\sin\theta)\sin^2\theta$ (more details in Appendix B). The values of the apparent elastic modulus obtained using the above closed form expression for low values of remote stress match up to 4 significant figures with the values obtained from the linear part of the two curves in figure 4.10. Upon further loading, deformations become elasto-plastic which is associated with the non-linear part of the response in figure 4.10 (the rectangular cross-section and the circular cross-section have the same total area). Note that the tangent modulus at the onset of plasticity shows continuity for both the constituent materials assumed. This is in contrast with the elastic-perfectly-plastic model, which shows a point of discontinuity of the tangent modulus at the point of yielding. This is because the plastic zones smoothly spread along the struts and through the thickness, as extensively explained in the previous chapter.

4.3 An additional illustrative example: press-brake bending of a metal rod

The results obtained above for a cantilever beam can be applied to several other engineering problems, such as manufacturing processes that are not the main concern of the present dissertation. Consider a press-brake bending of metal rod, as shown in figure 4.11 (a). Observed the symmetry of the problem, half of the rod can be modelled as a cantilever beam. Here the bending moment varies along the length of the beam and an axial force is applied additionally. The rod is of circular cross-section with radius r, clamped at one end and subjected to a concentrated force F at the tip inclined at an angle α, as shown in figure 4.11 (b). The inclination of the reaction from the die is a consequence of the direction of the normal to the die surface. Thus the geometry of the problem enforces simultaneous presence of significant axial force and bending moment. Thus the problem reduces to the model for a cantilever beam presented in the previous section.

4.4 Conclusions

Analytical models incorporating the influence of axial force on elasto-plastic response and springback of honeycomb lattices were developed here. Such an analysis was previously performed in Chapter 3 for a strut with a rectangular cross-section made of elastic-perfectly-plastic constitutive model was assumed. This has been extended to introduce the effects of material hardening using a constitutive model proposed here and it has been generalised for an additional strut geometry.

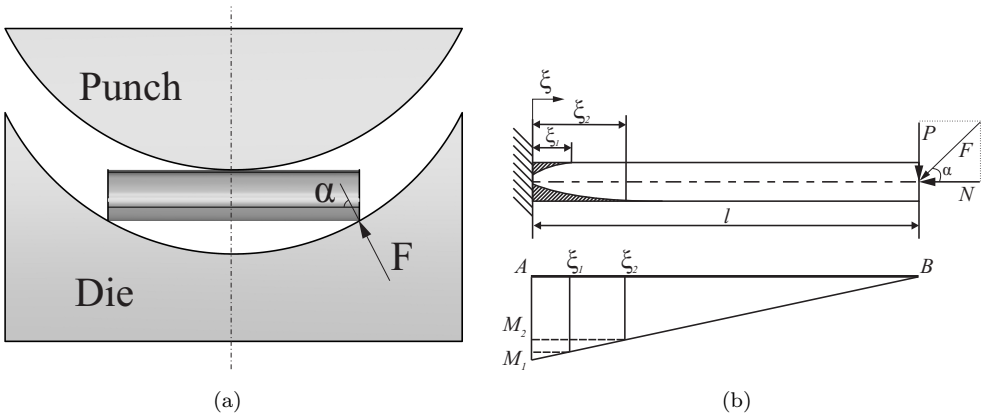

Figure 4.11: (a) Press-brake bending of a metal road (b) Half of the work piece modelled as a cantilever beam with axial and shear components. The hatched areas are the plastic zones that spread along the beam while the load is increased.

The calculation of the elasto-plastic response of honeycomb is reduced to that of a single strut, which can be modelled as a cantilever beam in conjunction with the kinematics of the lattice deformation. It was possible to account for the hardening effect by introducing a novel mathematical description of the stress-strain curve which combines a straight line with a translated rectangular hyperbola. This mathematical representation of the material constitutive law gives us the possibility to exactly model the linear-elastic behaviour at low strain in addition to that in the plastic regime. Elastoplastic analysis using the hyperbolic material hardening model was performed for both rectangular and circular cross-sections. The relationships developed here are able to provide the full non-linear lattice response without the use of finite element procedure. The usefulness of such analytical approaches arises at early stages of designs, when we are not interested in the accurate response calculation of those structured materials. Also, analytical results contain useful information with regards to the sensitivity of the response to the parameters of the problem–something that all computational results lack.

Chapter 5

Stress analysis of cylindrical periodic structures and its application to stent design

Elasto-plastic response and recoil analysis were presented for flat 2D lattices in Chapters 3 and 4. We now consider structures, such as those frequently encountered in stents, where periodicity is over a cylindrical surface. The usefulness of the analyses previously carried out for planar lattices will become apparent. The stent is a cylindrical structure that possesses periodicity along its length and the circumferential direction. Some examples of "flattened" stents are shown in figure 5.1. These architectures possess generic common geometric features in that they contain crowns that are connected by straight or curved bridges, to provide flexibility during the deployment. In this dissertation, we develop an analytical framework to characterise the expansion of stents, a phase of implantation that is critical from the point of view of mechanical performance. The realism of actual stent geometries is deliberately compromised in order to gain insight into the mechanical behaviour of structures of this class experiencing high plastic deformation. The curved crown has been represented as an infinite sinusoid made of an elastic-perfectly-plastic material. By using an energy minimisation technique, for this simplified, yet reasonably detailed model, analytical expressions for the response of such periodic cylindrical structures are derived.

The present chapter provides insight into the mechanical behaviour of these bio-structures that experience deformation past yielding by using a simplification in the material model combined with an abstraction of the actual stent geometry. Practical guidelines for the design of novel stents will be provided. This simplified problem possesses all the generic features of stent mechanics and the derived model has been directly applied to the development of a new stent prototype in the next chapter. The benefits and effectiveness of mathematical analysis within a practical context have been found to be very satisfactory.

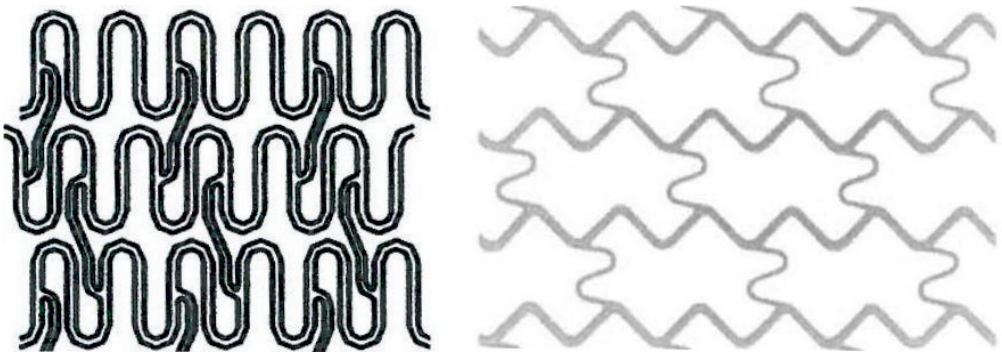

(a) Coroflex stent pattern

(b) Duraflex^{TM} stent pattern

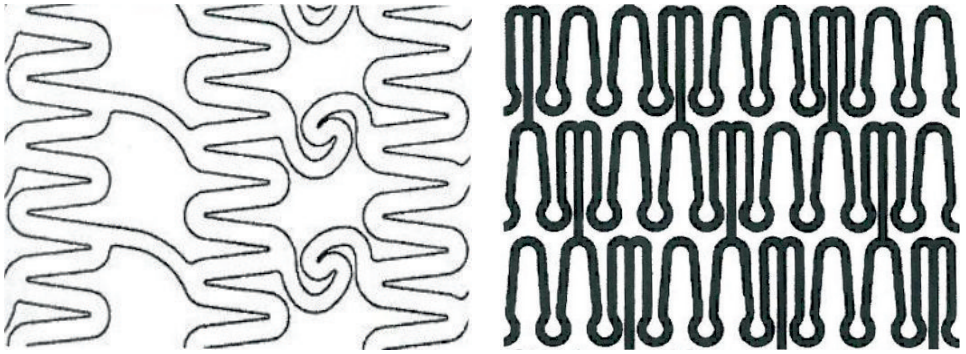

(c) JOSTENT$^{®}$ Flex stent pattern

(d) Multi-Link Ultra^{TM} stent pattern

Figure 5.1: Features of existing stent geometries [130]. They show periodic crowns connected by straight or curved bridges.

5.1 Crown plasticity and the apparent response of a periodic cylindrical structure

Consider the two planar architectures shown in figure 5.2. The planar lattice is a pattern similar to those in figure 5.1, with significant changes in the unit cell geometry. A stent could be constructed by rolling the planar lattice onto a cylinder. Consider an infinite cylindrical periodic structure, which is made of sinusoidal crowns connected to each other through straight links, also known as bridges, as shown in figure 5.3 (a) and (b). The cylinder is loaded with a uniform internal pressure, denoted by p, as shown in figure 5.3 (a) and (b). The arrangement of the connections gives raise to two different behaviours. If the bridge links the valley of the upper crown with the peak of the lower crown, by applying the internal pressure, the cylinder expands radially, while *shortening* in the axial direction (see figure 5.3 a). We will refer to this geometry as *convex honeycomb* since the topology of the flattened out structure resembles that of a hexagonal lattice structure whose straight inclined members have been smoothly connected, giving the appearance of a sinusoid. If the linkage connects peak-valley of the upper and bottom crown respectively, then the pressurised cylinder expands radially and elongates longitudinally (see figure 5.3 b). This is a manifestation of a negative apparent

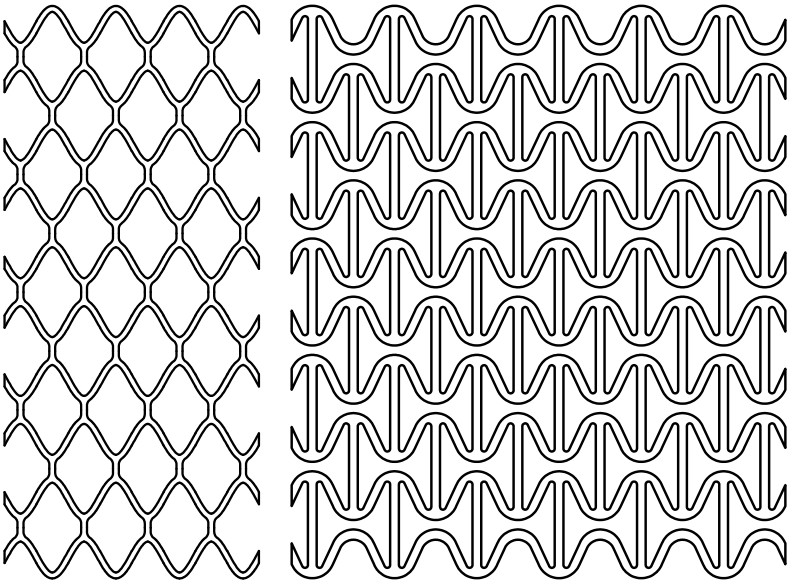

(a) Convex honeycomb (b) Auxetic honeycomb

Figure 5.2: Features of two novel stent geometries. (a) The structure possesses positive apparent Poisson's ratio, thus when inflated it shortens axially. (b) The structure possesses negative apparent Poisson's ratio, thus when inflated it elongates axially. They will be studied in detail in the next chapter.

Poisson's ratio of the structure; therefore, we will refer to this structure as *auxetic*. The geometric parameters of the sinusoidal crown are defined in figure 5.3 (*c*). In many real stents, the thickness of bridges is smaller than the crown since they are mainly used to achieve flexibility in the structure during the deployment. However, here we restrict our attention to a structure with constant thickness, i.e. both crowns and bridges have the same thickness in the circumferential direction. The constituent material is assumed to be elastic-perfectly-plastic, thus no hardening occurs beyond yield. The stress-strain curve of the idealized material is shown in figure 5.3 (*d*), where E is the Young's modulus and σ_y is the yield stress.

When a stent is subjected to internal pressure, the crowns undergo bending and stretching. If the curvature effects are neglected, the study of the stent expansion can be related to the in-plane stretch of an infinite open-up periodic lattice structure loaded at infinity (see figure 5.3 *a* and *b*). This approach allows us to simplify the analysis by avoiding the unnecessary complications arising from the shifting of the neutral axis caused by the curvature, while capturing the essential features of the stent expansion. The mirror symmetry with respect to the vertical linkages (see figure 5.2), combined with the vertical equilibrium, dictates that the bridges are stress-free. Therefore, the structural response is only given by the deformation of the curved members and the study can be reduced to that of an infinite periodic curved beam under remote tensile loading.

Pressure p is applied to the inner surface of the cylinder. If we cut the cylindrical structure with a plane parallel to the longitudinal direction, the only stress counteracting

the internal pressure is the hoop stress, σ_H. By enforcing the equilibrium between pressure and stress normal to the cutting plane, we obtain the relationship between internal pressure and the hoop stress $\sigma_H = pS_p/(2tb)$. Here t and b are thickness and width of the strut, respectively and $S_p = S \times (2/\pi)$ is the projection of half of the inner surface of the cylindrical structure (S) on the horizontal plane, as shown in figure 5.3 (a) and (b). The width b in the radial direction is often referred to as the "thickness" of the stent in clinical literature; however, as the mechanics of struts is dominated in the hoop-direction, we choose to call the tangential dimension t as thickness. In the analysis presented here, the crown is modelled as an unfolded periodic curve under tensile force

$$F = \sigma_H \times tb = pS_p/2, \tag{5.1}$$

which is related to the inner pressure through the hoop stress σ_H from the expression given above.

In many engineering problems, the failure is identified with reaching of the yield stress within the structure. However, there are applications where calculation of the complete plastic response is required, such as during the deployment of biomedical stents. The conventional assumptions of thin beam theory are accepted here. Firstly, plane cross-sections remain plane upon loading. Secondly, the amplitude A and the wavelength λ of the sinusoid is much greater than the cross-section dimensions; therefore, the shear-stresses are ignored. Finally, the deformation is smaller than the sinusoidal amplitude.

Energy principles are effective alternative methods to obtain structural response of complex systems. They enable us to solve structural problems approximately without solving governing partial differential equations. The well-known Castigliano's second theorem relates the linear displacement in the direction of an applied force to the first derivative of the strain energy of the system with respect to the generalised force. When the deformation is non-linear, Castigliano's theorem does not hold any more. Its generalised form is given by the Crotti-Engesser theorem $\delta_i = \partial C/\partial F_i$ [64], where δ_i is the generalised displacement in the direction of the applied force F_i and C is the complementary energy, given by the area above the stress-strain curve, as shown in figure 5.3 (d). Although C has energy units, it does not have any physical meaning.

When a flat wavy periodic configuration is loaded with uniaxial remote stress, the sinusoidal crowns bend and stretch. A typical unit curved member is represented in figure 5.3 (c). The stretch part is ignored here–an approximation frequently used and as shown in Chapter 3. The symmetry of the geometry allows us to reduce the study of the unit sinusoid wave to only a quarter of it. The current approach uses the energy minimisation along the curved segment to calculate the displacement δ of the extreme point, where F is applied. The moment along the studied sector is given by $M = FA \sin kx$, where $k = 2\pi/\lambda$. Here λ is the wavelength of the structure, as shown in figure 5.3 (c). The maximum bending moment along the length of the curved segment appears at the peak

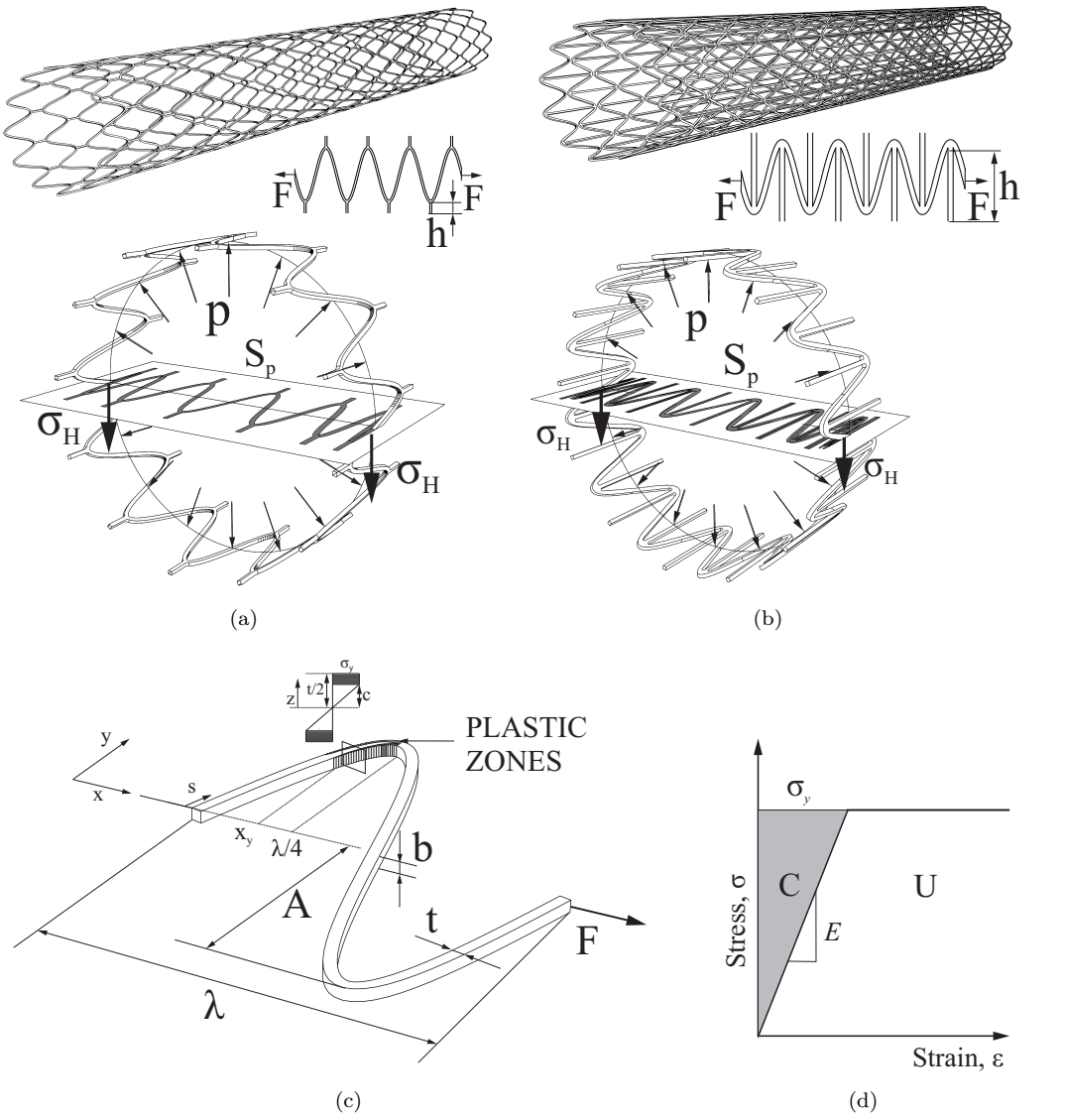

Figure 5.3: Infinite cylindrical structures made of crowns periodically connected to each other through straight bridges. The configuration in figure (a), when pressurised, expands radially but contracts along its length, as opposed to the geometry in figure (b) that expands radially while elongating. (c) Parameters of the unit sinusoid, part of the circular crown. (d) Elastic-perfectly-plastic material law of which the cylindrical structure is made of, where U is the strain energy and C the complementary energy.

and is given by $M^* = FA$. If the maximum bending moment is less than the yield moment $M_y = \sigma_y \times bt^2/6$, then the all structure is only under elastic deformation. In the case of linear elastic deformations, the complementary energy is equal to the strain energy and it is given by

$$C = U = \frac{1}{2EI} \int_0^l M^2 \mathrm{d}s \tag{5.2}$$

where U is the strain energy, EI the bending stiffness, l the length of the analysed segment and s the intrinsic coordinate along the curved segment. Substituting the

expression for M and changing the integration variable yield to

$$C = \frac{(FA)^2}{2EIk} \int_0^{\lambda/4} \sin^2(kx) C_{\mathrm{ds/dx}} \mathrm{d}x \tag{5.3}$$

where $C_{\mathrm{ds/dx}} = \sqrt{1 + C_1 \cos^2(kx)}$ and $C_1 = (kA)^2$. Applying Castigliano's theorem, the displacement along the x direction for the whole sinusoidal beam is given by

$$\delta = \frac{4F}{EI} \frac{1}{3k^3} C_{\mathrm{Elliptic}}, \tag{5.4}$$

where $C_{\mathrm{Elliptic}} = (C_1 + 1)\, K\,(-C_1) + (C_1 - 1)\, E\,(-C_1)$. Note that $K(-C1)$ and $E(-C1)$ are the complete elliptic integrals of the first and second kind respectively[1]. The factor of four derives from the fact that only one fourth of the sinusoid was considered during the calculation of the strain energy.

The expression in equation (5.4) is valid only so long as the maximum moment is less than or equal to the yield moment of the cross-section. When the force F is further increased, the sinusoidal curved beam undergoes elasto-plastic deformation. All the fibres in the cross-section do not plastically deform simultaneously which leads to the formation of plastic zones spreading along the segment, as shown in figure 5.3 (c) by the dashed area. Part of the segment remains completely elastic, this occurs for $0 \leq x \leq x_y$, where x_y is the value of x at which $M = M_y$. For $x_y < x \leq \lambda/4$, is the region of plastic deformation, where the outer fibres of the cross-section are under plastic deformation, but the inner fibres remain elastic. We neglect the stretch component and the shift of the neutral axis, thus yield occurs symmetrically on both sides of the segment. The distance between the neutral axis and the first yielded fibre is denoted by c (figure 5.3 c).

The total complementary energy of the segment is given by the sum of the complementary energy of the elastic and the plastic region. The elastic contribution is given by

$$C_{\mathrm{elastic}} = \frac{(FA)^2}{2EIk} \int_0^{x_y} \sin^2(kx) C_{\mathrm{ds/dx}} \mathrm{d}x \tag{5.7}$$

where $x_y(F) = \arcsin\left[M_y/(FA)\right]$ is the axial coordinate at which the transition between elastic and plastic region occurs. The computation of the complementary energy of the plastic region is more complicated. It is useful to introduce a new quantity called *complementary energy density function*, $u_c = 1/2 \int_0^{\sigma} \epsilon \mathrm{d}\sigma$ for the fibres in the cross-section

[1] The complete elliptic integral of the first kind is defined as

$$K(m) = \int_0^{\pi/2} \frac{1}{\sqrt{1 - m \sin^2\theta}} \mathrm{d}\theta, \tag{5.5}$$

whereas the complete elliptic integral of the second kind is defined as follow

$$E(m) = \int_0^{\pi/2} \sqrt{1 - m \sin^2\theta} \mathrm{d}\theta. \tag{5.6}$$

under elastic deformation and those under plastic deformation

$$\begin{cases} u_c^{\text{elastic fiber}}(x,z) = (1/2) \times (\sigma_y z/c)^2/E & \text{if } 0 \le z \le c(x) \\ u_c^{\text{plastic fiber}}(x,z) = (1/2) \times (\sigma_y^2/E) & \text{if } c(x) \le z \le t/2 \end{cases} \tag{5.8}$$

where z is the coordinate along the thickness, E the Young's modulus and σ_y the yield stress of the constituent material. The energy density is indirectly a function of x through the distance of the first yielded fibre from the neutral axis $c(x)$. Imposing the moment equilibrium at the cross-section leads to $c(x) = \sqrt{3\,(t^2/4 - FA\sin kx/(\sigma_y b))}$. The complementary energy of the plastic region is given by

$$\begin{aligned} C_{\text{plastic}} = \frac{2b}{k} \Bigg(& \int_{x_y}^{\lambda/4} \int_0^{c(x)} u_c^{\text{elastic fibers}} \mathrm{d}z C_{\mathrm{d}s/\mathrm{d}x} \mathrm{d}x + \\ & \int_{x_y}^{\lambda/4} \int_{c(x)}^{t/2} u_c^{\text{plastic fibers}} \mathrm{d}z C_{\mathrm{d}s/\mathrm{d}x} \mathrm{d}x \Bigg) \end{aligned} \tag{5.9}$$

which is obtained by integrating the complementary energy density across half of the thickness ($0 \le z \le t/2$) and along the segment undergone plastic deformation ($x_y < x \le \lambda/4$). Because the stress distribution is symmetric across the cross-section, the total complementary energy of the plastic region is obtained by multiplying by a factor of two. Substituting equation (5.8) into (5.9) and simplifying, results into

$$C_{\text{plastic}} = \frac{2b}{k}\frac{\sigma_y^2}{E} \left(\frac{t}{4} \int_{x_y}^{\lambda/4} C_{\mathrm{d}s/\mathrm{d}x} \mathrm{d}x - \frac{1}{3} \int_{x_y}^{\lambda/4} c(x) C_{\mathrm{d}s/\mathrm{d}x} \mathrm{d}x \right). \tag{5.10}$$

The complementary energy C_{plastic} is an implicit function of F via x_y. Therefore, the displacement in the direction of the applied force F, given by $\delta = 4 \times \partial(C_{\text{elastic}} + C_{\text{plastic}})/\partial F$, is computed using Leibniz's rule for differentiation under the integral sign. The final expression for δ is reported in the Appendix C, together with a more detailed derivation of equation (5.10).

The theoretical model developed above can now be used to assess the mechanical properties of a periodic tubular structure. In the area of stent design, the relationship between internal pressure p and change in radius Δr is a measure of the mechanical behaviour of the device during the expansion. The horizontal displacement of the sinusoid can be directly related to the change in radius of the cylindrical structure using the relationship

$$\Delta r = n\delta/(2\pi), \tag{5.11}$$

where n is the number of sinusoids along the circumference. By using the above expression for δ we are now in a position to analytically obtain the $p - \Delta r$ relationship, where the relation between p and F is given by equation (5.1).

5.2 Results and discussions

Graphical presentation of analytical results together with computational verifications of the non-linear response in the plastic regime, effects of the curvature, influence of shear stress on the overall response and generic scaling arguments are provided in this section. The application of such analysis to the design of a real stent is also presented. These results are organised into several subsections with in-depth discussion.

5.2.1 Non-linear elasto-plastic response of infinite open-up wavy structure

Having developed an analytical expression for the response of an infinite wavy beam beyond yielding by using the energy minimisation theorem, we are now in a position to quantitatively present the response of real open-up wavy structures. When a curved beam is stretched at infinity, the initial part is purely elastic as the whole structure is under elastic deformation. In this phase, the displacement varies linearly with the force and the relationship is given by equation (5.4). The part of the curve in figure 5.4, from the origin to the point labelled "onset of plasticity" represents the linear elastic regime. When the curved beam yields beyond the elastic limit, the force-displacement relationship becomes non-linear. Equation (C.1) in Appendix C can be taken as the relationship for the sinusoid under plastic deformation. Note that the tangent modulus at the transition point is continuous although the stress-strain curve of the constitutive material shows discontinuity at the point of yielding. This is because the plastic zones smoothly evolve along the beam and the whole structure does not become plastic simultaneously. Despite the discontinuity of the parent material curve at the yield point, the force-deflection curve is smooth at the transition from elasticity to plasticity.

The agreement between the analytical results presented here and the computational results, which are obtained by the finite element method, is excellent for the whole range of elasto-plastic response up to the point of collapse. The solid line in figure 5.4 is the analytical response obtained from the above presented model. The dash-dot line corresponds to the computational result. The sinusoid has been modelled as a 3D structure using the element type C3D8I (8-node brick element) within the commercial software ABAQUS. An ideal elastic-perfectly-plastic material with Young's modulus (E) of 209 GPa and yield stress (σ_y) of 240 MPa has been used. At the collapse point, the force difference is only 1.5%. It is interesting to note that the absence of the shifting of the neutral axis because of the curvature of the beam and the stretch in the model, slightly underestimates the required force at collapse.

Consider now the role of geometric non-linearity as it may be claimed to have a notable influence on the response of the curved beam. The unit cell simulation was run again in ABAQUS while including geometric non-linearity in addition to stretch. The result

shown in the inset of figure 5.4 shows an overall softening of the structure. For a slender curved beam (wave amplitude to thickness ratio equal to 20), the stretch has a greater influence on the mechanical response than the geometric non-linearity.

The model of sinusoid plasticity developed here ignores the presence of bridges used to interconnect sequential crowns. Because of the symmetry, they do not deform. The effect can be easily assessed computationally and this is presented in figure 5.4. The dashed line represents the computational results assuming an auxetic unit cell (as shown in the top inset). The dotted line is a plot of the response of the unit convex honeycomb cell (as shown in the bottom-left inset). The computational results for the two unit cells are in good agreement with the analytical model. However, a slight overall stiffening of the structure is observed. The connection between crowns and bridges is not an ideal point, as assumed in the analytical model. The area near the junction at which the wavy beam and the bridges meet undergoes deformation, as shown in the two enlargements in figure 5.4. This corresponds to extra material, not considered in the theoretical model, which is able to resist the applied load. This justifies the slightly higher structural stiffness obtained for the auxetic and honeycomb configurations.

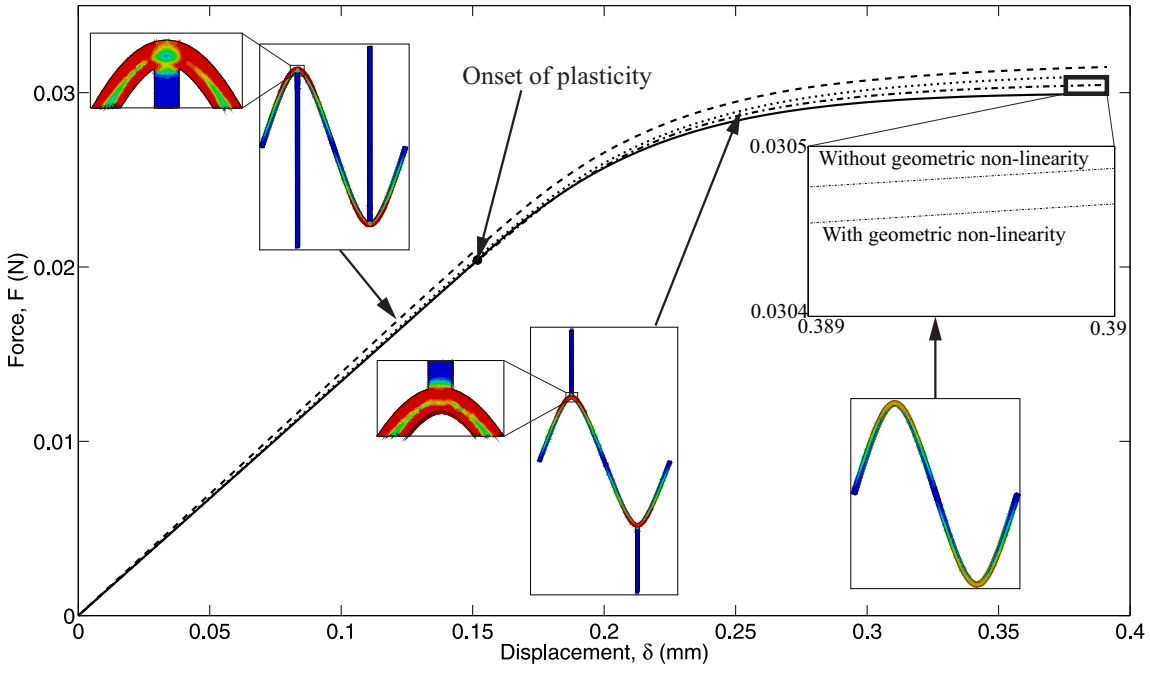

Figure 5.4: Elasto-plastic response of an infinite sinusoidal curve. The solid line is the analytical results while the dash-dot line that obtained using finite elements. The analysed sinusoid has $A = 2$ mm, $\lambda = \pi$ mm and $b = t = 0.1$ mm made of an elastic-perfectly-plastic material ($E = 209$ GPa and $\sigma_y = 240$ MPa). The computational results for the corresponding convex honeycomb and auxetic configurations, having bridges of high $h_{\text{Honeycomb}} = 2$ mm and $h_{\text{Auxetic}} = 4.5$ mm respectively, are in good agreement with the analytical results.

5.2.2 Curvature effects on the cylinder response

The analytical approach developed here affords results for a cylindrical periodic structure under internal pressure in a closed form. The model uses an unrolled configuration loaded remotely with tensile stress, which is related to the applied pressure through equation (5.1). The theoretical study does not take into consideration the curvature effects due to the rolling of the planar configuration. This section aims to assess the effect of the global curvature computationally.

Consider n number of sinusoids of amplitude A, wavelength λ, thickness and width constant within a crown. By increasing the number of sinusoids, the curvature effects decrease and the mechanical response corresponds to that of the planar configuration. The computational results are presented in figure 5.5. By increasing the number of sinusoids over the circumference we observe that when the radius of the cylinder r and the wavelength λ of the sinusoid are comparable (cylinder radius to wavelength ratio equal to 1), the effects of the curvature are noticeable. At the collapse point, the force is underestimated by around 8.2%, which is still a satisfactory result for a closed-form solution. Under the condition of radius of the cylinder to wavelength ratio greater than 3, the response of the pressurised cylinder is accurately estimated by the planar structure under tensile loading.

After assessing the influence of the curvature, the computational analysis of the expansion of the cylinder has been performed for the correspondent convex honeycomb and auxetic structures with $r/\lambda \approx 3$–assuming the same sinusoidal parameters. As expected, the mechanical responses appear exactly like that in figure 5.4, where the results for the planar configurations have been presented. When a sufficient number of sinusoids n along the circumference are present, the curvature effects are minimal and the response of the cylinder is accurately estimated by the open-up stretch configuration.

5.2.3 Scaling arguments and data collapse

The analytical approach presented here gives benchmark results for the elasto-plastic analysis of cylindrical periodic structures made of sinusoidal crowns interconnected by vertical bridges. An additional reward of such analysis is the ability to infer trends of the behaviour and the dependence of the mechanical response on the parameters of the problem. In this spirit, we propose a scaling ansatz that embodies the behaviour of all cylindrical periodic structures, with the assumed geometrical features, under plastic deformation.

Having considered the response of such unrolled periodic lattice structures that differ in the location of the bridges and their lattice parameters, i.e. half length of the bridge h, we are now in a position to separate the crown mechanics from the kinematics of

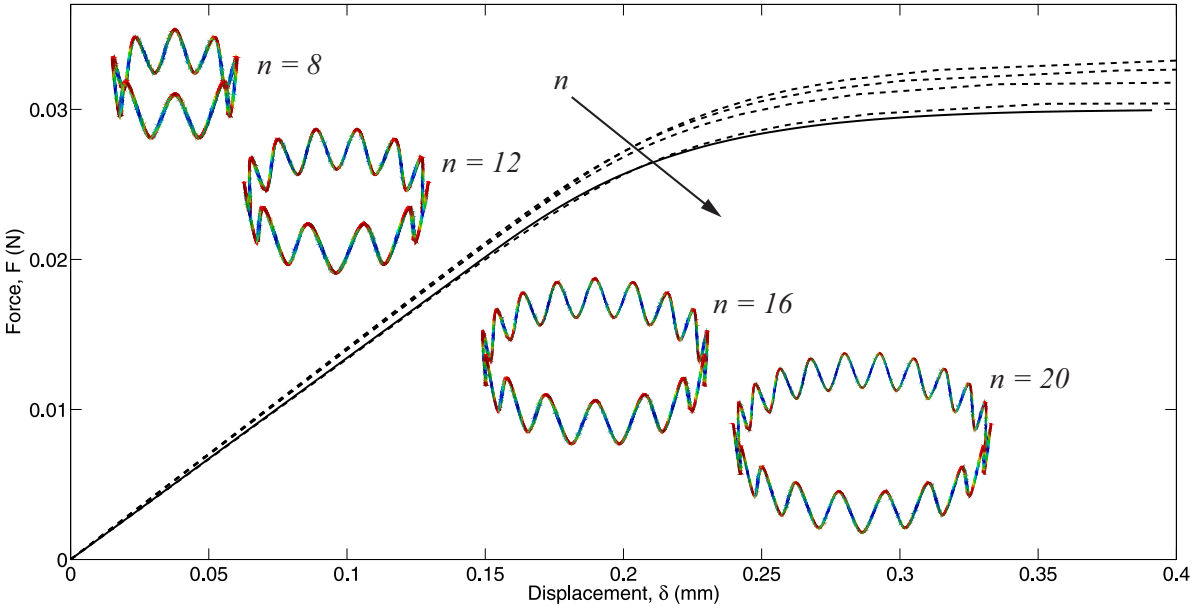

Figure 5.5: Numerical assessment of the effects of the curvature on the elasto-plastic response. The ratio r/λ has been gradually increased $4/\pi$, $6/\pi$, $8/\pi$, $10/\pi$ until the response of the sinusoidal crown resembles that of the flat configuration. Therefore, the effects due to the shift of the neutral axis because of the curvature can be neglected for $r/\lambda \approx 10/\pi$.

lattice deformation. The force vs displacement curves of the elasto-plastic response of such periodic structures show similarities and this suggests the existence of scaling variables and renormalisation groups. Consider a sinusoidal crown with transverse load F, amplitude A, wavelength λ, thickness t and depth in the direction perpendicular to the plane of deformation b. The elastic-perfectly-plastic material model is described by the Young's modulus E and yield stress σ_y. The longitudinal displacement for the sinusoid is given by δ. Now we develop a scaling relationship for the elasto-plastic response.

Consider the functional relationship $\delta = \delta(F, E, \sigma_y, A, \lambda, t, b)$, which is a 7-variable problem. By applying Buckingham's π-theorem, the variables can be reduced by two, which is the number of primary dimensions in the problem (respectively length and mass). Therefore, the above functional relationship take the non-dimensional form of $(\delta/A) = f_1\left(\left(F/EA^2\right), (\sigma_y/E), (\lambda/A), (t/A), (b/A)\right)$. Dimensional analysis cannot help us any further. We need simplifications and physical understanding of the mechanical behaviour in order to derived scaling laws. Firstly, by assuming that the displacement field is independent of the depth direction of the sinusoid, we can combine the first and last non-dimensional group so that F/b appears together as a single π-group. This results in

$$(\delta/A) = f_2\left((F/bEA), (\sigma_y/E), (\lambda/A), (t/A)\right). \tag{5.12}$$

This resembles the analysis presented in Chapter 3 for the development of a scaling relationship for the elasto-plastic response of honeycombs. The analysed problem was

characterised only by one length scale (length of the inclined struts). Therefore, it has been possible to find a unique relationship between applied force and geometric parameters. The sinusoid is two length-scale parameters problem, involving amplitude A and wavelength λ, which gives origin to an extra π-group. By making use of the beam-curvature relationship, as previously done in Chapter 3, the t/A dependence is integrated in the first non-dimensional group. The functional relationship in equation (5.12) becomes

$$\frac{\delta}{\sigma_y A^2/Et} = f\left(\frac{F}{\sigma_y bt^2/A}, \frac{\lambda}{A}\right), \tag{5.13}$$

where f is a complicated unknown function. Therefore, the current problem is fully described by three π-groups and it cannot be further reduced. We can clearly see that $\delta \sim (t/A)^3$, which is typical of a structure whose deformation is primarily determined by bending.

We renormalise the mechanical response according to $\overline{\delta} = \delta/(\sigma_y A^2/(Et))$ and $\overline{F} = F/(\sigma_y bt^2/A)$ so that we get a *family of 'master-curves'* describing the non-linear elasto-plastic behaviour of sinusoids as functions of λ/A. This family includes all geometric and material parameters relevant to the mechanics of the sinusoid and it is plotted in figure 5.6. The mechanical response for geometries having the same λ/A value collapses to the same curve. Two critical points on the curve (i) the transition to plastic deformation (labelled 'onset of plasticity') and (ii) the plastic collapse at which a cross-section becomes fully plastic are highlighted. At the onset of yielding, the value of the non-dimensional force is $\overline{F}_{\text{Yield}} = 1/6$. The corresponding value at the collapse is $\overline{F}_{\text{Collapse}} = 1/4$. These values are obtained from the analytical expression for beam elasto-plasticity. Making use of equation (5.4) and the definition of $\overline{\delta}$ and $\overline{F}$, the stiffness of the periodic sinusoidal structure $\langle E\rangle_{\overline{F}-\overline{\delta}}$ is given by

$$\langle E\rangle_{\overline{F}-\overline{\delta}} = \frac{\pi^3}{2C_{\text{Elliptic}}}\left(\frac{A}{\lambda}\right)^3, \tag{5.14}$$

from which we can derive $\overline{\delta}_{\text{Yield}} = \overline{F}_{\text{Yield}}/\langle E\rangle_{\overline{F}-\overline{\delta}}$. The expression for the stiffness of the planar configuration shows the inverse proportionality with respect to λ/A. This demonstrates that geometries with a smaller λ/A ratio possess a higher apparent Young's modulus; therefore, they have a higher elastic stiffness.

5.2.4 Application of the analytical model to stent design

Computational modelling is a common tool used to assess stent performance; however, it requires large computational resource and time. The analytical framework developed above aims at quantifying the mechanical properties of periodic tubular structures when subjected to radial expansion. This can render the design process of such a device quick and efficient. The aim of the scaffold is to provide support to the artery to restore

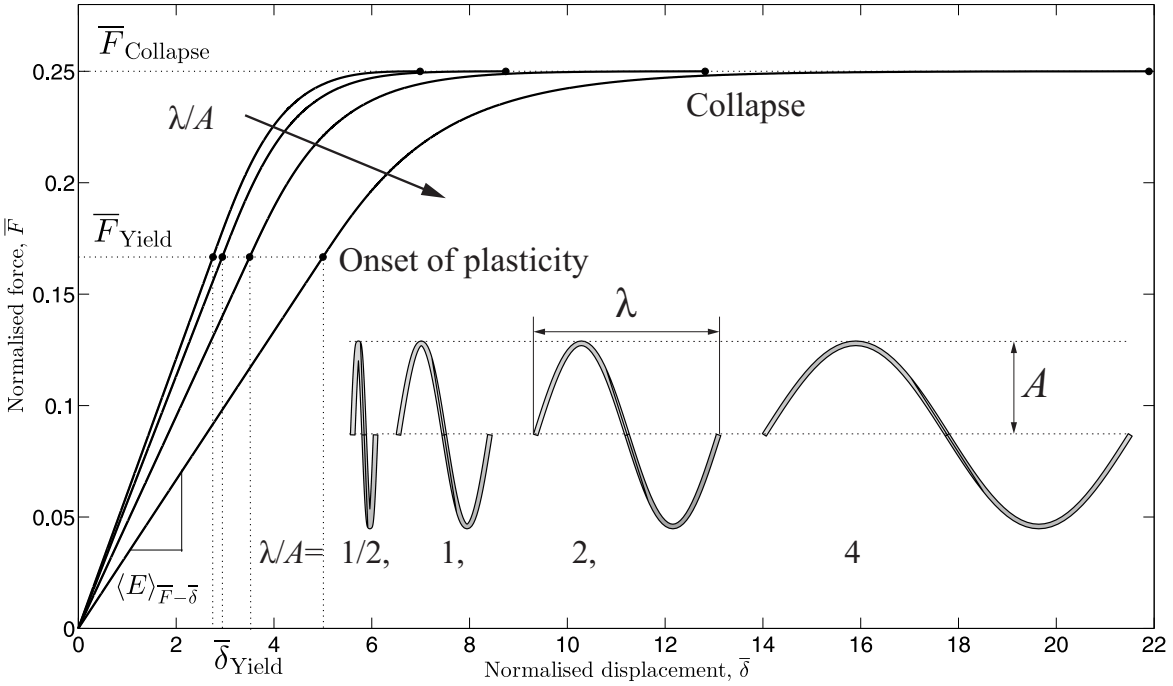

Figure 5.6: Plot of the non-dimensional force $\overline{F}$ against the horizontal displacement $\overline{\delta}$ of a sinusoid subjected to horizontal force F. With a suitable scaling of variables, all the $\overline{F}-\overline{\delta}$ relationships collapse to a family of curve dependent on the geometric parameter λ/A. The points $(\overline{F}_{\text{Yield}}, \overline{\delta}_{\text{Yield}})$ correspond to the onset of plasticity, while $\overline{F}_{\text{Collapse}}$ is the collapse force of the sinusoid when the cross-section at the peak is fully plastic.

the blood flow. Therefore, the structure must offer high radial stiffness. The family of 'master-curves' presented in figure 5.6 and equation (5.14) suggest, for the stent application, a design with a small λ/A ratio because a high $\langle E\rangle_{\overline{F}-\overline{\delta}}$ is desired.

In the area of stent implants, the mechanical performances of the devices are often presented in terms of applied pressure and radial expansion. The relation between tensile force F and internal pressure p is given by equation (5.1). The dimensionless functional relationship $\overline{F}-\overline{\delta}$ between force and displacement can be re-written in terms of dimensionless pressure $\overline{p}$ and radial displacement $\overline{\Delta r}$ as

$$\overline{\Delta r} = \frac{\Delta r}{\sigma_y A^2 2\pi/\left(Etn\right)} = f\left(\frac{p}{\sigma_y b t^2 2m/\left(AS_p\right)}, \frac{\lambda}{A}\right), \tag{5.15}$$

where S_p is half of the inner surface of the stent projected on the horizontal plane, as shown in figure 5.3 (a) and (b), m is the number of crowns along the length and n the number of sinusoids around the circumference. The area of a period of the sinusoid can be approximated as the difference between two sinusoids having amplitude equal to $A' = A + t/2$ and $A'' = A - t/2$, and period $\lambda' = \lambda + 2t$ and $\lambda'' = \lambda - 2t$. Considering all n sinusoids and m crowns, including the contribution of the straight bridges and

projecting it on the horizontal surface leads to

$$S_p = \frac{mnt}{\pi}\left(4A + \lambda + h\pi\right)\frac{2}{\pi}, \tag{5.16}$$

where h is half of the length of the straight bridges, n is the number of sinusoids in a crown, m the number of crowns along the length. By renormalising the mechanical response of the stent according to $\overline{\Delta r} = \Delta r/(\sigma_y A^2 2\pi/Etn)$ and $\overline{p} = p/(\sigma_y bt^2 2m/AS_p)$, we obtain the same family of 'master-curves' describing the non-linear elasto-plastic behaviour as function of λ/A plotted in figure 5.6.

The analytical approach developed here affords results for stent expansion. Consider now two novel stent designs that resemble the convex honeycomb and auxetic structures studied above. Their response is now assessed computationally. The results are obtained using ABAQUS, a commercial Finite Element software. The geometry has been meshed using the element type C3D8I (8-node brick element), with average size of 0.01mm– obtained from a mesh convergence study. An ideal elastic-perfectly-plastic material with Young's modulus (E) of 209 GPa and yield stress (σ_y) of 240 MPa has been used. Because of the symmetry of the geometry and the load, only a quarter of the structure has been modelled and symmetry boundary conditions have been applied. The results are plotted in figure 5.7 using the scaled variables presented in equation (5.15).

An overall stiffening of the structure is observed for the auxetic configuration compared to the analytical results, as highlighted for the planar configuration. The effects of curvature have been already assessed in a previous section. This discrepancy can be further attributed to the shear stress within the crowns, which is ignored in the analysis by assuming the thickness of the sinusoid t much smaller than the amplitude A. However, this condition is not satisfied when the ratio t/A is close to 8. Further, the fact that the stent is a finite structure results in a non-uniform radial expansion of the tube–the so call dog-boning effect. This implies that not all the crowns experience the same state of stress and some of the straight members, those close to the two ends, participate in larger deformation. This is because a stent is axially a finite structure, whereas the analysis is simplified for a single crown that cannot account for such end effects. Note that results for the auxetic configuration differ from the theoretical results more than those for the rolled convex honeycomb configuration. This can be attributed to the extra material in case of the auxetic stents undergoing deformation at the sinusoid peaks and valleys, as shown in the inset of figure 5.7, where the Von Mises stress is plotted. Regarding the convex honeycomb configuration, a good agreement with the analysis in the linear part is observed, whilst a slight structural softening occurs when it undergoes plastic deformation. This can be attributed to the shear stress developed within the crowns and the non-uniform radial expansion. As for the planar configuration, while keeping the ratio λ/A constant, by changing the material parameters and all the remaining geometric parameters, the mechanical response curves collapse onto a single curve. This suggests

that the parametric dependence determined from the scaling analysis is valid also for this class of real structures.

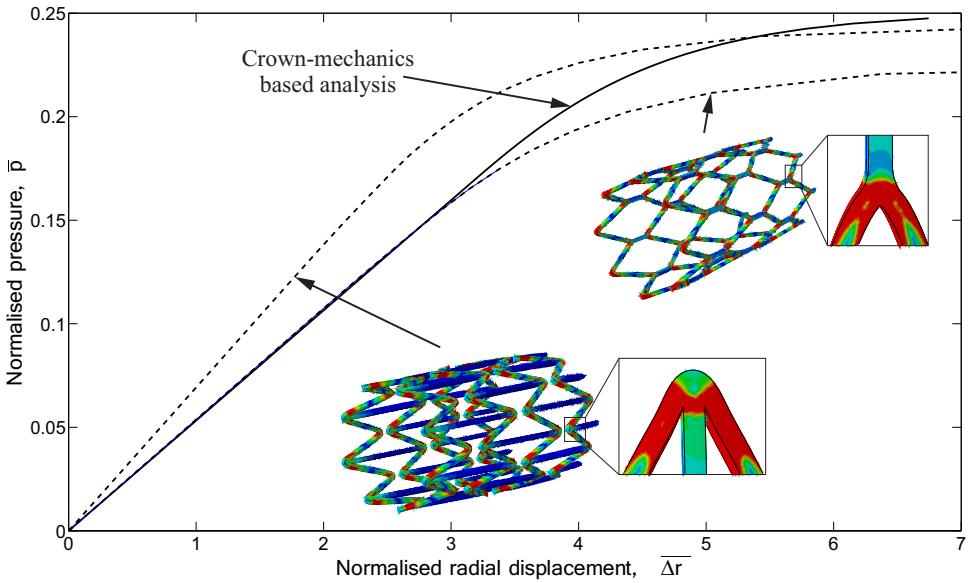

Figure 5.7: Plot of the non-dimensional pressure $\overline{p}$ against the radial displacement $\overline{\Delta r}$ of real stent structures. The solid lines is the results obtained by applying the analytical framework developed here for a flat configuration. The solids lines are receptively the elasto-plastic response of two real stent of radius $r = 3$ mm, having the same sinusoidal parameters ($A = 0.8$ mm, $t = b = 0.1$ mm, $n = 8$ and $m = 8$). Half of the bridge length for the auxetic configuration is $h_{\text{auxetic}} = 1.8$ mm, while for the honeycomb is $h_{\text{honeycomb}} = 0.5$ mm. An ideal elastic-perfectly-plastic constituent material of Young's modulus $E = 209$ GPa and yield stress $\sigma_y = 240$ MPa has been assumed.

Following the successful scaling analysis, we are now in a position to infer the mechanical response of infinite stent designs subjected to internal pressure. The family of 'master-curves' presented in figure 5.6 allows us to identify the approximate response of all the stent designs analytically. Decreasing the λ/A ratio results in a higher stiffness as shown in figure 5.6 and confirmed by equation (5.14), which explicitly shows the inverse relationship. The wavelength λ is directly related to the number of sinusoids along the circumference n as $\lambda = 2\pi r/n$. In order to obtain a stiffer structure, a large number of sinusoids n is required. However, the designer has to account for several other constraints coming from both the crimping and expansion phases. During the crimping phase, the stent profile is reduced and the implant is compressed to a smaller diameter onto the balloon to allow the delivery of the implant through the blood vessels. The self-contact between the struts of the scaffold should be minimised to avoid damage of the material. The final diameter aimed after the crimping procedure sets the maximum number of sinusoids that can fit along the circumference in its pre-crimped configuration in order to avoid struts overlap or contact. This means that a high amplitude A should be preferred to increase the stiffness. However, while increasing A, the total inner surface of

the stent increases according to equation (5.16) resulting in a higher coverage area which is undesirable because it is the major cause of the blood vessel inflammation–known as restenosis. To conclude, the optimal stent is a trade off between high apparent stiffness and minimum coverage area S. The usefulness of the analysis of Chapter 3 becomes evident now. Many generic conclusions with regards to the elasto-plastic behaviour of the real implant bears a strong resemblance with these obtained in case of the hexagonal honeycomb. Indeed, the analytical dependence suggested by the flat honeycomb elasto-plasticity enables us to derive design information when a geometric parameter is altered. This can be extremely useful at early design stages.

5.3 Conclusions

Analytical expressions for elasto-plastic analysis of sinusoidal cylindrical structures were developed. It was shown that the response of the cylinder under internal pressure is well approximated by that of the stretch of its open-up configuration. The lattice response displays a smooth apparent stress-strain relationship even though an elastic-perfectly-plastic constituent material model is assumed. The effects of the curvature, neglected in the analytical model, have been assessed computationally. A scaling ansatz was proposed on the basis of known physics that collapses data in a family of 'master-curves'. From such relationship, it can be seen that the apparent stiffness is proportional to $(A/\lambda)^3$, which is true for all bending-dominated periodic structures. This suggests that the most efficient way to increase the stiffness of the stent is to increase the sinusoid amplitude A. A practical application to stent structures of the analytical framework developed here is then proposed. The usefulness of such analytical approach arises at early stages of design when we are interested in the parametric sensitivity of the stent response, but not in the accurate response calculation. This is well captured by the analysis presented here.

Chapter 6

Development of a novel cardiovascular stent

Coronary artery disease (CAD) is the major cause of mortality within the European Union [131]. The choice of treatment is at doctor discretion due to the influence of several factors, such as the extent of the disease, patients age and presence of other medical conditions. For severe disease, coronary artery bypass graft (CABG) is essential. This invasive surgery requires the implant of a blood vessel taken from the patient's body to pass around the obstruction in order to restore the blood flow. Novel minimal invasive surgical approaches have been developed to overcome the long recovery time and to reduce the risks for the patients. The most significant technical advance in percutaneous coronary interventions is the establishment of the angioplasty technique, a procedure during which a narrowed blood vessel is widened using a balloon that presses the plaque against the artery wall. In several cases, after the angioplasty, a stent is placed in the blood vessel in order to provide scaffolding and to prevent the re-narrowing of the artery.

Currently, three types of stents are used to treat cardiovascular diseases. The most common types are Bare Metallic Stent (BMS) and Drug Eluting Stent (DES). They are commonly made of 316L stainless steel or chromium-cobalt alloy. Once implanted, they permanently stay in the patients' body. This often leads to chronic inflammation of the artery, in-stent restenosis, thrombosis and stent jailing. Moreover, they present a difficulty for future cardiac interventions at the same location due to the presence of a previous implant. This has opened up the market for biodegradable polymeric stents such as those made of poly-glycolic acid (PGA) and poly-L-lactic acid (PLLA). On the market, there is only one FDA[1] approved stent, manufactured by Abbott–the lead USA company. However, it expands only up to 3 mm diameter since failure of the structure is

[1]Food & Drug Administration (FDA) is responsible for protecting the public health by assuring the safety, efficacy and security of human and veterinary drugs, biological products, medical devices [132].

observed when inflated over 3.5-4 mm diameter. Moreover, it is not suitable for calcified lesions because of its lower radial strength compared to metal stents [133]. Finally, extensive training is required for the cardiologist in order to prevent fractures during the deployment and its cost makes it inaccessible for most hospitals compared to the cheaper metallic options. The work presented in this chapter has been developed as part of the FP7 project ReBioStent, whose main aim is the development of biodegradable and biocompatible resorbable stents using highly innovative materials.

In this chapter, two preliminary stent prototypes for cardiovascular application are presented. The aim is to predict the response of such devices during its installation on the deployment catheter and the expansion at the injured area for a future optimisation study. A flexible geometry generator is presented first, followed by the numerical modelling. The complexity of the system and the large number of uncertainties in biomedical systems makes the analytical prediction of its exact mechanical response challenging. Therefore, numerical modelling using finite element analysis is an indispensable tool for the design process. Preliminary trial tests and comparison with numerical simulations are presented.

6.1 Methodology

A finite element analysis usually requires the definition of the geometry, material properties and specific numerical aspects, i.e. applied load, boundary conditions and numerical solver. These properties and the numerical parameters used to simulate the crimping and expansion of the novel stents are described next.

6.1.1 Geometry creation and parameterisation

The modelling process starts with a parametric Computer Aided Design (CAD) drawing of the flat-sheet pattern. For this purpose, Rhinoceros 5 (Robert McNeel & Associates) has been used–a NURBS-based CAD software. The need of obtaining freely adjustable and mathematically accurate geometries has driven our choice to the use of Bézier splines, which are a subset of NURBS curves. It allows us to create precise geometries and to generate easily a family of designs by making use of a Python script that can tailor the geometric parameters.

By using the model of a generic sinusoidal structure presented in the previous chapter, a novel axially extending, or *auxetic*, stent is introduced. A single cell has been parametrised and copied along the fundamental lattice directions unchanged in a flat configuration. The parameterisation of the unit cell is shown in figure 6.1 (a). As ascertained in the previous chapter (see figure 5.7), the extra material located at the peaks and valleys of the sinusoidal crowns does not fully participate to the deformation. In

order enhance the spread of the plastic deformation within the structure, some material at these critical locations is removed. This is, in practice, controlled by the fillet radius R_2, shown in figure 6.1 (a). In contrast with the analyses performed in the previous chapters, the structure here considered has a finite length; therefore, the boundary effects cannot be ignored. The stiffness of the two extreme crowns of the stent plays a significant role during the expansion of the implant. Therefore, an additional parameter R_3 (see figure 6.1 b) has been introduced to control the amount of material at the sinusoid extreme, where no bridges are connected, at the last two crowns.

By coping the unit cell along two principal directions in a plane, the stent geometry in its unrolled configuration is obtained (figure 6.1 b). A closed network of poly-lines thus obtained is converted into a surface later, and further extruded to a height equal to t, as shown in figure 6.1 (c). Finally, the flat structure is wrapped around a cylinder of diameter D to obtain the stent in its final configuration, as shown in figure 6.1 (d). The diameter is measured from the inner surface of the stent and it is referred to as inner diameter (ID). By using the parameterisation presented above, infinite number of cell geometries can be generated. The selected geometries were then used for cutting polymer tubes to manufacture the stents. The manufacturing task was carried out by an external organisation (TEKNIKER, a partner within the collaborative project ReBioStent). A laser cut stent prototype is shown in figure 6.1 (e).

The use of axially extending stents–thus showing an *auxetic* behaviour–decreases the risk of mal-positioning of the implant during the expansion. A length longer than its deployment size can be covered; therefore, the target plaque can be fully treated by deploying only one implant. Auxetic stents can achieve a good grip with the surrounding tissue by embedding inside the tissue during the elongation. This can largely reduce the problem of the migration of the implant [134]. Furthermore, the device that has to be delivered through the blood vessels has a smaller length and this might facilitate the angioplasty procedure. Currently, no evidence to prove or reflect this insight are available; however, *in vivo* testing performed during the project will provide more information on this novel aspect.

The treatment of a plaque near a bifurcation by an axially extending stent could jut and obstruct the flow in the side vein [135], causing flow separation and increase in the shear stress on the wall of the blood vessel [136]. Considering this possible scenario, a new configuration exhibiting axial shortening during the expansion is proposed here. The novel shape is obtained from the previous configuration by altering the connectivity between the crown and the bridges, according to the discussion presented in Chapter 5. The unit cell parameters are shown in figure 6.2 (a and b), together with the first prototype obtained from laser cutting performed at TEKNIKER (see figure 6.2 c).

As designers, we do not have a free choice on all the stent parameters, as some are imposed by the manufacturing considerations. The structure was cut using the laser

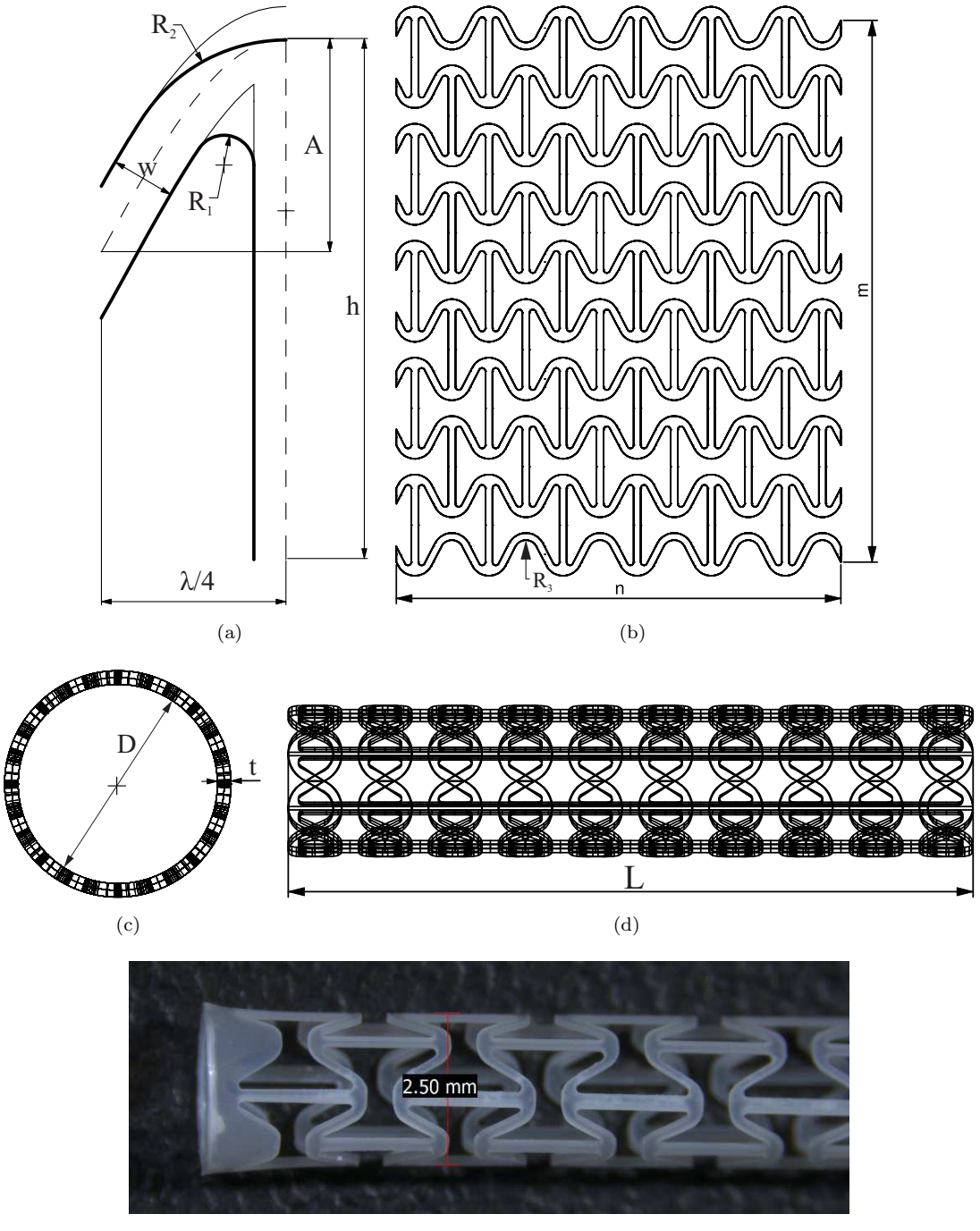

Figure 6.1: (a) Geometrical parameters used to describe the unit cell. (b) The flat configuration of the stent is obtained by coping the unit cell n-times along the horizontal direction and m-times along the vertical direction. (c) Fixed the inner stent diameter D and the number of cells along the circumference n, the wave length of each unit cell λ is calculated. The thickness of the stent is measured by t. (d) Cylindrical stent configuration obtained after wrapping the flat geometry around a cylinder, where L is its total length. (e) First stent prototype manufactured using laser cut (with the courtesy of TEKNIKER).

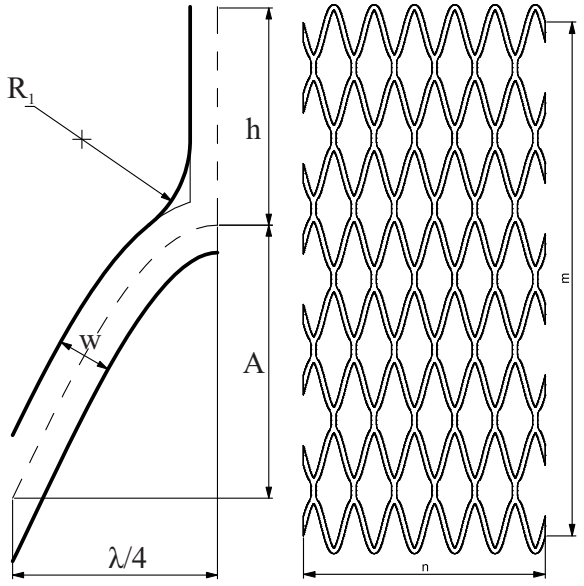

(a) (b)

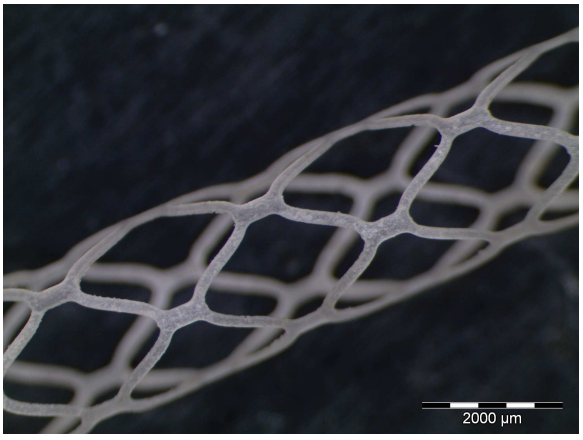

(c)

Figure 6.2: (a) Geometrical parameters used to describe the unit cell of the *convex honeycomb* configuration. (b) The flat configuration of the stent is obtained by coping the unit cell n-times along the horizontal direction and m-times along the vertical direction. (c) First stent prototype manufactured using laser cut (with the courtesy of TEKNIKER).

from an extruded tube. Therefore, the diameter of the tube and its thickness will determine those of the implant. The two stent competitors currently on the market are Absorb, coming from Abbott, and DESolve, from Elixir. Their main characteristics and geometric features are summarised in table 6.1. Motivated by the need to introduce on the market a new competitive device and after the consultation with well-known European cardiologists, it has been decided to aim for a stent with an outer diameter (OD) of 2.5 mm and strut thickness of 150 μm. Smaller devices are frequently desired by surgeons in order to treat patients with smaller arteries (e.g. young patients) and for non-cardiovascular applications, such as the treatment of brain aneurysms. This has

further driven the choice of the project consortium towards the design of a device with a small diameter.

Table 6.1: Features of the only two biodegradable stents currently on the market.

Property	**DESolve** [98]	**Absorb** [97]
	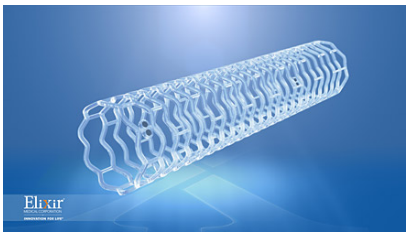	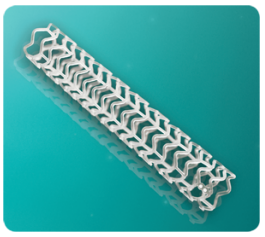
Backbone	PLLA	PLLA
Design	Tubulary hoops and bridges	In-phase zig-zag hoops and bridges
Struts thickness	150 μm	150 μm
Diameter	2.5, 3.0, 3.25, 3.5 mm	2.5, 3.0, 3.5 mm
Length	14, 18, 28 mm	8, 12, 18, 23, 28 mm

The models so far created correspond to the stent as obtained after the laser cut. It represents the implant in its pre-crimped state. It is commonly referred to this configuration as *nominal* geometry. To deploy the stent to the blocked area of an artery, at first, the device must be firmly crimped on a balloon, which is attached at the end of a catheter that will be inserted through the groin of the patient to reach the injured artery area. The stent diameter must be reduced to allow the deployment of the implant through the blood vessels, which have an average diameter of 3.5-4.0 mm [137]. During the crimping process, the stent is plastically deformed so that it permanently stays on the balloon. When the stent-balloon system is removed from the crimping machine, the structure will springback because of the recovery of the elastic deformation. To counteract the elastic recoil, the stent is subjected to a heat treatment. This will also remove the residual stresses from the structure. When the blocked area is reached, the balloon is inflated and the scaffold is permanently placed inside the blood vessel by once more plastically deform the stent. Numerical simulations are performed here to mimic both the crimping and the free expansion procedures of the stent.

6.1.2 Material composition of the stent

Most of the stents on the market are bare metallic or drug-eluting made of 316L Stainless steel. Because of the risks of long-term implantation, biodegradable stents are now under development. The RebioStent consortium has developed two novel bioresorbable

materials using novel synthetic and natural biodegradable polymers: modified synthetic PLLA-co-PEG produced using a supercritical CO_2 method and natural Polyhydroxyalkanoates (PHAs) produced via bacterial fermentation. To improve the mechanical properties, inorganic fillers (phosphate nano-bioglass) have been added. Antiproliferative drug to provide controlled drug delivery has been incorporated using mesoporous silicate bioabsorbable glass and PHA nanospheres.

In general, the developed materials show a relative low Young's modulus (ranging between 0.5-1.8 GPa at room temperature) and maximum stress (between 30-50 MPa) compared to the basic structural metal materials employed for BMS and DES implants. Despite the low radial stiffness related to the low Young's modulus that must be compensated with novel design features, the two materials show a really elastomeric behaviour, thus the strain at the breaking point reaches 800%-1000%. Allowing large deformations before reaching the collapse clearly prevents a sudden fracture of the stent struts, a common problem observed in Abbott stent during implantation because of the brittle behaviour of PLLA [133]. More detailed information regarding the selected materials cannot be disclosed here because of the confidentiality issue.

6.1.3 The finite element mesh

A crucial aspect in the FEM analysis is the element choice. The computational efficiency and the accuracy of the results obtained using different elements types in the context of stent mechanics have been studied by Hall *et al.* [138]. In the work, they considered solid, shell and beam elements. Hall *et al.* showed that all the elements give similar results even despite the high discrepancy in computational cost due to the large difference in the dimensionality. Surprisingly, the beam element nearly predicts the overall stent response, despite its simple formulation. However, a variation can be found in the extreme values of stress, strain and equivalent plastic strain. Therefore, in this chapter, three-dimensionality of the state of stress will be accounted for. The solid element has been selected to carry out the analysis. The stent structures were meshed using a linear 4-node tetrahedral element (C3D4) available in Abaqus® 6.13, as shown in figure 6.3.

6.1.4 Structural modelling using finite elements

The simulations presented in this chapter are performed using Abaqus/Explicit 6.13.1 (Dassault Systems Simulia Corp., Providence, RI, USA), a commercial finite element solver. The Explicit module has been chosen in order to capture the immediate elastic recoil occurring when the balloon is deflated. The simulation is divided into two steps: crimping of the stent followed by the free expansion–thus the resistance of the plaque and artery are not taken into consideration. All the data of commercial stents provided by the manufacturers refers to the free-expansion performance of the stents. Although

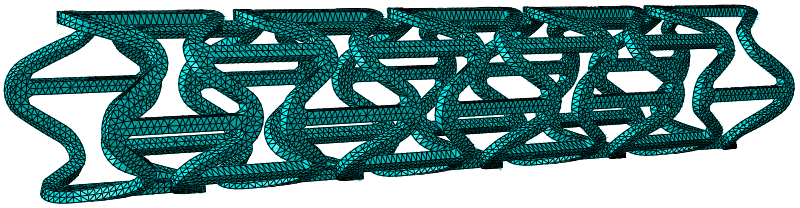

(a)

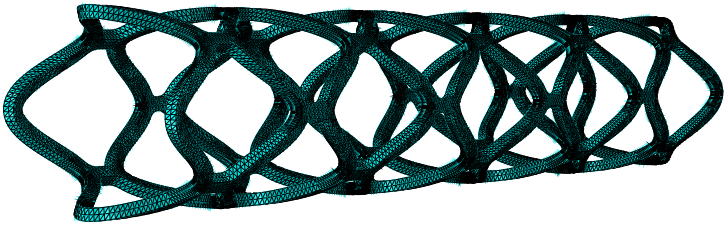

(b)

Figure 6.3: Nominal stent geometries (a) auxetic (b) convex honeycomb, before the crimping procedure, modelled using solid elements (C3D4).

the external environment has a high influence on the stent performance, during the preliminary design stage, the attention is mainly focused on the mechanical response of the implant because it is computationally cheaper. The following two sections describe the methodology adopted for the mechanical characterisation of the stent.

6.1.4.1 Crimping

During the surgery, the deployment of the stent is performed using a catheter with an inflatable balloon at one end on which the stent is mounted in a crimped state. The crimping tool firmly fixes the stent onto the balloon to avoid any movement or slippage during the advancement of the catheter inside the patient's blood vessels from the groin to the blocked area of the artery. The crimped diameter along the stent length must be constant and the cross-section must remain circular; therefore, a uniform pressure is applied along the entire length and the circumference of the stent. The most common equipment adopted for this purpose is a mechanism that applies a constant radial force using 12 rigid planes. An image of a specific of such machine is shown in figure 6.4 (a). During the crimping procedure, the stent undergoes plastic deformation so that it is firmly mounted on the balloon. Once the load is removed, the deformation on the device attributed to the elastic strain is immediately recovered resulting in a final diameter that is larger than the one applied with the crimping mechanism. Recently, to avoid this undesired effect, the stent is subjected to a heat treatment at the end of the crimping procedure. It can be therefore assumed that the stent in the crimped configuration is stress free and the final shape corresponds to the one imposed with the crimping device.

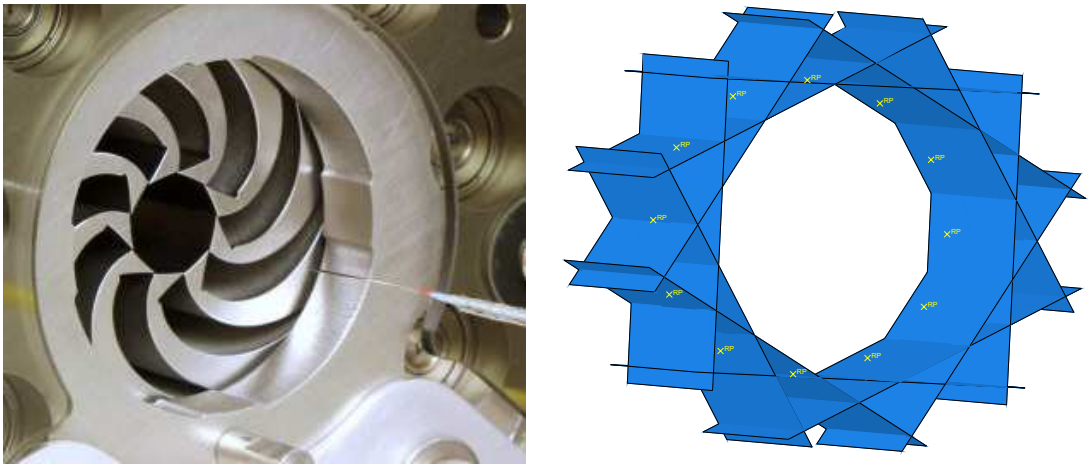

(a) (b)

Figure 6.4: (a) Crimping technologies for stent (Blockwise, 2-CrimpTM [139]). (b) Twelve rigid planes whose motion is related to that of a single node known as rigid body reference node (RP in the figure). The radial motion is assigned to the reference nodes through the boundary conditions.

The crimping process is simulated computationally using FEM. In order to closely resemble the real procedure in the simulation, the crimping tool is modelled using 12 planes defined in Abaqus as rigid surfaces (figure 6.4 b). The motion of these planes is controlled by that of a single node, called rigid body reference node [140]. A displacement boundary condition was enforced to the reference node of each rigid plane in the radial direction. Since crimping is not influenced by inertia effects because internal forces are low as the process is not high velocity, it can be modelled using a quasi-static Abaqus/-Explicit procedure [110]. In quasi-static analyses, it is recommended that the kinetic energy does not exceed 5% of the total energy [140]. Given that the crimping process is not completely static, this appears reasonable. The load was smoothly applied to the structure and the rate was appropriately chosen so that the condition on the kinetic energy is met. The magnitude of the radial displacement was increased accordingly to the graph shown in figure 6.5 (a). The analysis is performed under displacement control conditions. In order to achieve a final diameter of 1.2 mm, a maximum radial displacement of 0.65 mm is applied. The contact within the stent and the rigid planes was modelled as 'hard' contact in order to avoid the penetration of the slave surfaces (the stent) into the master surfaces (the rigid planes). Likewise, strut-to-strut self-contact was taken into account by using a surface-to-surface 'hard' contact. To avoid any rigid body motion of the stent during the simulation [113], symmetry boundary conditions were applied to three nodes along each symmetry plane of the stent model.

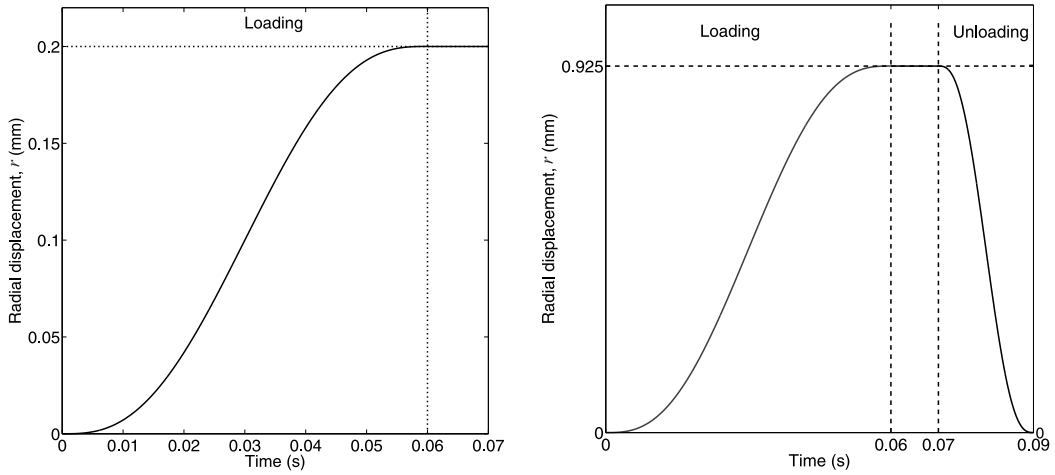

(a) (b)

Figure 6.5: (a) Loading profile for the crimping process of the stent. (b) Loading profile for the free expansion of balloon. The left y-axis refers to the stent expansion with a cylindrical surface subjected to radial displacement, the right y-axis to the expansion with a pressure applied to the inner surface of the simplified balloon.

6.1.4.2 Free expansion in the absence of external blood vessel

In this work, a novel stent geometry is developed. Firstly, it is fundamental to compare the stent performances with that of the implants available on the market. Manufacturers of competing devices provide measurements of the stent performance when the stent is freely expanded–thus the artery and plaque are not included in the information available. Therefore, the numerical simulations for free expansions are performed here in order to compare results with those available for similar products. Three possible scenarios can be adopted to mimic the free expansion of the stent: (i) uniform pressure directly applied on the stent inner surface while completely ignoring the balloon, (ii) accounting for the stent-balloon interaction and enforcing a radial displacement on a cylindrical balloon modelled as a surface, (iii) accounting for stent-balloon interaction and applying an increasing pressure on the inner surface of a trifolded balloon.

In the last 15 years or so, engineers have studied the bio-mechanical behaviour of metallic coronary stents to better understand the mechanical response of these devices when freely expanded. From the data available in literature, the balloon is more flexible compared to a metallic stent. Therefore, it is reasonable to neglect the stiffness of the balloon [104]. This has allowed to discard the presence of the balloon in the analysis and directly apply the pressure on the inner surface of the stent–which corresponds to the scenario (i). With the advent of bioresorbable stents, this condition of dominant stiffness of the stent over that of the balloon is not satisfied any more. The stent and

the balloon have comparable stiffness; therefore, the balloon structure also needs to be kept as a part of the simulation.

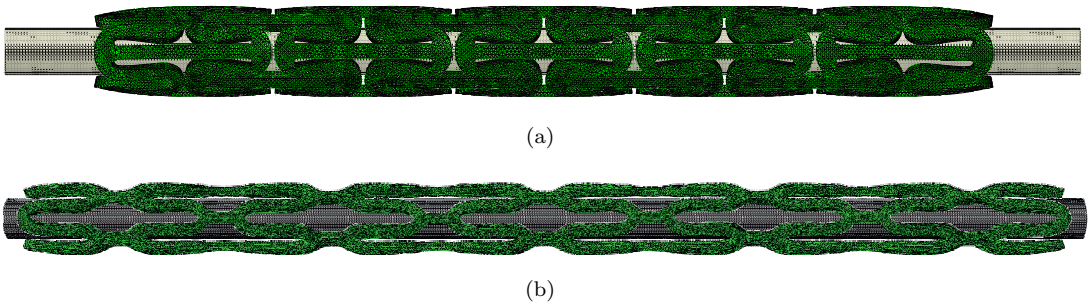

(a)

(b)

Figure 6.6: Finite element mesh of the stent-balloon assemblies to perform the displacement-driven free expansions, for both the (a) auxetic and (b) convex honeycomb topologies.

During the initial design phase of a new stent, the engineer is mainly interested in the global stent behaviour, i.e. the final shape of the stent after expansion and the maximum strain, which has to be below the failure strain of the constituent material of the stent struts. The use of a displacement-driven cylindrical surface to model the balloon expansion provides relatively accurate information regarding the stent shape, stress and strain within the struts at the end of the deployment. Therefore, the second scenario is the best choice since it is significantly less expensive in terms of computational resources than the third scenario [110] while providing all the important information.

For this simulation, the stent configuration resulting from the above crimping step is positioned midway onto a cylinder, which resembles the balloon. After the heat treatment, the stent is stress-free; therefore, the residual stresses can be set to zero. The practical interest is only in the shape of the implant after crimping; therefore, the final deformed geometry obtained before is imported as "orphan mesh"–the geometry is only defined by element and node information, no parts, lines or areas exist in the model. The balloon material is represented approximately by an elastic model, characterized by a Young's modulus of 920 MPa and a Poisson's ratio of 0.4. The material density of the balloon is taken as 1100 kg/m^3 [110]. Density is used in the simulation only to ensure quasi-static analysis. In order to avoid any rigid body motion, three nodes at the central axial cross-section of the stent and the balloon are constrained to move only in the radial direction.

The stent is expanded by applying a radial displacement to the cylindrical surface, which is modelled as a membrane (element type M3D4R–4-node quadrilateral membrane) of thickness 0.02 mm. The length of the balloon for the *auxetic* topology is 3 mm longer than that of the stent in its crimped configuration because its axial length will increase during the expansion. The balloon has been protruded only 0.3 mm axially for the *convex honeycomb* topology because during the expansion the stent will shorten along its length. Surface-to-surface contact was used to model balloon-stent contact interaction, using a

friction coefficient of 0.2 [110]. The finite element model for the balloon-stent system is shown in figure 6.6.

In clinical practice, inertia has a negligible effect on the expansion process; therefore, the deployment of the stent can be modelled as quasi-static by using Abaqus/Explicit [110]. During the balloon inflation, the pressure is slowly applied until the scaffold is completely expanded. Prior to deflation, the pressure is maintained at its peak value for few seconds to avoid the propagation of vibrations into the structure. In order to faithfully simulate the stenting procedure and to bound the kinetic energy of the system– as done for the crimping simulation, the radial displacement of the balloon is applied smoothly according to the graph shown in figure 6.5 (b).

6.2 Results and Discussion

In this section, the structural response of the novel stents is systematically presented and analysed. The stent structure is first crimped from its nominal shape onto an inflatable folded balloon attached at the end of a catheter using radial compression of twelve rigid planes. From this configuration, the stent is expanded by applying a uniform radial displacement via the use of a cylindrical surface placed internally.

At first, a mesh sensitivity study was performed for the *auxetic* stent to establish the required number of elements and time-step. Table 6.2 shows the combinations of different mesh sizes and time-steps used for the crimping analysis of the *auxetic* prototype. The results of the simulations (axial shortening and maximum stress close to the peak of the sinusoid), obtained for increasingly finer mesh (see figure 6.7 a) and smaller time-step (see figure 6.7 b), have been compared until no significant changes were observed and convergence established. A stent mesh of 220.000 elements (element size 0.055 mm) and time-step of 1×10^{-7} s were found to give accurate results. Smaller time-steps increase the accuracy of the results by 0.6%, but the physical simulation time increases up to almost 5 days for a time-step of 1×10^{-9} s–compared to 4 hours for the chosen time-step. Based on this observation and found that the ratio of kinetic energy to total internal energy remains below 5%, a time-step of 1×10^{-7} s is used for subsequent studies. The same parameters have been used for the expansion simulation of this topology and for the crimping and expansion of the *convex honeycomb* stent.

6.2.1 Crimping

During the crimping process, the stent is radially compressed from its nominal outer diameter of 2.5 mm to 1.2 mm. The scaffold undergoes large irreversible plastic deformation so that it is firmly fixed onto the deployment device, called the catheter. The two final crimped configurations are compared in figure 6.6. Note that the *auxetic* topology

Table 6.2: Different mesh and time-steps used for the convergence study

Mesh	**Element size**	**Number of elements**	**Time step**
Mesh 01	0.200	7621	1.00E-07
Mesh 02	0.150	14995	1.00E-07
Mesh 03	0.120	27247	1.00E-07
Mesh 04	0.100	46348	1.00E-07
Mesh 05	0.080	80136	1.00E-07
Mesh 06	0.070	125411	1.00E-07
Mesh 07	0.060	186710	1.00E-07
Mesh 08	0.055	228750	1.00E-07
Mesh 08-01	0.055	228750	5.00E-07
Mesh 08-02	0.055	228750	1.00E-07
Mesh 08-03	0.055	228750	5.00E-08
Mesh 08-04	0.055	228750	1.00E-08
Mesh 08-05	0.055	228750	1.00E-09
Mesh 09	0.050	368248	1.00E-07
Mesh 10	0.045	414930	1.00E-07

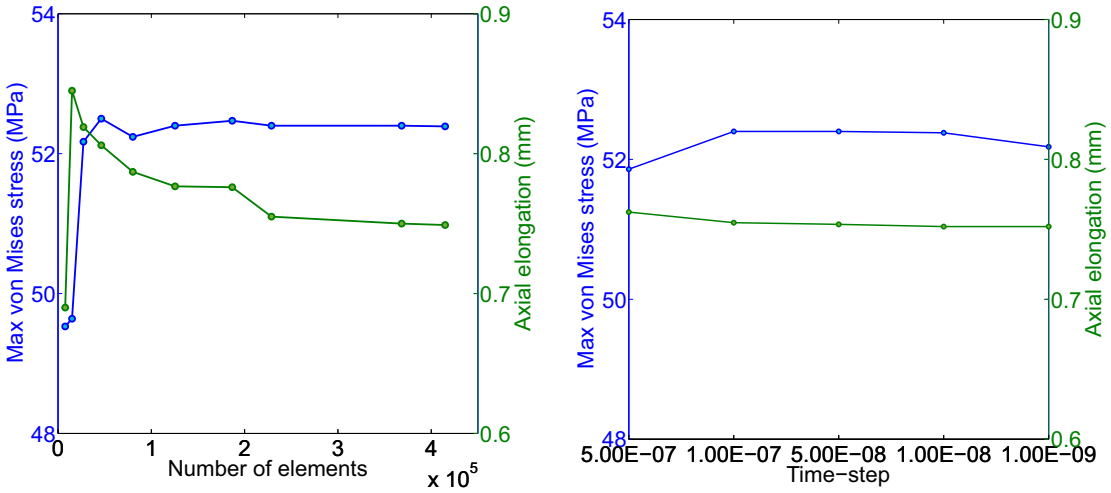

(a) (b)

Figure 6.7: Maximum von Mises stress and axial elongation during crimping for different (a) number of elements (time-step kept constant at 1.00E-07) and (b) time-steps (using the chosen element size that showed convergence–0.055).

is much shorter than the *convex honeycombs* stent. Future clinical studies will provide valuable insight into the possible advantages of a shorter device during the deployment.

The preliminary crimp analysis provides the stent's initial shape before the expansion inside the patient. Self-contact between stent crowns and bridges is avoided during the crimping procedure to prohibit damage or deformation of the struts. In the novel stent geometries considered here, because of the thicker struts (150 μm) compare to metallic stents (80-100 μm) required to compensate the poorer mechanical properties of biodegradable polymers, self-contact occurs during the crimping of the *auxetic* topology

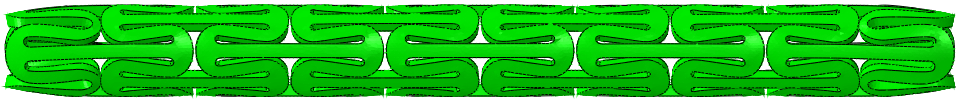

(a)

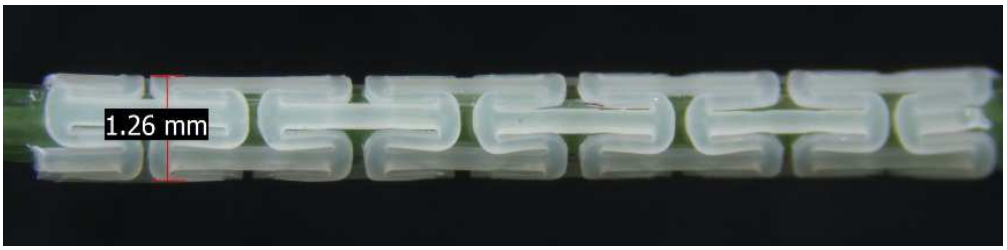

(b)

Figure 6.8: Final crimped configuration of the novel auxetic stent geometry obtained (a) using numerical modelling and (b) from a preliminary trial investigation at room temperature (with courtesy of Arterious).

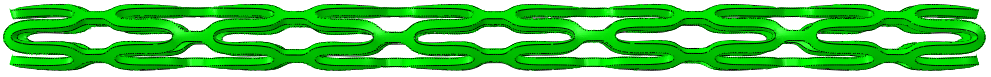

(a)

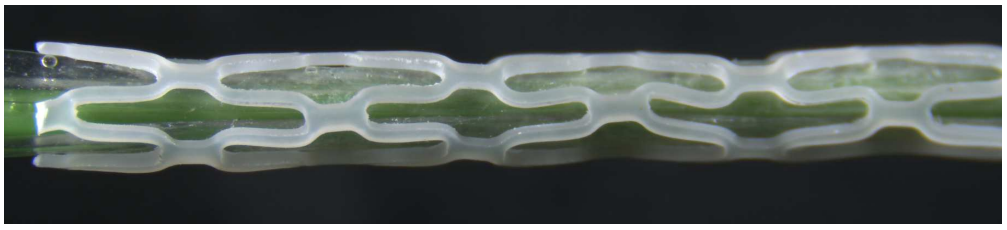

(b)

Figure 6.9: Final crimped configuration of the novel convex honeycomb stent geometry obtained (a) using numerical modelling and (b) from a preliminary trial investigation at room temperature (with courtesy of Arterious).

(see figure 6.6 a). This is also observed in one of the competitor biodegradable stent on the market Absorb BVS [141]–no information regarding the crimping quality is available for DESolve. This is a reflection of the demand on the mechanical performance from structures made of poorer material. The poor material properties of polymers are compensated by the superior performance due to biodegradability.

The preliminary trial investigation of laser cut ReBioStent prototypes was performed using the MSI Crimper, onto CNovate Medical Helix 2.5 20 mm balloon catheters by Arterious–a UK company working in the development of coronary stents. The crimp procedure has been performed at room temperature imposing a final diameter of 1.2 mm with 30 s hold time and at 50°C. Because of the high temperature, the polymers melted, resulting in uneven crimped profiles. Further optimisation of such process is in progress.

Images of the *auxetic* and *convex honeycomb* scaffolds in their crimped configurations at room temperature are respectively shown in figures 6.8 and 6.9, where the final shapes obtained from the numerical analysis (figure 6.8 a and 6.9 a) are compared to the final shapes of the real prototype (figure 6.8 b and 6.9 b respectively). Both numerical and trial test are in a good agreement. A homogeneous crimped diameter is obtained and no fracture of the struts has been recorded. Because of manufacturing limitations, the laser cut was initially programmed only to cut the main body of the stent. The two ends were therefore incomplete (see figures 6.8 and 6.9). This imperfection caused the slight difference in the deformed shapes at the edges of the stents.

6.2.2 Free expansion of the stent

Balloon expandable stents are crimped from their manufactured configuration (nominal geometry) over a catheter for the deployment to the injured area. The shape resulting from the previous analysis is now incorporated with a simplified balloon and subjected to the free expansion by imposing a radial displacement through the cylindrical surface. Since the device is subjected to a heat treatment at the end of the crimping procedure, the crimped configuration on the balloon can be assumed to be stress-free. Therefore, our interest of the crimping simulation lies only in the final shape of the implant and not on the internal residual stresses of the structure.

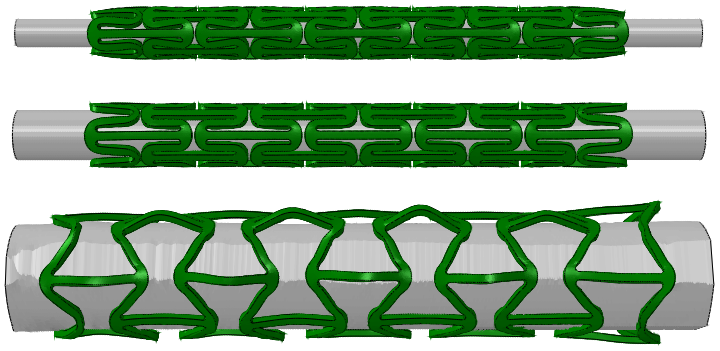

(a)

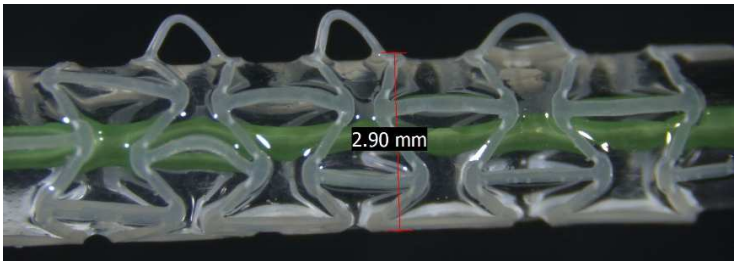

(b)

Figure 6.10: Final expanded configuration of the novel auxetic geometry obtained using numerical modelling and (b) from a preliminary trial investigation [142].

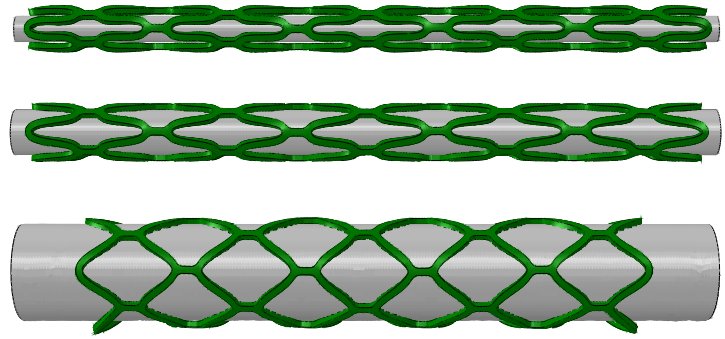

(a)

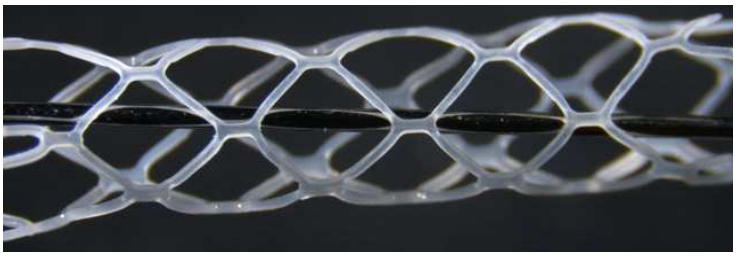

(b)

Figure 6.11: Final expanded configuration of the novel convex honeycomb stent geometry obtained using numerical modelling and (b) from a preliminary trial investigation [142].

Our attention is focused on the global behaviour of the implant. The stent deployment pattern for preliminary *convex honeycomb* and *auxetic* geometries prior to, during and after the expansion are presented respectively in figure 6.10 and 6.11. During the expansion phase, the *auxetic* topology shows some straight bridges curved outwards (see figure 6.10 a). This unstable behaviour has been clearly highlighted by both simulations and initial trial tests. The instability was caused by a boundary effect since the structured analysed here is not infinite–as assumed in the previous chapters, but it has a fixed length. Stiffer end crowns resolves the instability behaviour. To overcome such a problem, the end crowns were designed as being different from all the others along the length. They are stiffened by reducing the fillet radius R_3 shown in figure 6.1 (b). Preliminary trial tests on the new topology have not been performed yet. Numerical simulations shown an expanded final shape to be uniform where none of the bridges loops out radially (see the final deformed shape in figure 6.12). By contrast, the stent shape of the *convex honeycomb* topology when its nominal diameter is reached does not present any distorted members or instability behaviour, e.g. buckling of the straight bridges. This is observed in both computational results and trial investigation, which show a good agreement in the final deployed shape. Hence, it can be said that this initial design offers a good starting point and promising prospects.

The Von-Mises stress and the maximum plastic strain resulting from the displacement-driven cylindrical balloon expansion method for the two novel topologies are depicted

in figure 6.12 and 6.13. The plastic strain, designated in the commercial finite element program Abaqus as PEEQ, measures the amount of plastic deformation remaining within the stent [143]. The value of this parameter shows the locations where failure is most likely to occur [144]. The maximum stress, as well as the maximum plastic strain, are located at the curved section of the rings. These areas are highly critical for the integrity of the structure, as predicted from the analysis presented in the previous chapter. As extensively demonstrated in the previous chapter, the structural response of the stent is mainly dictated by that of the circumferential rings. By contrast, the bridges do not play a significant role during the expansion, but their primary task is to provide flexibility during the deployment.

The simulation does not include any failure criterion; therefore, it is important to assess the structural integrity. Although the maximum stress exceed the failure stress of the material, it can be safely said that the stent would not fail during the expansion since the material stress-strain curve continues well beyond the strain corresponding to the maximum allowable stress–in fact, the material shows a highly elastomeric behaviour.

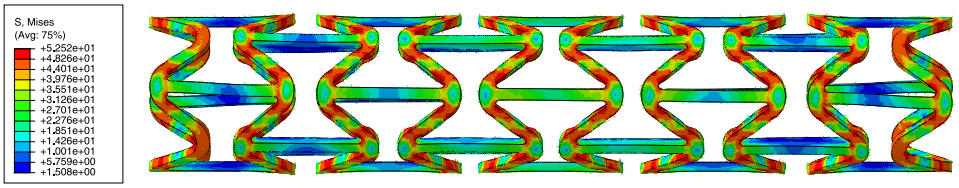

(a)

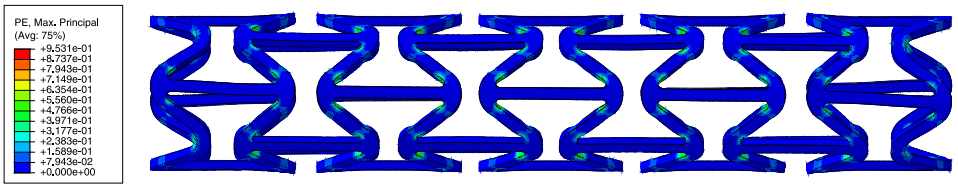

(b)

Figure 6.12: Final crimped configuration of the novel convex honeycomb stent geometry obtained (a) using numerical modelling and (b) from a preliminary trial investigation.

A trial investigation of the laser cut stents has been performed to assess the quality and performance of the novel geometries under expansion conditions. The stent was expanded using an inflatable balloon to reach an inner diameter (ID) of 2.5 mm. At the point of maximum expansion, images were taken (see figure 6.11 b and figure 6.10 b) to compare with the numerical results obtained during the design phase. None of the struts breaks during the expansion for none of the two topologies. However, as observed during the simulations, on the expansion of the first *auxetic* design, some connectors loop radially (figure 6.10). The balloon catheter was deflated and removed. Images of the stents were taken after the elastic deformation was recovered.

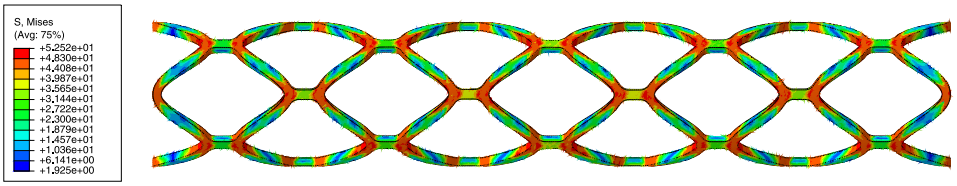

(a)

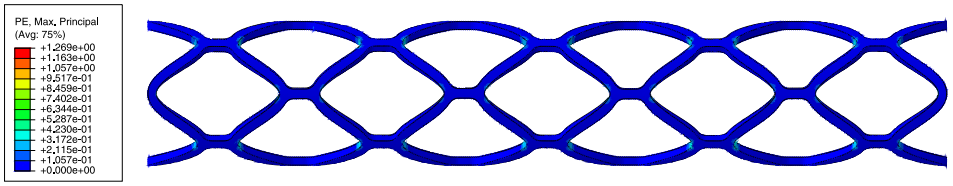

(b)

Figure 6.13: Final crimped configuration of the novel convex honeycomb stent geometry obtained (a) using numerical modelling and (b) from a preliminary trial investigation.

One of the most important parameter commonly used to measure stents performance is its immediate radial recoil, R_c, given by

$$R_c = \left(R^{\text{load}}_{\text{central}} - R^{\text{unload}}_{\text{central}}\right) / R^{\text{load}}_{\text{central}}, \tag{6.1}$$

where $R^{\text{load}}_{\text{central}}$ and $R^{\text{unload}}_{\text{central}}$ are the radius of the stent at the central section after the load is applied and when the load is removed, respectively. When expanded, the stent obtained using the *convex honeycomb* topology shortens in the longitudinal direction. This phenomenon is called foreshortening (FS) and it is defined as

$$FS = \left(L_{\text{initial}} - L_{\text{final}}\right) / L_{\text{initial}}, \tag{6.2}$$

where L_{initial} and L_{final} are the initial and final lengths of the stent, respectively. Note that, during expansion, the *auxetic* topology elongates in the longitudinal direction; therefore, such phenomenon does not occur.

Recoil and foreshortening were calculated during the trials for the novel stent prototypes for the two selected materials, one synthetic and one natural, and the results are presented in table 6.3. We refer to the two materials as $S2$ and $N1$ because the composition cannot be disclosed here due to confidentiality[2]. A competitor bioresorbable stent Absorb, available on the market, shows a recoil of 10% [141]. Both prototypes made of the synthetic biodegradable S2 material show a recoil well below that of Absorb. This shows great potential for future commercialization. By contrast, the prototypes made of the natural material N1 possess a high radial elastic recoil. This material follows a non-linear path when unloaded; therefore, most of the deformation is recovered when the internal pressure is removed. The foreshortening of most of the stents on the market

[2]IP protection in progress for the composition of $S2$ and $N1$ materials.

Table 6.3: Performances of stent prototypes when expanded to different final diameters.

Design		**Recoil**			**Foreshortening**
		2.5mm	**3.0mm**	**3.5mm**	**2.5mm**
Honeycomb	**S2**	1.4%	-	-	6.8%
	N1	11.7%	-	-	10%
Auxetic	**S2**	1.2%	1.3%	0.7%	-9.9%
	N1	9.2%	15.5%	16.1%	-0.9%

Table 6.4: Performances of stent prototypes when expanded to different final diameters.

Design	**Area (mm^2)**	
	2.5mm	**3.0mm**
Honeycomb	118	127
Auxetic	81	86

is around 6-8%. The *convex honeycomb* geometry is well within such range for the S2 material, whilst N1 shows a slightly higher shortening still related to the high elastic recoil. By contrast, the *auxetic* topology shows an elongation during the expansion, resulting in a *negative* foreshortening.

The contact area between stent and artery is one of the cause of late restenosis–reclosure of the blood vessel due to an inflammatory reaction three to six months after the surgery. A smaller contact area reduces the risk of such long-term side effect. Stent currently on the market have a total surface area of around 120-150 mm^2 [130]. As shown in table 6.4, the total area of the prototypes developed here–for two outer diameters, is well below this range. This further highlights the ability of the present designs to compete on the novel market of the biodegradable implants.

6.3 Conclusions

Although drug-eluting metallic stents are effective, clinical data show that they initiate the formation of thrombus. Clinical studies show that coronary stents are needed only during the vascular healing, commonly lasting six months. Therefore, long-term side effects can be reduced with the use of Bioabsorbable Vascular Stents (BVS) that will provide adequate support at early stage until being replaced by tissue. Given two novel bioabsorbable materials (one natural $N1$ and one synthetic $S2$), two stent prototypes have been developed–one design per material.

A flexible tool to generated infinite family of designs was developed. While using engineering judgement and the analysis presented in the previous chapters, the key geometric parameters have been identified and included in the parameterisation. The modelling

of a coronary stent presented here addresses the crimping and the free stent expansion phases of deformation. Such analyses are used to extract information regarding the shape, stress and strain for the stent. It has been shown that the maximum stresses and strains are located in the sinusoidal rings, as predicted in the previous chapter.

The mechanical performance of novel structures has been evaluated via the use of computational modelling and preliminary trials. Numerical and preliminary investigations results have shown good agreement and success of the novel topologies. For the European project, two stent prototypes, one per material, have to be selected. Taking into consideration their performances, the natural tubes have been cut with the *auxetic* topology since it has shown better performances, in terms of recoil, compare to the *convex honeycomb*. The synthetic tubes have been cut with the *convex honeycomb* design–for this material both geometries gave a good performance. These two devices are currently at the stage of *in vivo* testing in big and small animals.

Chapter 7

Wrinkle-free films and elastic stabilisation by auxetic microstructure

Natural as well as engineered materials frequently appear in the form of membranes, films and elastic sheets. Biological membranes and skins provide partitioning and containment for soft matter [145–147]; stiff films over soft substrates are common in many electronic devices [148–150]; and membranes are frequently used as structural components within shape morphing aerodynamic surfaces–all with significance to a wide range of biological phenomena such as morphogenesis [151–154], cell motility [155], tissue differentiation [156] as well as to technological applications such as microfabrication [157; 158], adaptive aerodynamic drag control [159], characterisation of physical properties [160; 161], etc. Thin films usually wrinkle laterally when stretched [42]. Here we show that structured thin films with apparent negative Poisson's ratio are wrinkle-free within the bulk of a membrane upon being stretched, except localised near the clamped edges. Wrinkles that run along the edge but decay away from it, as reported here in the domain of elastic instability, have physical analogues of well-known trapped waves observed in wave phenomena. We develop a simple kinematic model to characterise the amplitude and the wavelength of anomalous edge wrinkles. The phenomenon of wrinkle-free stretching is found to be robust as it is observed in simulations as well as experiments and is found consistent with mathematical analysis. Resistance to wrinkling as reported here, in conjunction with previously known synclastic curvature of auxetic film, make them a promising candidate for future developments in the area of artificial skin, cardiac patches and biomedical stretchable sensors.

7.1 Introduction

The possibility of fabricating architectured materials has enabled the development of modern metamaterials that possess unusual properties that are not commonly found in naturally occurring materials. In the realm of elastic metamaterials, apparent properties leading to negative refractive index for sound propagation [162], negative Poisson's ratio [163], negative compressibility [164] and negative coefficient of expansion [165] have been observed before. Materials with negative Poisson's ratio are frequently referred to as *auxetic*. Recently, several reports have described the use of stretchable planar device, that adapt to natural soft surfaces, to monitor tissue response [166–168]. The mechanical behaviour of such planar devices resembles that of elastic membranes and they can develop wrinkles when a compressive state of stress is generated on the surface [169]. Buckling in thin films is a well known problem in mechanics [170; 171] and different solutions have been proposed–e.g. increase the thickness of the film directly derived from plate buckling analysis, inclusion of nanoparticles to lower the internal compressive stress [172–174]. The seamless integration of such devices with the tissue has been achieved by conferring a macroporous structure to the planar membrane [175]. Here we explore the more general elastic stabilisation properties of lattice membranes by tailoring the apparent negative Poisson's ratio. We report their anti-wrinkling behaviour under tension when usual elastic lattice membranes, with the Poisson's ratio $\nu > 0$, would suffer wrinkling. Poisson's ratio is a measure of lateral contraction when a piece of matter is stretched; its value is theoretically bound within the narrow range $-1 < \nu < 0.5$. For most naturally occurring materials such as polymers, metals and ceramics, the actual values lie within an even narrower range, between about 0.25 and 0.35.

Because of their low bending stiffness, membranes are prone to wrinkling and similar mechanical instabilities such as folding and creasing. Wrinkling is elastic instability which is often associated with compressive loading. Energetically, there is a competition between the strain energy stored within an elastic solid and the potential energy of loading. The latter is equal to the negative of the work done by external forces that gives rise to a 'kinematic stiffness'. When an elastic sheet is compressed within its own plane, the buckling instability arising is most easily explained in terms of such a competition of elastic strain energy and potential energy. Wrinkling of membranes has also been studied under pure shear which leads to principal stresses that are tensile as well as compressive–the compressive stresses being responsible for buckling. As opposed to these, Cerda and Mahadevan [42] recently reported the formation of folds and wrinkles within rectangular strips of thin films, when flat thin sheets are stretched in tension, except near the edges where they remains taut. This unusual elastic instability is under no compressive stresses in the direction of the waviness of wrinkles and is best explained via the structure requiring geometric fit to the same size as what the Poisson's shrinkage would produce. The essence of Cerda-Mahadevan-type instability, therefore, is the kinematic constraint posed by Poisson-contraction. The phenomenon is readily reproduced by stretching

thin membranes such as kitchen films made of polymer, the Poisson's ratio of the film material being in the range of 0.25 to 0.4. This instability was well characterised by Cerda and Mahadevan [42].

Geometric constraint dictates the overall Poisson's contraction to match with the shortening caused by wrinkle demanded by inextensibility [42]–a constraint that drives the wrinkles to form when the Poisson's ratio of the material is positive, as is the case with most naturally occurring materials. This provides us with the inspiration that such wrinkling in sheet material could be suppressed, if we could engineer the architecture of the material so that it possesses *apparent negative Poisson's ratio*. There are several well known such microstructures, perhaps the best known being that of inverted hexagonal cells. In such honeycomb materials, the mechanism of deformation is cell-wall bending and the level of porosity required for this elastic deformation to take place is high. Therefore we consider alternative lattice geometries where the negative Poisson's ratio is achieved by the rotation of approximate squares which lead to enlargement of the voids (hence negative apparent Poisson's ratio). This architecture is commonly used in mechanics [8; 176]. One such micro-structured film of length L and width b, with $L >> b$, is shown in figure 7.1. This sample was laser cut from an acetate sheet.

7.2 Materials and Methods

Thin lattice membranes used in this study were fabricated by engraving two different micro-patterns on uniform solid films to obtain two different membranes with positive and negative apparent Poisson's ratios respectively. The thin films were prepared using the laser cutting technique that allows cutting fine materials with high precision. A 0.102-mm-thick acetate film, commonly available in stationary stores for plain paper copier use, was attached firmly to a clean glass sheet. It was laser cut using the LS6840 LaserScript engraving machine–CO_2 laser tube technology. The cutting parameters, speed and power of the laser beam, were optimised by changing the process parameters systematically to obtain neat edges in the micro-patterns. The samples were manufactured by moving the laser beam at a speed of 63 mm/s and a laser tube power of 15 W. For the corners, a lower power of 13 W was chosen in order to obtain a clean cut with no burn into the polymer. The films were then attached using cyanoacrylates adhesives–commonly named as "Super Glue"–to wooden ends specifically designed to fit into the grips of the testing machine later used to characterised the samples. The ends were also laser cut from 3.5-mm-thick wooden sheets using the settings suggested in the Users Manual by the manufacture LaserScript–speed of 20 mm/s and 35 W power.

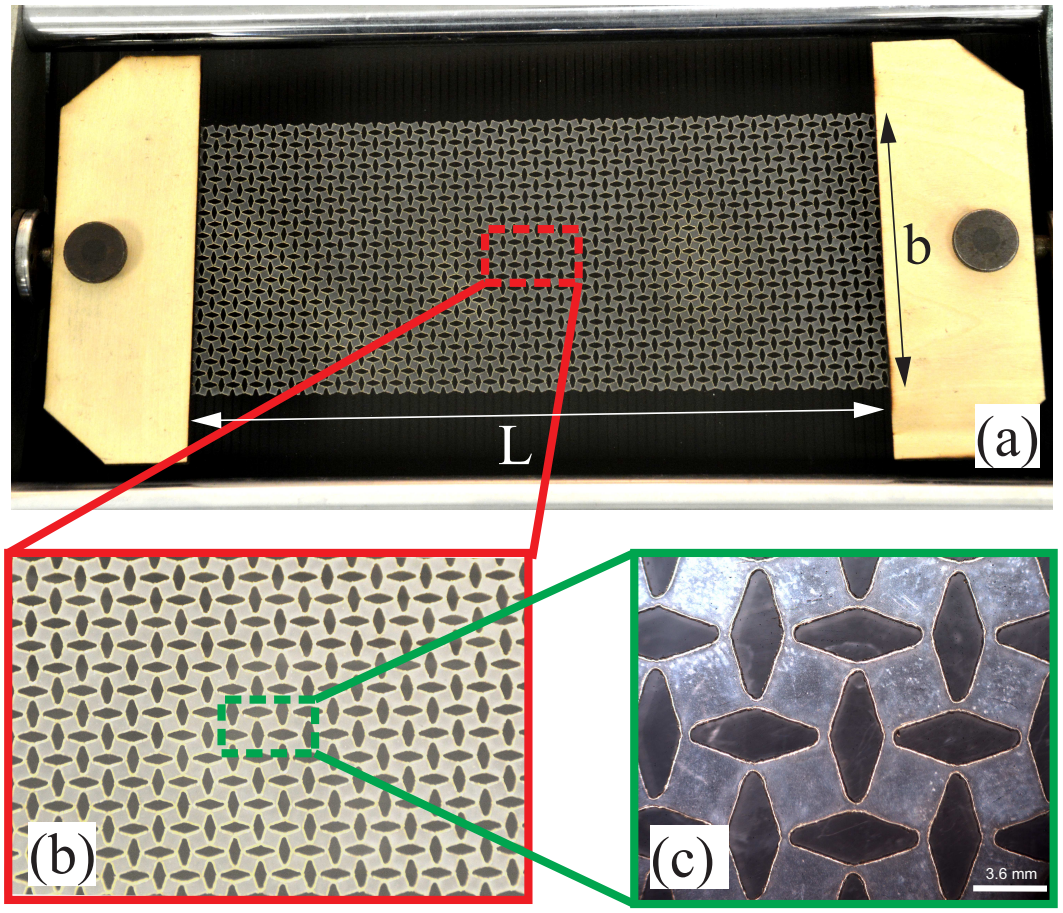

Figure 7.1: Structured cellulose acetate film mounted. (a) Complete experimental sample with perforation clamped at the ends. (b) Enlarged view showing the lattice of diamond shaped periodic holes. (c) A closer look highlights the essential square elements connected at small ligaments that allow rotation increasing the volume of the voids when stretched. Increase in void upon stretching leads to apparent negative Poissons ratio.

The qualitative behaviour of the auxetic membranes was studied at first by uniaxially stretch the films using a horizontal hand tensile testing machine–Tensometer WMonsanto. The force-displacement curves were obtained by using the Instron electrical mechanical test machine which provides a more accurate instrumentation. The acetate sheet were stretched uniaxially by 1.6 mm for the first auxetic sample, 1.2 mm for the second auxetic sample and 3.6 mm for the sample with positive Poisson's ratio on the Instron tensile machine. Since no information about the stiffness of the samples was available a priori, the calibration of the upper force limits (respectively 20 N for the first auxetic sample, 12 N for the second auxetic sample and 120N for the sample with positive Poisson's ratio) was performed initially by hand on trial samples. The test was performed under displacement control and the stretch was applied at a speed of 0.01 mm/s. Images of the wrinkling patterns (6 per sample) were recorded at constant displacement intervals (equal to $\Delta/6$ mm) with a NIKON D3200, fixed on a tripod, using a Tamron AF 18-200 mm F/3.5-6.3 XR. The flash was synchronised with the camera and

it has been positioned perpendicularly to the sample in order to reflect on the acetate surface and highlight the wrinkle profile.

7.3 Experimental results

A structured film that possesses positive apparent Poisson's ratio was tensioned and it shows wrinkling at the centre (figure 7.2 (a) shows initiation of such wrinkles), except at the fixed edges on the left and right where it is taut–this is an expected behaviour as reported by Cerda et al. [177] previously. The diamond shaped holes are now oriented on a 2D lattice differently (as shown in figure 7.1 (c)) so that the apparent Poisson's ratio of the film is negative. Note that while the film material had positive Poisson's ratio, the architecture of the porosity gives the film an apparent negative Poisson's ratio. When tension is applied parallel to the long edges of the structured auxetic film, it remains wrinkle-free and taut at the centre, as small amplitude anomalous wrinkles at the two short edges begin to appear (see figure 7.2 b). Upon increasing the tensile force, the localised wrinkles spread, still leaving the centre flat and wrinkle-free. For long films with small lateral width, the edge effects are confined closed to clamping, leaving most of the rectangular film wrinkle-free. The amplitude of these anomalous wrinkles at the edge increases as the tension in the film is increased. However, most of the centre of the sheet continues to be wrinkle free. This behaviour is in clear contrast with thin films made of material with positive Poisson's ratio as reported in [177] and [42] where most of the length-wise centre of the film is filled with wrinkles.

When tension in the auxetic film is increased, the localised wrinkles spread towards the centre and the amplitude of the wrinkles increases progressively (see figure 7.2 (c), note the centre of the film is still wrinkle free just below to the point of rupture of the film). To understand the formation of edge wrinkles qualitatively, consider the state of stress on an elastic element close to the clamped edge as schematically shown in figure 7.2 (d). Stresses can be transformed in the principal directions by rotation of the coordinate axes such that shear vanishes–one of the two principal stresses σ_1 is tensile (along the direction of the anomalous wrinkles) and compressive σ_2 across them, the latter causing the folds to form. This is in contrast with the films made of positive Poisson's ratio material tensioned similarly, where the principal stresses are *both tensile* in this biaxial state of stress close to clamping–the tension keeps the film near the clamped edges taught. In many ways, the situation is mirrored–bulk of the film is wrinkled when the Poisson's ratio is positive except neat the clamped edges, whereas the bulk of the auxetic film is wrinkle-free except the localised regions near the clamps. The stabilisation of wrinkles at the centre is observed experimentally and is shown in figure 7.2 (e) (auxetic film, showing stabilisation at the centre), whereas the spread of wrinkles within the film is shown in figure 7.2 (f) (non-auxetic film, showing wrinkling at the centre). Of course, wrinkles spread with increase in tension in both cases, as samples of finite length only

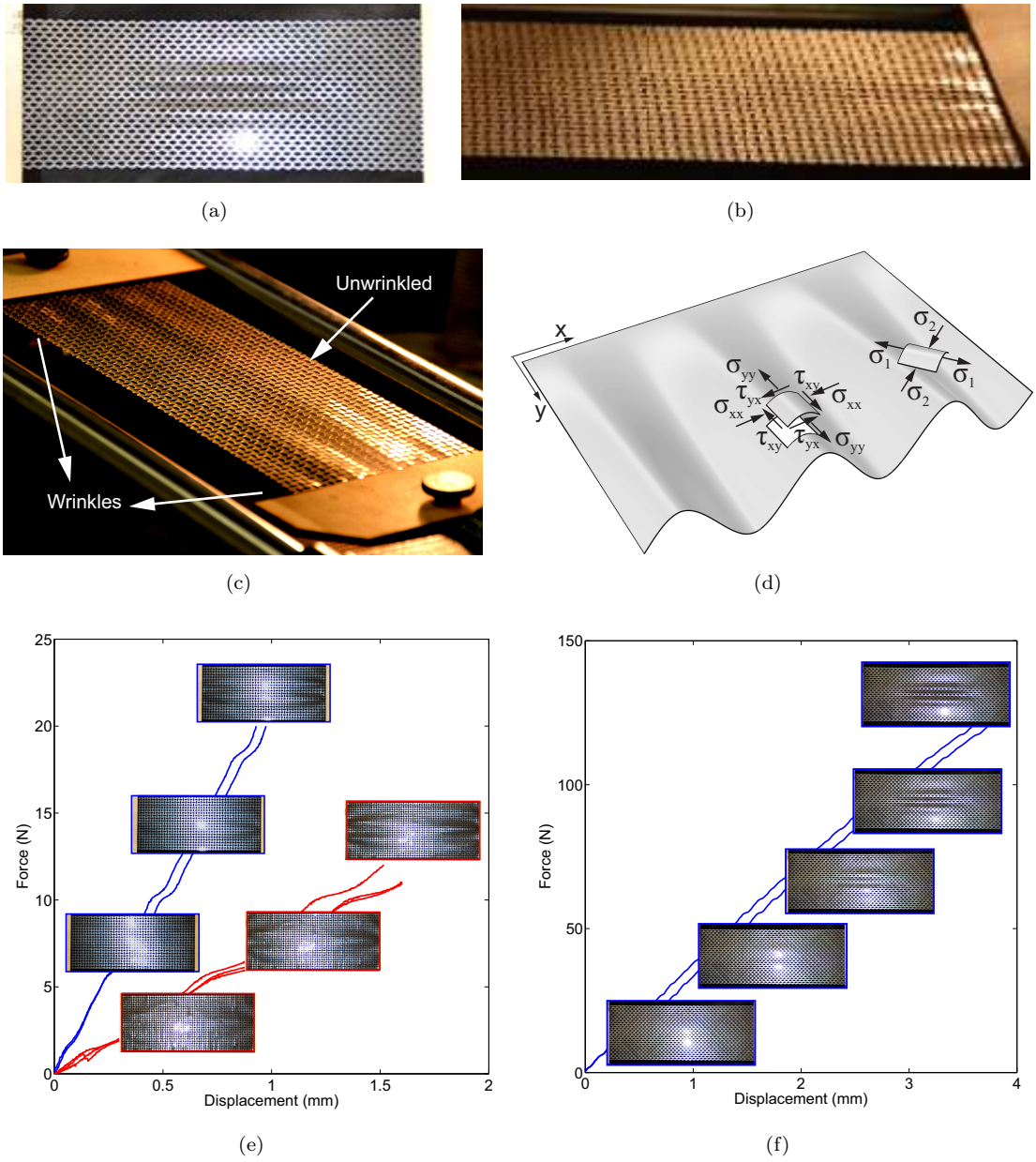

Figure 7.2: Auxetic film samples under tension. (a) structured film shows wrinkling except at the clamped edges, when the apparent Poisson's ratio of the perforated film is positive (b) Perforated film with apparent negative Poisson's ratio is stabilised at the centre. Anomalous localised wrinkles at the edges are observed leaving the bulk of the centre of the film to be wrinkle-free. (c) The amplitude of the anomalous edge folds increases upon increasing tension. Further increase in tension increases the amplitude of waviness. (d) Schematic diagram of the film near the clamped edges shows the development of biaxial state of stress leading to folds. A biaxial stress with tensile stress on one set of faces and compressive at the other is associated with localised fold formation near clamped edges. (e) Development of the localised wrinkles at the edges for increase tensile load. (f) Development of wrinkles everywhere except at the edges that are fixed laterally for increase tensile load.

could be tested in laboratory–the point is that for a long film, wrinkles are localised for auxetic films and stabilised regions exist for most of the film, whereas taught region is localised while wrinkles exist for large part of non-auxetic films.

A spatially localised wrinkle attached to the edge has an interesting physical analogue, well known in a host of wave phenomena, but not observed before in the context of elastic instability [178]. Trapped shallow water waves travel along the shore but are evanescent away from it [179–181]. The instability mode reported here is a trapped mode that "propagates" along the edge but is "confined" away from it. This behaviour is characterised by a sinusoidal dependence along the edge coordinate and an exponential decay away from the edge [182–184]. Perhaps the earliest known example of such an edge-confined travelling wave is the Rayleigh surface wave which travels on a surface freely but decays in the depth direction exponentially. Thin plates are known to possess such modes of localised energy propagation and are known as Konenkov waves [185]. Here we report an analogous phenomenon for instability modes for the first time. This is again mirrored in case of the non-auxetic films where there is a small persistence length near clamping over which the film is taut in the clamping region.

The mechanism of elastic stabilisation observed experimentally here can be understood qualitatively by realising that the structured membrane considered here will expand laterally upon stretching, except at the edges where the film is clamped. The lateral expansion is due to auxetic behaviour which possesses kinematic requirements that is just the opposite of non-auxetic membranes which need to fold in order to fit in width to a length dictated by Poissons shrinking. Thus we obtain a wrinkle-free membrane for most part of the auxetic film except at the short edges where the state of stress is biaxial. The shape of the experimentally observed localised wrinkles for auxetic films has approximately sinusoidal ripples across the width of the film, a rapid decay away from the clamped edges, which the wrinkle is pushed back to match the flatness of the clamped edge. This gives a "blister-like" appearance of the localised instability, which decays away from the clamped edges. To facilitate mathematical understanding of these complex blister shapes, we simplify the clamping condition by considering edges that constrain the film laterally (thus creating Poisson mismatch during tension) but are free to move in a direction normal to the surface of the film. This is hard to realise in practice but could be simulated easily by a computational experiment. Favouring simplicity over exactness of calculations, we represent such an edge-localised wrinkle by an exponential variation. Complex end shapes that decay away from ends are known to arise in other contents in elasticity–they are often exponentials (or alternatively hyperbolic sines and hyperbolic cosines) with an associated length scale. Here we allow the edge wrinkles to decay exponentially by letting the edge be free out-of-plane.

7.4 A kinematic theory

A simple geometric theory that provides relationship between the applied tensile stress and the amplitude of anomalous wrinkles near the clamped edges can be developed by enforcing the geometric compatibility demanded by Poisson's expansion when the apparent Poisson's ratio of the film is negative. The strain parallel to the direction of the applied tensile stress σ is given by $\epsilon^{||} = \sigma/E$, where E is the apparent Young's modulus of the structured film. The lateral strain far from the clamped edges is extensional and given by $\epsilon^{\perp} = -\nu\epsilon^{||}$, where the apparent Poisson's ratio ν of the perforated film is negative. If the localised wrinkles are approximated as sinusoidal ripples in the y-direction whereas exponentially decaying in the x-direction, so that $w(x, y) = A\sin(\pi y/\lambda)e^{-\pi x/l}$, the total lateral expansion is given by

$$\Delta b = \tfrac{1}{2}\int \left(\tfrac{\partial w}{\partial y}\right)^2 \mathrm{d}y = n^2\pi^2 A^2/b, \tag{7.1}$$

where l can be interpreted as the decay length scale associated with the wrinkle. Combining this with lateral Poisson extension far from the clamped edges, given by $\Delta b = \nu b\sigma/E$, we obtain the ratio of the amplitude of wrinkles to width, $A^* = A/b$, in terms of the applied tensile stress scaled with respect to the Young's modulus $\sigma^* = \sigma/E$, given by

$$A^* = \left(|\nu|\sigma^*\right)^{1/2}/n\pi. \tag{7.2}$$

The wavelength of wrinkles can be estimated from the vertical equilibrium of a shell which requires $\sigma_1\kappa + \sigma_c\kappa' = 0$ [186], where $\kappa = \partial^2 w/\partial x^2$ and $\kappa' = \partial^2 w/\partial y^2$ are the x-wise and y-wise curvatures respectively; $\sigma_c = \pi^2 E t^2/\left[12(1-\nu^2)\lambda^2\right]$ is the critical buckling load for a simply supported plate strip and σ_1 is approximately equal to the applied stress σ. Inserting the expressions for curvatures after differentiating $w(x, y)$ twice, we obtain an expression for the wavelength of the edge-localised wrinkles as

$$\lambda = (\pi t l)^{1/2}/\left[12\left(1-\nu^2\right)\epsilon^{||}\right]^{1/4}. \tag{7.3}$$

Further refinement in characterisation of the anomalous edge-wrinkles is possible by realising that the constraint at the clamped edges sets up a biaxial stress field with three components: tensile stresses, σ_x, along the direction of application of the external stress, compressive stress, σ_y, in the lateral direction, and shear stress, τ_{xy}, due to kinematic mismatch caused by the lateral Poisson's expansion everywhere away from the edge. The stress system is shown in figure 7.2 (d). The situation contrasts with that of a membrane with positive Poisson's ratio because the biaxial stress in that case is *tensile in both* directions, which keeps the membrane taut locally at the edges while the rest of the membrane suffers wrinkling instability. For auxetic films, each of the localised wrinkles runs principally away from the clamped edge and die out as we go sufficiently far from the edge. The sinusoidal waviness of the trapped instability mode runs along the

fixed edge. The state of stress is fairly complex and can be mathematically calculated by using the analysis of Bentham [187] after modifying the Poisson's ratio to be negative.

Simulations using material that possesses negative Poisson's ratio were carried out which confirm wrinkle-free continuum film except the appearance of localised wrinkles near the edges when such structured films are stretched. The direction of computationally obtained folds, that decay away from the edges, aligns well with the mathematically derived directions of principal stresses (the black arrows in figure 7.3 (a); the vertical edge at on the left end represents the line along clamps). The principal directions are titled slightly so that the folds align themselves with the tensile principal stress direction whereas the waviness of the wrinkles is along the compressive principal stress directions. There is a remarkable consistency between the predicted directions of folds and those observed computationally. Computational experiments using Finite Element Analysis were then carried out for micro-structured film under tension. The results for such perforated films under tension are shown in figure 7.3 (a) (the clamped edge is at the right).

We carried out numerical experiments using finite element analysis of structured films shown in figure 7.3 (a). The laser cut geometry has been imported as a solid structure from Rhinoceros 5 (Robert McNeel & Associates) into the commercial software Abaqus. The thin film has been modelled as a 3D structure using the element type C3D8I (8-node brick element) within Abaqus. This element has geometric non-linearity capability which are switched on. The number of degrees-of-freedom per node is 3 and the total number of elements over 35,000 which was arrived systematically by increasing this till convergence was achieved. Acetate sheets have a Young's modulus (E) of 1.6 GPa and Poisson's ratio (ν) of 0.38 [188], which have been used for the computational simulations. Note again that while the film material had positive Poisson's ratio, the architecture gives the film an apparent negative Poisson's ratio. When tension is increased gradually in simulations, the centre of the auxetic film remains taut and wrinkle-free, while localised waviness starts to appear near the edges, also as observed in laboratory experiments. The edge effect is local and waviness decays away from the clamped edges leaving the bulk of the film flat–just the opposite of what happens with wrinkling of elastic sheets made of positive Poisson's ratio material under tension where the taut portion is localised to the vicinity of the clamped edges while most of the centre of the film wrinkles. The visual observations of taut centre accompanied by the localised edge wrinkles were quantitatively examined by simulating the tension response of structured auxetic films near the edges. The amplitude and the wavelength were measured from the numerical results for a range of films with varying properties. The results were plotted for numerically observed values of the amplitude (figure 7.3 (b)) and the wavelength (figure 7.3 (c)) as a function of the values predicted on the basis of equations (7.2) and (7.2). Each dot represents measurements of amplitude of the localised and wavelength from a computer experiment. The different corolurs refer to different values of Poisson's

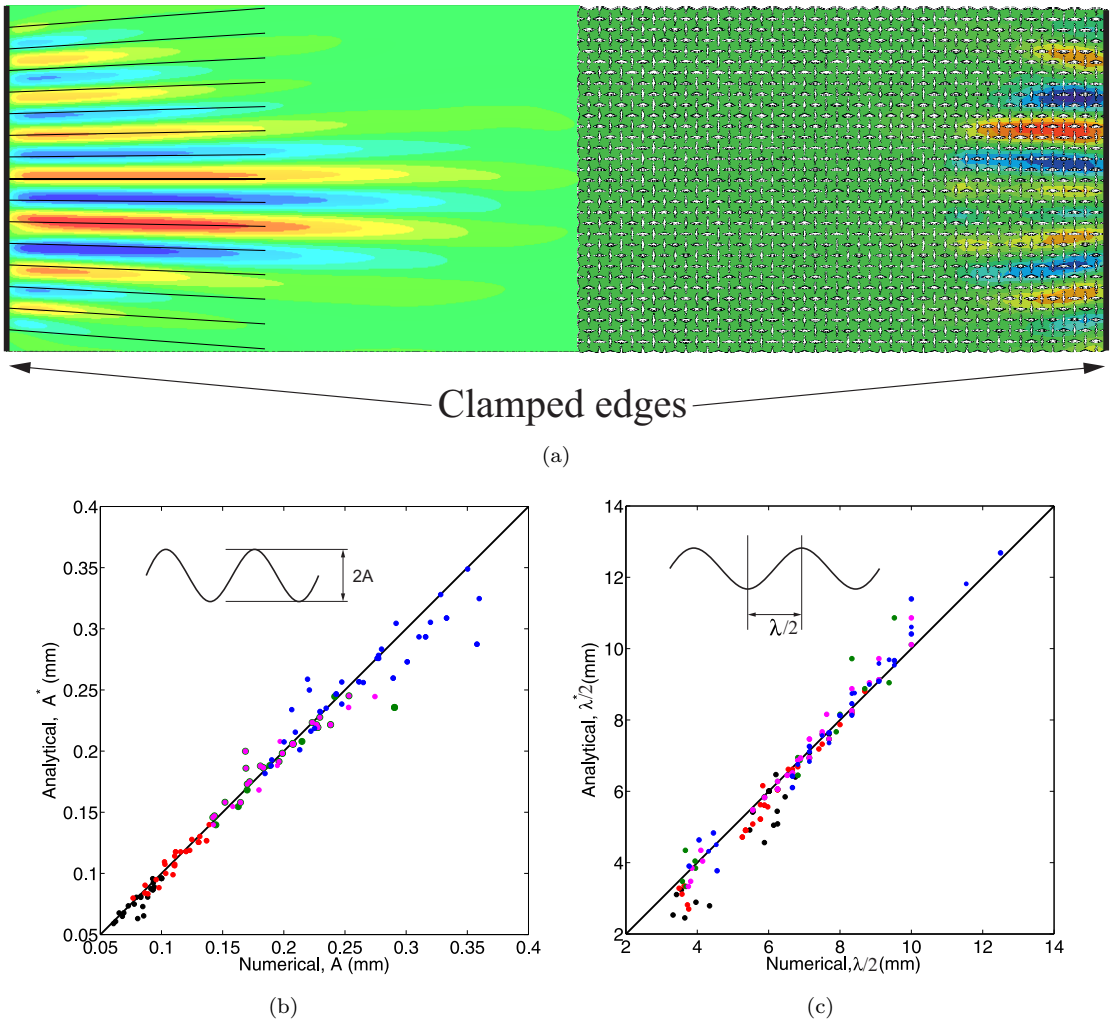

Figure 7.3: (a) Comparison numerical results assuming an homogeneous material with negative effective Poisson's ratio (left side) and with the rigid rotating units (right side). The principle stress directions are plotted on top of the numerical results for an homogeneous material. the Comparison between prediction based on kinematic model and simulation. (b) Amplitude of edge-localised wrinkles vs simulation. (c) Wavelength of the loacalised wrinkles vs simulation.

ratios (-0.2, -0.4, -0.6, -0.8, -0.9 respectively). For each Poisson's ratio, films with different L/b ratios (10, 7 and 5) and thickness (0.01 mm, 0.05 mm and 0.1 mm) have been stretched. It is reasonable, for order of magnitude calculations, to take the decay length scale l in equation (7.2) to be half of the length of the film. Over this length scale, the amplitude decays to a value of $e^{-\pi} \sim 4.3\%$ of its amplitude at the edge. The model of anomalous wrinkling at the edges is in excellent agreement with the values obtained from simulations as demonstrated by the scatter of points close to the straight line with a perfect relationship.

7.5 Conclusions

Thin films with structured porosity were tested experimentally. The architecture of perforations was such that films with apparent negative or positive Poisson's ratio could be fabricated. For films with negative Poisson's ratio, elastic stabilisation was observed which is in contrast with the well known behaviour of wrinkling of membranes. The stabilisation thus achieved is accompanied by anomalous edge wrinkles. The unusual behaviour for auxetic films was attributed to the kinematics of lateral expansion under stretch. A simple kinematic theory to characterise the amplitude and the wavelength of the edge-localised wrinkles was presented. The predicted trends show excellent qualitative agreement with the amplitude and wavelength of localised wrinkles as obtained from numerical experiments. The localisation of wrinkles is interpreted as elastic instability similar to trapped waves in wave phenomena.

Chapter 8

Conclusions and Future work

At the end of each chapter, specific conclusions relevant to the work presented were reported. Here we summarise the general conclusions of the project and the possible extensions for future work.

8.1 Concluding remarks

Several structures and materials show an internal architecture characterized by regularity. Their mechanical response under elastic deformation has been extensively studied in the past. However, very few analytical attempts have been made regarding the response of regular lattice structures under plastic deformation. This study has been inspired by a biomedical context i.e. cardiovascular stent amongst other biomedical implants. There seems to be a gap in the literature with regards to analytical results even for the simplest lattice geometry–the hexagonal honeycomb–that could be used as benchmarks or could serve as first approximation for more complex geometries.

We developed an analytical model to study the elasto-plastic deformation and the recoil of a two-dimensional hexagonal honeycomb sheet under an in-plane uniaxial remote stress. At first, the constitutive material model assumed is that of an elastic-perfectly-plastic material. Interestingly, the lattice response shows a smooth transition between elastic and plastic regime, even though the constitutive material law is piece-wise linear. The elastic springback of the lattice structure upon unloading was analytically calculated. Under the assumption of small deformation, the combination of dimensional and scaling arguments show the dependence of the effective Poisson's ratio on the cell geometry alone. The underlying reason for this is that 1D elasticity does not incorporate Poisson's ratio in the calculation of transverse response. By varying the geometric parameters of a hexagonal cell, the mechanical response of the lattices show similarities. This affords a '*non-linear master deformation profile*'–thus collapsing data for all the

combinations of lattice and material parameters. A separation of the non-linear mechanics of the cell wall and the lattice kinematics is achieved. This, together with the scaling transformations, enables response curves to be transformed to a single curve for various parametric changes. The 'master curve' was fully characterised for critical points such as those at transition to plasticity, collapse, relevant slope and shape, via non-dimensional numbers and non-dimensional functions describing shapes. The model was then applied to the inverted hexagonal lattice that shows a negative apparent Poisson's ratio. The results of the analysis presented here are in good agreement with computational results. The response of such auxetic lattice under plastic deformation was presented for the first time.

The analytical model developed at first for an hexagonal unit cell has been extended to include the hardening effects due to plasticity. This has been possible by proposing a hyperbolic model for the stress-strain curve of the constituent material. The apparent response of a honeycomb sheet is dictated by that of a single strut, which is modelled as a cantilever beam with both axial and transverse force. The mathematical representation of the material law gave us the possibility to calculate exactly the elasto-plastic response of a beam with rectangular cross-section, which represents a cell wall, subjected to an inclined tip load. The beam model has been applied to an infinite lattice structure providing the mechanical response of such a structure while taking into consideration the material hardening effects. Additive manufacturing (AM) has recently shown promise as an alternative for the fabrication of lattice materials because it gives the opportunity of the controlled deposition of matter in the 3D-space. Frequently the nozzle has a circular shape. This has inspired us for the extension of the theory developed above for regular cellular materials whom cell-walls have circular cross-section. Two models for elasto-plastic deformation of beam with circular cross-section have been developed. The first model assumes an elastic-perfectly-plastic material, while the second model takes into consideration the effects of the non-linear hardening behaviour shown by real materials. They have been next adopted to infer the macroscopic response of a regular 2D cellular lattice structure.

Computational modelling is commonly used to assess the mechanical performance of cardiovascular stents. However, it requires a large amount of computational resources and time. By using a simplification in the material model and an abstraction of the actual stent geometry, we have been able to provide an analytical model that predicts the mechanical behaviour of these bio-structures that experience elasto-plastic deformation. The development of the analysis presented in this work has been possible by exploiting the common geometric features of such biomedical devices. Stent geometries exhibit a remarkable structural periodicity. They are made of wavy crowns that are connected by straight or curved bridges, to provide flexibility during the deployment. This simplified problem possesses all the generic features of stent mechanics and the derived model has been directly applied to the development of new stent prototypes, as part of a

collaborative European project [41] which aims to introduce two novel bioresorbable cardiovascular stents on the market. Bioresorbable stents represent the fourth-generation stent–a scaffold that dissolves in the human body after 6 months. The mechanical performance of the two novel stents has been finally assessed via the use of computational modelling and preliminary trial tests. The two devices are currently at the stage of *in vivo* testing. The benefits and effectiveness of mathematical analysis within a practical context have been most satisfying.

Constrained thin films under tensile load show elastic instability problems. An internal compressive state of stress gives rise to wrinkling over the all structure. In this work, we achieved the stabilisation of such membranes by manufacturing films with negative Poisson's ratio. When these manufactured films are subjected to tensile loading, the instability problem is mostly solved since the main body of the film is wrinkle-free. However, a localised wrinkling occurs at the clamped edges. Such unusual behaviour of auxetic films was successfully characterised experimentally, computationally and analytically. A simple kinematic model was introduced to characterise the amplitude and wavelength of the localised wrinkles. The predicted values were in good agreement with those obtained computationally for auxetic films with different Poisson's ratios and geometries.

To summarise, the main contributions of this thesis are as follows:

- Here we analytically presented the complete non-linear response that describes the apparent stress-strain relationship of any hexagonal lattice sheet when deformed plastically (Chapter 3).
- The effects of material hardening have been included in the analytical model developed before. This has been made possible by a newly proposed hyperbolic hardening model to describe the constitutive material. The new model has been successfully validated using numerical results (Chapter 4).
- Analytical calculation of the elasto-plastic response of periodic biostructures, when the crown is modelled as a sinusoid, was carried out. This further enabled us to calculate the internal pressure vs radial expansion for realistic cylindrical meshed devices such as stents (Chapter 5).
- Two novel designs, of which one exhibits auxetic behaviour, were successfully developed. Further *in vivo* trials are under progress by other researchers engaged in this collaborative project [41] (Chapter 6).
- We reported for the first time that auxetic microstructure stabilises wrinkling in thin films. Edge effects were observed, characterised and experimentally validated (Chapter 7).

8.2 Future work

This dissertation represents a contribution to the area of cellular materials and design of biomedical devices. However, several other aspects require further study. They are itemised below:

- The models presented here refer to lattices with a regular microstructure. As next step, the elasto-plastic response of cellular solids with random microstructure can be studied. It would be interesting to check if the general conclusions drawn for two-dimensional lattice materials hold for two-dimensional materials with a random microstructure. The possibility to predict the mechanical behaviour of materials with random microstructure based on that of the correspondent lattice with the same relative density could be explored. This idea is based on experimental observations, which show that the collapse stress of a random structure is roughly 30% lower than that of the correspondent regular honeycomb lattice possessing the same relative density (see Chapter 2).

- The present work is limited to the elasto-plastic analysis of two-dimensional lattices. The structural response of three-dimensional models is a problem closely related and of high relevance in the area of biomedical implants, such as bone replacement.

- The analytical models developed in this work are based on thin beam theory; therefore, the shear effects are neglected throughout. As the next step, the effects of shear deformation on the elasto-plastic response of periodic structures can be studied.

- Closely related to the previous point, the stretch deformation inside the lattice struts has been neglected. Study including such effect could be undertaken.

- The analyses presented above are restricted to small strains. As the next step, the effect of large deformations can be included in the study. A model that includes both geometric and material non-linearities can perhaps be useful in engineering applications, such as metal forming processes.

- In the prediction of springback, both kinematic hardening and plastic anisotropy have been neglected. The reduction in stiffness during the plastic loading, due to the Bauschinger effect, is very important when several cycles of stress past plasticity are applied. Including such effects into the analytical model might be useful for specific applications under repetitive load.

- The fact that the stent is a finite structure results in a non-uniform radial expansion of the tube–the so call dog-boning effect. An analytical model to quantify the

changes along the length can perhaps be developed by making use of the perturbation analysis. This effect is highly undesirable during the deployment; therefore, an analytical assessment of the dog-boning will be useful to identify the effect of the geometric parameters on the overall response while giving general guidelines to the designer.

- The elasto-plastic model developed for idealised stents could be extended to the calculation of the elastic recoil. This will provide an explicit relationship between the geometric and material parameters with the response of cardiovascular stents.

- To further optimise the expansion of the new stent, a more realistic computational model must be developed. Consequently, the balloon should be included into the analysis. This will require the compliance chart of the balloon-catheter–the relationship between applied pressure and diameter of the balloon.

- The stress in the artery tissue is strictly related to the stent geometry. Minimising the maximum stress and, therefore, obtaining a uniformly distributed stress are two important aspects to take into consideration during the design of the stent. Including the artery and the plaque into the computational model is the next step to study and improve the performance of the two prototypes.

Appendix A

Elasto-plastic analysis of circular cross-section

In order to find the stress distribution in a circular cross-section given an applied load, the axial force and moment equilibrium are imposed. A detailed derivation is presented in this Appendix.

A.1 Elastic-perfectly-plastic material: primary plastic regime, PI

The area of the circular segment that has undergone plasticity is given by

$$A_{c0} = r^2(\theta_0 - \sin\theta_0 \cos\theta_0) = r^2(\theta_0 - \sin 2\theta_0/2). \tag{A.1}$$

The y-position of its centroid is calculated as

$$y_{c0} = 2r\sin^3\theta_0/\left[3(\theta_0 - \sin\theta_0\cos\theta_0)\right] = 2r\sin^3\theta_0/\left[3(A_c/r^2)\right] = 2r^3\sin^3\theta_0/(3A_c)\,. \tag{A.2}$$

We can carry out integrations in the (r, θ) polar coordinates such that $y = r\cos\theta$. The stress distribution in the elastic area of this regime is obtained as

$$\sigma(y) = \sigma_y \times (y + d)/c, \tag{A.3}$$

after imposing

$$\sigma(y = c - d) = \sigma_y \quad \text{and} \quad \sigma(y = -r) = \sigma_y \times (-r + d)/c. \tag{A.4}$$

Hence in polar coordinates the stress profile is calculated as

$$\sigma(\theta) = \sigma_y(r\cos\theta + d)/c. \tag{A.5}$$

Imposing static equilibrium in the longitudinal direction leads to

$$A_c\sigma_y + \int_{-r}^{c-d} [2r\sin\theta\sigma(y)]\,\mathrm{d}y = N \tag{A.6}$$

or in polar coordinates

$$A_c\sigma_y + (2\sigma_y/c)\int_{\pi}^{\theta_0} [(r\cos\theta + d)r\sin\theta(-r\sin\theta)]\,\mathrm{d}\theta = N \tag{A.7}$$

which after integration and substitution of A_c from equation (A.1) becomes

$$(\theta_0 - \sin 2\theta_0/2) - (2/c)\left[r\sin^3\theta_0/3 + d(\theta_0 - \sin 2\theta_0/2)/2 - \pi d/2\right] = N/(r^2\sigma_y). \tag{A.8}$$

Imposing momentum equilibrium leads to

$$A_c\sigma_y y_c + 2\int_{\pi}^{\theta_0} [yr\sin\theta\sigma(\theta)]\,\mathrm{d}y = M \tag{A.9}$$

which after substitution of A_c from equation (A.1), y_c from equation (A.2) and $y = r\cos\theta$ and integration becomes

$$2\sin^3\theta_0/3 - (2/c)\left[-r\pi/8 + r(\theta_0 - \sin 4\theta_0/4)/8 + d\sin^3\theta_0/3\right] = M/(r^3\sigma_y). \tag{A.10}$$

Equation (5.8), (A.8) and (A.10) respectively form a set of simultaneous equations in three unknowns c, d and θ_0.

$$\begin{cases} \cos\theta_0 = (c-d)/r \\ \pi d/c + (\theta_0 - \sin 2\theta_0/2)(1 - d/c) - (2r/3c)\sin^3\theta_0 = N/(r^2\sigma_y) \\ \pi r/4c + 2(1 - d/c)\sin^3\theta_0/3 - (r/4c)(\theta_0 - \sin 4\theta_0/4) = M/(r^3\sigma_y) \end{cases} \tag{A.11}$$

Solving the first of these equations for d and substituting in the second and the third, and then eliminating d, we have

$$\begin{cases} (\pi - \theta_0 + \sin 2\theta_0/2)\cos\theta_0 + 2\sin^3\theta_0/3 = \left[\pi - N/(r^2\sigma_y)\right](c/r) \\ (\pi - \theta_0 + \sin 4\theta_0/4)/4 + 2\sin^3\theta_0\cos\theta_0/3 = \left[M/(r^3\sigma_y)\right](c/r) \end{cases} \tag{A.12}$$

c/r can now be eliminated from one of the above equations, leading to a single equation depending only the unknown θ_0.

A.2 Elastic-perfectly-plastic material: secondary plastic regime, PII

The areas of the two circular segments are respectively given by

$$A_{c1} = r^2(\theta_1 - \sin 2\theta_1/2) \quad \text{and} \quad A_{c2} = r^2(\theta_2 - \sin 2\theta_2/2) \tag{A.13}$$

and the y-position of their centroids is respectively calculated as

$$y_{c1} = 2r^3 \sin^3 \theta_1/(3A_{c1}) \quad \text{and} \quad y_{c2} = 2r^3 \sin^3 \theta_2/(3A_{c2}). \tag{A.14}$$

The boundaries between elastic and plastic deformation on the two sides of the beam are

$$\cos\theta_1 = (c-d)/r \quad \text{and} \quad \cos\theta_2 = (c+d)/r = \cos\theta_1 + 2d/r. \tag{A.15}$$

Imposing static equilibrium in the longitudinal direction leads to

$$A_{c1}\sigma_y - A_{c2}\sigma_y + \int_{-c-d}^{c-d} [2r\sin\theta\sigma(y)]\,\mathrm{d}y = N \tag{A.16}$$

which, after substituting the expressions for the circular segment areas (A.13), equation (A.15) and carrying out the integration, becomes:

$$(\theta_1 - \frac{1}{2}\sin 2\theta_1) - (\theta_2 - \frac{1}{2}\sin 2\theta_2) - \frac{4}{3}\frac{\sin^3\theta_1 - \sin^3\theta_2}{\cos\theta_1 + \cos\theta_2} + \frac{\cos\theta_1 - \cos\theta_2}{\cos\theta_1 + \cos\theta_2}(\pi - \theta_1 - \theta_2) + \\ + \frac{1}{2}\sin 2\theta_1 + \frac{1}{2}\sin 2\theta_2 = n. \tag{A.17}$$

Imposing the momentum equilibrium leads to

$$A_{c1}\sigma_y y_1 - A_{c2}\sigma_y t_2 + \int_{-c-d}^{c-d} [2r\sin\theta y\sigma(y)]\,\mathrm{d}y = M \tag{A.18}$$

which after integrating and substituting equations (A.13), (A.14) and (A.15) into the above equation becomes

$$2\sin^3\theta_1/3 + 2\sin^3\theta_2/3 - \\ (2/c)\left\{d(\sin^3\theta_1 - \sin^3\theta_2)/3 - r\left[-4(\theta_1 + \theta_2 - \pi) + \sin 4\theta_1 + \sin 4\theta_2\right]/32\right\} = M/(r^3\sigma_y). \tag{A.19}$$

A.3 Non-linear hardening model: stress distribution

By assuming an non-linear material with hyperbolic hardening, the stress distribution in the cross-section takes the form of $\sigma(\epsilon) = (B\epsilon + D)/(A - \epsilon)$. Imposing that $\sigma(d) = 0$ and $\sigma(c - d) = \sigma_y$ leads to

$$\sigma(y) = \frac{B(\epsilon_y/c)(y + d) + D}{A - (\epsilon_y/c)(y + d)} \tag{A.20}$$

The mathematical description of the stress distribution in polar coordinates is obtain by substituting $y = r\cos\theta$ into (A.20)

$$\sigma(\theta) = \frac{B(\epsilon_y/c)(r\cos\theta + d) + D}{A - (\epsilon_y/c)(r\cos\theta + d)}. \tag{A.21}$$

Appendix B

Linear mechanics of two-dimensional honeycomb with circular cross-section

The linear elastic response of honeycomb is primarily caused by bending. Each wall is modelled as a beam of radius r and Young's modulus E. The Eulero-Bernulli beam formulation is used throughout the work; therefore, the shear deformation and axial extension or compression are neglected.

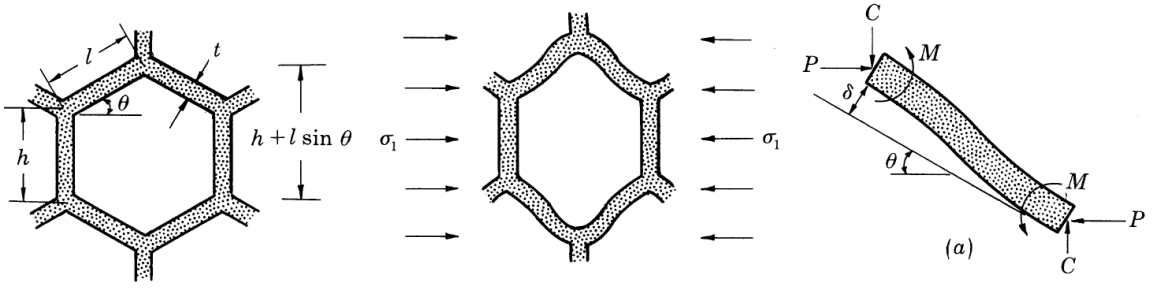

Figure B.1: Cell deformation under loading in the x-direction [33].

The force acting at the end of the cell wall is given by

$$P = \sigma_\infty (h + l\sin\theta) 2r, \tag{B.1}$$

where σ_∞ is the remote stress applied to the honeycomb, h the high of the straight members, l the length of the inclined struts, θ the angle between the straight and tilted members and r the radius of the cross-section of the struts.

From standard beam theory, the wall deflection is given by

$$\delta = Pl^3 \sin\theta / 12EI, \tag{B.2}$$

where $I = r^4\pi/4$ is the second moment of inertia for a circular cross-section.

The projection along the x direction gives a strain equal to

$$\epsilon_{||} = \frac{\delta \sin\theta}{l\cos\theta} = \frac{2\sigma_\infty}{3E\pi}\frac{(h/l+\sin\theta)\sin^2\theta}{\cos\theta}\left(\frac{l}{r}\right)^3. \tag{B.3}$$

The Young's modulus parallel to x direction is $\langle E\rangle = \sigma_\infty/\epsilon_{||}$, giving

$$\langle E\rangle = E\frac{3\pi}{2}\left(\frac{r}{l}\right)^3\frac{(h/l+\sin\theta)\sin^2\theta}{\cos\theta}. \tag{B.4}$$

Appendix C

Elasto-plastic analysis of sinusoidal beams

The horizontal displacement of the sinusoid stretched at infinity is given by the sum of the contribution made by the segment under elastic deformation and that undergone plasticity. A detailed derivation in presented here.

The total horizontal displacement is given by

$$\delta = 4\left(\delta_{\text{elastic}} + 2\delta_{\text{plastic}}\right). \tag{C.1}$$

The contribution given by the segment under plastic deformation is calculated as $\delta_{\text{elastic}} = \partial C_{\text{elastic}}/\partial F$, where C_{elastic} is given by equation (5.7). Differentiating the expression for the complementary energy leads to

$$\begin{aligned}\delta_{\text{elastic}} = \frac{(FA\sin kx_y)^2}{2EI}\sqrt{1+C_1\cos^2(kx_y)}\left(-\frac{1}{k\sqrt{1-x_y^2}}\frac{x_y}{FA}\right) + \frac{F}{EI}\frac{1}{3k^3} \\ \left\{-C_1\cos kx_y\sin kx_y\sqrt{1+C_1\cos^2(kx_y)} + \cdot\right. \\ (C_1+1)\left[K\left(-C_1\right) - F\left(\arcsin\cos kx_y, -C_1\right)\right] + \\ \left.(C_1-1)\left[E\left(-C_1\right) - E\left(\arcsin\cos kx_y, -C_1\right)\right]\right\}\end{aligned} \tag{C.2}$$

where the incomplete integral of the first kind is defined as

$$F(\phi, m) = \int_0^{\phi} \frac{1}{\sqrt{1-m\sin^2\theta}}\mathrm{d}\theta. \tag{C.3}$$

When ϕ is equal to $\pi/2$, we obtain the complete elliptic integral of the first kind

$$K(m) = F(\pi/2, m) = \int_0^{\pi/2} \frac{1}{\sqrt{1 - m\sin^2\theta}} \mathrm{d}\theta. \tag{C.4}$$

The incomplete elliptic integral of the second kind is defined as follows

$$E(\phi, m) = \int_0^{\phi} \sqrt{1 - m\sin^2\theta} \mathrm{d}\theta. \tag{C.5}$$

When ϕ is equal to $\pi/2$ we obtaine the complete elliptic integral of the second kind, which becomes

$$E(m) = \int_0^{\pi/2} \sqrt{1 - m\sin^2\theta} \mathrm{d}\theta. \tag{C.6}$$

The calculation of the total complementary energy of the part of the sinusoid undergone plastic deformation is more cumbersome. The complementary energy density $u_c(x, z)$ for the segment undergone plastic deformation $x_y < x < L$ is defined in equation (5.8). The total complementary energy of a cross section is given by the contribution of the fibres undergone plastic deformation and those still under elastic deformation

$$C_{\text{plastic}} = 2b \left(\int_{x_y}^{\lambda/4} \int_0^{c(x)} u_c^{\text{elastic}} C_{\mathrm{d}s/\mathrm{d}x} \mathrm{d}z\mathrm{d}x + \int_{x_y}^{\lambda/4} \int_{c(x)}^{t/2} u_c^{\text{plastic}} C_{\mathrm{d}s/\mathrm{d}x} \mathrm{d}z\mathrm{d}x \right) \tag{C.7}$$

By integrating respect to z the expression above, we obtain

$$C_{\text{plastic}} = \frac{b}{6}\frac{\sigma_y^2}{E} \int_{x_y}^{\lambda/4} c(x) C_{\mathrm{d}s/\mathrm{d}x} \mathrm{d}x + \frac{bt}{4}\frac{\sigma_y^2}{E} \int_{x_y}^{\lambda/4} C_{\mathrm{d}s/\mathrm{d}x} \mathrm{d}x - \frac{b}{2}\frac{\sigma_y^2}{E} \int_{x_y}^{\lambda/4} c(x) C_{\mathrm{d}s/\mathrm{d}x} \mathrm{d}x, \tag{C.8}$$

which can be simplified, resulting in equation (5.10).

Applying Leibniz's rule for differentiation under the integral sign leads to

$$\begin{aligned} \delta_{\text{plastic}} = -\frac{\sigma_y^2 b}{3kE} \Bigg[\sqrt{3\left(\frac{t^2}{4} - \frac{FA\sin\theta_P}{\sigma_y b}\right)} \left(-\frac{M_y}{F^2 A} \frac{C_{\mathrm{d}s/\mathrm{d}\theta}}{\sqrt{1 - M_y/(FA)^2}} \right) - \\ \frac{3A}{2\sigma_y b} \int_{\theta_P}^{\pi/2} \sin\theta C_{\mathrm{d}s/\mathrm{d}\theta} / \sqrt{3\left[h^2/4 - FA\sin\theta/\left(\sigma_y b\right)\right]} \mathrm{d}\theta \Bigg] + \\ \frac{bt}{4k}\frac{\sigma_y^2}{E} \left(M_y \sqrt{(AFk)^2 - (M_y F)^2 + F^2} / F^2 \sqrt{(AF)^2 - M_y^2} \right), \end{aligned} \tag{C.9}$$

where $C_{\mathrm{d}s/\mathrm{d}\theta} = \sqrt{1 + C_1 \cos^2(k\theta)}$. By substituting equations (C.2) and (C.9) into (C.1), the axial displacement of a period of a sinusoid under elasto-plastic deformation is obtained.

Bibliography

[1] A. Bonfanti and A. Bhaskar, "Spring back of infinite honeycomb sheets beyond plastic deformation," *IOP Conference Series: Materials Science and Engineering*, vol. 74, no. 1, p. 012003, 2015.

[2] A. Bonfanti, A. Bhaskar, and M. Ashby, "Plastic deformation of cellular materials," *Reference Module in Materials Science and Materials Engineering*, pp. 1–7, 2016.

[3] L. J. Gibson and M. F. Ashby, *Cellular Solids: Structure and Properties*. Cambridge University Press, 1999.

[4] E. Tuncer, "Numerical calculations of effective elastic properties of two cellular structures," *Journal of Physics D: Applied Physics*, vol. 38, no. 3, p. 497, 2005.

[5] G. Chen, X. Zhao, X. Wang, H. Jin, S. Li, S. Dong, A. Flewitt, W. Milne, and J. Luo, "Film bulk acoustic resonators integrated on arbitrary substrates using a polymer support layer," *Scientific Reports*, vol. 5, 2015.

[6] EngineerLive, "Aircraft sandwich composite reinforcing and repairs," 2013.

[7] S. Hendrixson, "Uav takes flight with 80 percent 3d-printed parts," 2015.

[8] Y. Cho, J.-H. Shin, A. Costa, T. A. Kim, V. Kunin, J. Li, S. Y. Lee, S. Yang, H. N. Han, I.-S. Choi, *et al.*, "Engineering the shape and structure of materials by fractal cut," *Proceedings of the National Academy of Sciences*, vol. 111, no. 49, pp. 17390–17395, 2014.

[9] Gizmodo, "Michelin's airless tire might actually start existing," 2014.

[10] K. M. Group, "Cranial osteosynthesis," 2015.

[11] Heart and V. Team, "Researchers study new stents pros, cons," 2013.

[12] M. Ashby, "The properties of foams and lattices," *Philosophical Transactions of the Royal Society of London A: Mathematical, Physical and Engineering Sciences*, vol. 364, no. 1838, pp. 15–30, 2006.

[13] J. F. Nye, *Physical Properties of Crystals: their representation by tensors and matrices*. Oxford University Press, 1985.

[14] N. Fleck, V. Deshpande, and M. Ashby, "Micro-architectured materials: past, present and future," in *Proceedings of the Royal Society of London A: Mathematical, Physical and Engineering Sciences*, vol. 466, pp. 2495–2516, The Royal Society, 2010.

[15] L. J. Gibson, M. F. Ashby, and B. A. Harley, *Cellular Materials in Nature and Medicine*. Cambridge University Press, 2010.

[16] N. Hoff, "Structural problems of future aircraft," in *Proceedings of the Third Anglo-American Aeronautical Conference*, pp. 77–114, 1951.

[17] A. C. Eringen, "Bending and buckling of rectangular sandwich plates," in *Journal of Applied Mechanics-Transactions of the ASME*, vol. 18, pp. 330–330, ASME-Amer Soc Mechanical Eng 345 E 47TH ST, New York, NY 10017, 1951.

[18] R. Duckett, S. Rabinowitz, and I. Ward, "The strain-rate, temperature and pressure dependence of yield of isotropic poly (methylmethacrylate) and poly (ethylene terephthalate)," *Journal of Materials Science*, vol. 5, no. 10, pp. 909–915, 1970.

[19] A. Gent and A. G. Thomas, "The deformation of foamed elastic materials," *Journal of Applied Polymer Science*, vol. 1, no. 1, pp. 107–113, 1959.

[20] M. F. Ashby, T. Evans, N. A. Fleck, J. Hutchinson, H. Wadley, and L. Gibson, *Metal Foams: A Design Guide*. Elsevier, 2000.

[21] V. Deshpande, M. Ashby, and N. Fleck, "Foam topology: bending versus stretching dominated architectures," *Acta Materialia*, vol. 49, no. 6, pp. 1035–1040, 2001.

[22] Y. Aminanda, B. Castanié, J.-J. Barrau, and P. Thevenet, "Experimental analysis and modeling of the crushing of honeycomb cores," *Applied Composite Materials*, vol. 12, no. 3-4, pp. 213–227, 2005.

[23] S. D. Papka and S. Kyriakides, "Experiments and full-scale numerical simulations of in-plane crushing of a honeycomb," *Acta Materialia*, vol. 46, no. 8, pp. 2765–2776, 1998.

[24] A. Markaki and T. Clyne, "The effect of cell wall microstructure on the deformation and fracture of aluminium-based foams," *Acta Materialia*, vol. 49, no. 9, pp. 1677–1686, 2001.

[25] A. Ajdari, H. Nayeb-Hashemi, and A. Vaziri, "Dynamic crushing and energy absorption of regular, irregular and functionally graded cellular structures," *International Journal of Solids and Structures*, vol. 48, no. 3, pp. 506–516, 2011.

[26] J. Shim, C. Perdigou, E. R. Chen, K. Bertoldi, and P. M. Reis, "Buckling-induced encapsulation of structured elastic shells under pressure," *Proceedings of the National Academy of Sciences*, vol. 109, no. 16, pp. 5978–5983, 2012.

[27] K. Bertoldi, P. M. Reis, S. Willshaw, and T. Mullin, "Negative poisson's ratio behavior induced by an elastic instability," *Advanced Materials*, vol. 22, no. 3, pp. 361–366, 2010.

[28] N. Ohno, D. Okumura, and H. Noguchi, "Microscopic symmetric bifurcation condition of cellular solids based on a homogenization theory of finite deformation," *Journal of the Mechanics and Physics of Solids*, vol. 50, no. 5, pp. 1125–1153, 2002.

[29] S. Papka and S. Kyriakides, "Biaxial crushing of honeycombs:part 1: Experiments," *International Journal of Solids and Structures*, vol. 36, no. 29, pp. 4367–4396, 1999.

[30] B. Haghpanah, J. Papadopoulos, D. Mousanezhad, H. Nayeb-Hashemi, and A. Vaziri, "Buckling of regular, chiral and hierarchical honeycombs under a general macroscopic stress state," in *Proceedings of the Royal Society of London A: Mathematical, Physical and Engineering Sciences*, vol. 470, p. 20130856, The Royal Society, 2014.

[31] G. Health and Aging, "Living longer," 2015.

[32] M. Bulati, M. Pellicanò, S. Vasto, and G. Colonna-Romano, "Understanding ageing: Biomedical and bioengineering approaches, the immunologic view," *Immunity & Ageing*, vol. 5, no. 1, p. 1, 2008.

[33] L. Gibson, M. Ashby, G. Schajer, and C. Robertson, "The mechanics of two-dimensional cellular materials," in *Proceedings of the Royal Society of London A: Mathematical, Physical and Engineering Sciences*, vol. 382, pp. 25–42, The Royal Society, 1982.

[34] G. C. Engelmayr, G. D. Papworth, S. C. Watkins, J. E. Mayer, and M. S. Sacks, "Guidance of engineered tissue collagen orientation by large-scale scaffold microstructures," *Journal of Biomechanics*, vol. 39, no. 10, pp. 1819–1831, 2006.

[35] G. C. Engelmayr, M. Cheng, C. J. Bettinger, J. T. Borenstein, R. Langer, and L. E. Freed, "Accordion-like honeycombs for tissue engineering of cardiac anisotropy," *Nature Materials*, vol. 7, no. 12, pp. 1003–1010, 2008.

[36] A. S. Go, D. Mozaffarian, V. L. Roger, E. J. Benjamin, J. D. Berry, W. B. Borden, D. M. Bravata, S. Dai, E. S. Ford, C. S. Fox, *et al.*, "Heart disease and stroke statistics–2013 update: a report from the american heart association.," *Circulation*, vol. 127, no. 1, p. e6, 2013.

[37] N. C. for Chronic Disease Prevention and H. Promotion, "Heart disease facts," 2015.

[38] N. H. Lung and B. Institute, "Who needs coronary angioplasty?," 214.

[39] W. M. Saltzman, *Biomedical Engineering: Bridging Medicine and Technology*. Cambridge University Press, 2009.

[40] J. A. Rogers, R. Ghaffari, and D.-H. Kim, *Stretchable Bioelectronics for Medical Devices and Systems*. Springer, 2016.

[41] ReBioStent, "Reinforced bioresorbable biomaterials for therapeutic drug eluting stents," 2014.

[42] E. Cerda and L. Mahadevan, "Geometry and physics of wrinkling," *Physical Review Letters*, vol. 90, no. 7, p. 074302, 2003.

[43] H. N. Wadley, T. Børvik, L. Olovsson, J. J. Wetzel, K. P. Dharmasena, O. S. Hopperstad, V. Deshpande, and J. W. Hutchinson, "Deformation and fracture of impulsively loaded sandwich panels," *Journal of the Mechanics and Physics of Solids*, vol. 61, no. 2, pp. 674–699, 2013.

[44] M. Tilbrook, D. Radford, V. Deshpande, and N. Fleck, "Dynamic crushing of sandwich panels with prismatic lattice cores," *International Journal of Solids and Structures*, vol. 44, no. 18, pp. 6101–6123, 2007.

[45] K. P. Dharmasena, H. N. Wadley, Z. Xue, and J. W. Hutchinson, "Mechanical response of metallic honeycomb sandwich panel structures to high-intensity dynamic loading," *International Journal of Impact Engineering*, vol. 35, no. 9, pp. 1063–1074, 2008.

[46] H. Wadley, K. Dharmasena, Y. Chen, P. Dudt, D. Knight, R. Charette, and K. Kiddy, "Compressive response of multilayered pyramidal lattices during underwater shock loading," *International Journal of Impact Engineering*, vol. 35, no. 9, pp. 1102–1114, 2008.

[47] F. Abd El-Sayed, R. Jones, and I. Burgess, "A theoretical approach to the deformation of honeycomb based composite materials," *Composites*, vol. 10, no. 4, pp. 209–214, 1979.

[48] H. Guoming, W. Hui, Z. Youlin, and B. Wujun, "A large deformation model for the elastic moduli of two-dimensional cellular materials," *Journal of Wuhan University of Technology-Mater. Sci. Ed.*, vol. 21, no. 2, pp. 154–157, 2006.

[49] A.-J. Wang and D. McDowell, "In-plane stiffness and yield strength of periodic metal honeycombs," *Journal of Engineering Materials and Technology*, vol. 126, no. 2, pp. 137–156, 2004.

[50] A. K. Noor, "Continuum modeling for repetitive lattice structures," *Applied Mechanics Reviews*, vol. 41, no. 7, pp. 285–296, 1988.

[51] R. S. Kumar and D. L. McDowell, "Generalized continuum modeling of 2-d periodic cellular solids," *International Journal of Solids and Structures*, vol. 41, no. 26, pp. 7399–7422, 2004.

[52] G. Menges and F. Knipschild, "Estimation of mechanical properties for rigid polyurethane foams," *Polymer Engineering & Science*, vol. 15, no. 8, pp. 623–627, 1975.

[53] J. Klintworth and W. Stronge, "Elasto-plastic yield limits and deformation laws for transversely crushed honeycombs," *International Journal of Mechanical Sciences*, vol. 30, no. 3, pp. 273–292, 1988.

[54] H. Zhu and N. Mills, "The in-plane non-linear compression of regular honeycombs," *International Journal of Solids and Structures*, vol. 37, no. 13, pp. 1931–1949, 2000.

[55] D. Karagiozova and T. Yu, "Plastic deformation modes of regular hexagonal honeycombs under in-plane biaxial compression," *International Journal of Mechanical Sciences*, vol. 46, no. 10, pp. 1489–1515, 2004.

[56] C.-H. Chuang and J.-S. Huang, "Yield surfaces for hexagonal honeycombs with plateau borders under in-plane biaxial loads," *Acta Mechanica*, vol. 159, no. 1-4, pp. 157–172, 2002.

[57] A.-J. Wang and D. McDowell, "Yield surfaces of various periodic metal honeycombs at intermediate relative density," *International Journal of Plasticity*, vol. 21, no. 2, pp. 285–320, 2005.

[58] S. D. Papka and S. Kyriakides, "In-plane compressive response and crushing of honeycomb," *Journal of the Mechanics and Physics of Solids*, vol. 42, no. 10, pp. 1499–1532, 1994.

[59] C. Chen, T. Lu, and N. Fleck, "Effect of imperfections on the yielding of two-dimensional foams," *Journal of the Mechanics and Physics of Solids*, vol. 47, no. 11, pp. 2235–2272, 1999.

[60] K. Mangipudi, S. Van Buuren, and P. Onck, "The microstructural origin of strain hardening in two-dimensional open-cell metal foams," *International Journal of Solids and Structures*, vol. 47, no. 16, pp. 2081–2096, 2010.

[61] W. Johnson and P. B. Mellor, *Engineering Plasticity*. E. Horwood, 1983.

[62] S. Kaliszky, *Plasticity: Theory and Engineering Applications*. Elsevier Amsterdam, 1989.

[63] D. Rees, *Basic Engineering Plasticity: An Introduction with Engineering and Manufacturing Applications*. Butterworth-Heinemann, 2006.

[64] J. Chakrabarty, *Theory of Plasticity*. Butterworth-Heinemann, 2006.

[65] M. Saje, G. Turk, A. Kalagasidu, and B. Vratanar, "A kinematically exact finite element formulation of elastic–plastic curved beams," *Computers & structures*, vol. 67, no. 4, pp. 197–214, 1998.

[66] R. Mines and N. Jones, "Approximate elastic-plastic analysis of the static and impact behaviour of polymer composite sandwich beams," *Composites*, vol. 26, no. 12, pp. 803–814, 1995.

[67] T. Yu and W. Johnson, "Influence of axial force on the elastic-plastic bending and springback of a beam," *Journal of Mechanical Working Technology*, vol. 6, no. 1, pp. 5–21, 1982.

[68] W. Prager and P. G. Hodge, "Theory of perfectly plastic solids," *Mathematical Association of America*, 1951.

[69] B. Štok and M. Halilovič, "Analytical solutions in elasto-plastic bending of beams with rectangular cross section," *Applied Mathematical Modelling*, vol. 33, no. 3, pp. 1749–1760, 2009.

[70] Y. Xu, L. Zhang, and T. Yu, "The elastic-plastic pure bending and springback of l-shaped beams," *International Journal of Mechanical Sciences*, vol. 29, no. 6, pp. 425–433, 1987.

[71] A. El-Domiaty and A. Elsharkawy, "Stretch-bending analysis of u-section beams," *International Journal of Machine Tools and Manufacture*, vol. 38, no. 1, pp. 75–95, 1998.

[72] J. Zhao, R. Zhai, Z. Qian, and R. Ma, "A study on springback of profile plane stretch–bending in the loading method of pretension and moment," *International Journal of Mechanical Sciences*, vol. 75, pp. 45–54, 2013.

[73] S. Baragetti, "A theoretical study on nonlinear bending of wires," *Meccanica*, vol. 41, no. 4, pp. 443–458, 2006.

[74] K. Samuel, "Limitations of hollomon and ludwigson stress–strain relations in assessing the strain hardening parameters," *Journal of Physics D: Applied Physics*, vol. 39, no. 1, p. 203, 2006.

[75] Y. Dafalias and E. Popov, "A model of nonlinearly hardening materials for complex loading," *Acta Mechanica*, vol. 21, no. 3, pp. 173–192, 1975.

[76] V. Hardenacke and J. Hohe, "Local probabilistic homogenization of two-dimensional model foams accounting for micro structural disorder," *International Journal of Solids and Structures*, vol. 46, no. 5, pp. 989–1006, 2009.

[77] G. Katgert, B. P. Tighe, M. E. Möbius, and M. van Hecke, "Couette flow of two-dimensional foams," *EPL (Europhysics Letters)*, vol. 90, no. 5, p. 54002, 2010.

[78] M. J. Silva, W. C. Hayes, and L. J. Gibson, "The effects of non-periodic microstructure on the elastic properties of two-dimensional cellular solids," *International Journal of Mechanical Sciences*, vol. 37, no. 11, pp. 1161–1177, 1995.

[79] H. Zhu, J. Hobdell, and A. Windle, "Effects of cell irregularity on the elastic properties of 2d voronoi honeycombs," *Journal of the Mechanics and Physics of Solids*, vol. 49, no. 4, pp. 857–870, 2001.

[80] H. Harders, K. Hupfer, and J. Rösler, "Influence of cell wall shape and density on the mechanical behaviour of 2d foam structures," *Acta Materialia*, vol. 53, no. 5, pp. 1335–1345, 2005.

[81] T. Triantafillou, J. Zhang, T. Shercliff, L. Gibson, and M. Ashby, "Failure surfaces for cellular materials under multiaxial loadsii. comparison of models with experiment," *International Journal of Mechanical Sciences*, vol. 31, no. 9, pp. 665–678, 1989.

[82] M. J. Silva and L. J. Gibson, "The effects of non-periodic microstructure and defects on the compressive strength of two-dimensional cellular solids," *International Journal of Mechanical Sciences*, vol. 39, no. 5, pp. 549–563, 1997.

[83] C. San Marchi and A. Mortensen, "Deformation of open-cell aluminum foam," *Acta Materialia*, vol. 49, no. 19, pp. 3959–3969, 2001.

[84] E. Amsterdam, J. T. M. De Hosson, and P. Onck, "On the plastic collapse stress of open-cell aluminum foam," *Scripta Materialia*, vol. 59, no. 6, pp. 653–656, 2008.

[85] A. T. Ong, J. Aoki, E. P. McFadden, and P. W. Serruys, "Classification and current treatment options of in-stent restenosis," *Herz*, vol. 29, no. 2, pp. 187–194, 2004.

[86] S. Cook, P. Wenaweser, M. Togni, M. Billinger, C. Morger, C. Seiler, R. Vogel, O. Hess, B. Meier, and S. Windecker, "Incomplete stent apposition and very late stent thrombosis after drug-eluting stent implantation," *Circulation*, vol. 115, no. 18, pp. 2426–2434, 2007.

[87] J. Gunn and D. Cumberland, "Does stent design influence restenosis?," *European Heart Journal*, vol. 20, no. 14, pp. 1009–1013, 1999.

[88] J. Gunn, N. Arnold, K. Chan, L. Shepherd, D. Cumberland, and D. Crossman, "Coronary artery stretch versus deep injury in the development of in-stent neointima," *Heart*, vol. 88, no. 4, pp. 401–405, 2002.

[89] R. Mongrain and J. Rodés-Cabau, "Role of shear stress in atherosclerosis and restenosis after coronary stent implantation," *Revista Española de Cardiología*, vol. 59, no. 01, pp. 1–4, 2006.

[90] M. Edelman, R. Elazer, M. Rogers, *et al.*, "Pathobiologic responses to stenting," *The American Journal of Cardiology*, vol. 81, no. 7, pp. 4E–6E, 1998.

[91] E. Cecchi, C. Giglioli, S. Valente, C. Lazzeri, G. F. Gensini, R. Abbate, and L. Mannini, "Role of hemodynamic shear stress in cardiovascular disease," *Atherosclerosis*, vol. 214, no. 2, pp. 249–256, 2011.

[92] A. Kastrati, J. Mehilli, J. Dirschinger, J. Pache, K. Ulm, H. Schühlen, M. Seyfarth, C. Schmitt, R. Blasini, F.-J. Neumann, *et al.*, "Restenosis after coronary placement of various stent types," *The American Journal of Cardiology*, vol. 87, no. 1, pp. 34–39, 2001.

[93] A. C. Morton, D. Crossman, and J. Gunn, "The influence of physical stent parameters upon restenosis," *Pathologie Biologie*, vol. 52, no. 4, pp. 196–205, 2004.

[94] J. E. Sousa, M. A. Costa, A. Abizaid, F. Feres, A. C. Seixas, L. F. Tanajura, L. A. Mattos, R. Falotico, J. Jaeger, J. J. Popma, *et al.*, "Four-year angiographic and intravascular ultrasound follow-up of patients treated with sirolimus-eluting stents," *Circulation*, vol. 111, no. 18, pp. 2326–2329, 2005.

[95] R. Virmani, G. Guagliumi, A. Farb, G. Musumeci, N. Grieco, T. Motta, L. Mihalcsik, M. Tespili, O. Valsecchi, and F. D. Kolodgie, "Localized hypersensitivity and late coronary thrombosis secondary to a sirolimus-eluting stent should we be cautious?," *Circulation*, vol. 109, no. 6, pp. 701–705, 2004.

[96] R. Kenedi, *Advances in Biomedical Engineering*, vol. 1. Elsevier, 2013.

[97] A. Vascuolar, "Absorb: The worlds first fully bioresorbable vascular scaffold," 2014.

[98] E. M. Corporation, "Desolve eluting bioresorbable coronary scaffold system," 2014.

[99] J. C. Squire, *Dynamics of Endovascular Stent Expansion.* PhD thesis, Massachusetts Institute of Technology, 2000.

[100] S. Morlacchi and F. Migliavacca, "Modeling stented coronary arteries: where we are, where to go," *Annals of Biomedical Engineering*, vol. 41, no. 7, pp. 1428–1444, 2013.

[101] F. J. Gijsen, F. Migliavacca, S. Schievano, L. Socci, L. Petrini, A. Thury, J. J. Wentzel, A. F. van der Steen, P. W. Serruys, and G. Dubini, "Simulation of stent deployment in a realistic human coronary artery," *Biomedical Engineering Online*, vol. 7, no. 1, p. 23, 2008.

[102] N. Gonzalo, H. M. Garcia-Garcia, E. Regar, P. Barlis, J. Wentzel, Y. Onuma, J. Ligthart, and P. W. Serruys, "In vivo assessment of high-risk coronary plaques at bifurcations with combined intravascular ultrasound and optical coherence tomography," *JACC: Cardiovascular Imaging*, vol. 2, no. 4, pp. 473–482, 2009.

[103] G. De Santis, M. De Beule, P. Segers, P. Verdonck, and B. Verhegghe, "Patient-specific computational haemodynamics: generation of structured and conformal hexahedral meshes from triangulated surfaces of vascular bifurcations," *Computer Methods in Biomechanics and Biomedical Engineering*, vol. 14, no. 9, pp. 797–802, 2011.

[104] F. Auricchio, M. Di Loreto, and E. Sacco, "Finite-element analysis of a stenotic artery revascularization through a stent insertion," *Computer Methods in Biomechanics and Biomedical Engineering*, vol. 4, no. 3, pp. 249–263, 2001.

[105] C. Dumoulin and B. Cochelin, "Mechanical behaviour modelling of balloon-expandable stents," *Journal of Biomechanics*, vol. 33, no. 11, pp. 1461–1470, 2000.

[106] J. McGarry, B. O'donnell, P. McHugh, and J. McGarry, "Analysis of the mechanical performance of a cardiovascular stent design based on micromechanical modelling," *Computational Materials Science*, vol. 31, no. 3, pp. 421–438, 2004.

[107] C. Lally, F. Dolan, and P. Prendergast, "Cardiovascular stent design and vessel stresses: a finite element analysis," *Journal of Biomechanics*, vol. 38, no. 8, pp. 1574–1581, 2005.

[108] F. Migliavacca, L. Petrini, V. Montanari, I. Quagliana, F. Auricchio, and G. Dubini, "A predictive study of the mechanical behaviour of coronary stents by computer modelling," *Medical Engineering & Physics*, vol. 27, no. 1, pp. 13–18, 2005.

[109] C. Rogers, D. Y. Tseng, J. C. Squire, and E. R. Edelman, "Balloon-artery interactions during stent placement a finite element analysis approach to pressure, compliance, and stent design as contributors to vascular injury," *Circulation Research*, vol. 84, no. 4, pp. 378–383, 1999.

[110] M. De Beule, P. Mortier, S. G. Carlier, B. Verhegghe, R. Van Impe, and P. Verdonck, "Realistic finite element-based stent design: the impact of balloon folding," *Journal of Biomechanics*, vol. 41, no. 2, pp. 383–389, 2008.

[111] ASME., "Asme v&v 10-2006: Guide for verification and validation in computational solid mechanics," 2006.

[112] D. Gastaldi, S. Morlacchi, R. Nichetti, C. Capelli, G. Dubini, L. Petrini, and F. Migliavacca, "Modelling of the provisional side-branch stenting approach for the treatment of atherosclerotic coronary bifurcations: effects of stent positioning," *Biomechanics and Modeling in Mechanobiology*, vol. 9, no. 5, pp. 551–561, 2010.

[113] F. Gervaso, C. Capelli, L. Petrini, S. Lattanzio, L. Di Virgilio, and F. Migliavacca, "On the effects of different strategies in modelling balloon-expandable stenting by means of finite element method," *Journal of Biomechanics*, vol. 41, no. 6, pp. 1206–1212, 2008.

[114] Y. Jie and H. Nan, "Formula for elastic radial stiffness of the tubular vascular stent," in *6th World Congress of Biomechanics (WCB 2010). August 1-6, 2010 Singapore*, pp. 1435–1438, Springer, 2010.

[115] Y. Jie and H. Nan, "Mechanical formula for the plastic limit pressure of stent during expansion," *Acta Mechanica Sinica*, vol. 25, no. 6, pp. 795–801, 2009.

[116] M. R. Jedwab and C. O. Clerc, "A study of the geometrical and mechanical properties of a self-expanding metallic stenttheory and experiment," *Journal of Applied Biomaterials*, vol. 4, no. 1, pp. 77–85, 1993.

[117] A. Bhaskar, "The effective poisson ratio of random cellular matter having bending dominated architecture," *EPL (Europhysics Letters)*, vol. 87, no. 1, p. 18004, 2009.

[118] G. I. Barenblatt, *Scaling, Self-similarity, and Intermediate Asymptotics: Dimensional Analysis and Intermediate Asymptotics*, vol. 14. Cambridge University Press, 1996.

[119] G. Taylor, "The formation of a blast wave by a very intense explosion. i. theoretical discussion," *Proceedings of the Royal Society of London. Series A, Mathematical and Physical Sciences*, pp. 159–174, 1950.

[120] G. N. Greaves, A. Greer, R. Lakes, and T. Rouxel, "Poisson's ratio and modern materials," *Nature Materials*, vol. 10, no. 11, pp. 823–837, 2011.

[121] R. Lakes, "Materials science: A broader view of membranes," *Nature*, vol. 414, no. 6863, pp. 503–504, 2001.

[122] I. Masters and K. Evans, "Models for the elastic deformation of honeycombs," *Composite structures*, vol. 35, no. 4, pp. 403–422, 1996.

[123] M. Warner, B. Thiel, and A. Donald, "The elasticity and failure of fluid-filled cellular solids: theory and experiment," *Proceedings of the National Academy of Sciences*, vol. 97, no. 4, pp. 1370–1375, 2000.

[124] Additive3D, "Extrusion deposition: Fused deposition modeling (fdm)," 2016.

[125] F. Riemelmoser and G. Mocko, "Mechanical properties of additive manufactured honeycomb structures," Master's thesis, Fachhochschule Karnten, 2015.

[126] B. S. Chun, H.-S. Lim, M. Sagong, and K. Kim, "Development of a hyperbolic constitutive model for expanded polystyrene (eps) geofoam under triaxial compression tests," *Geotextiles and Geomembranes*, vol. 22, no. 4, pp. 223–237, 2004.

[127] B. S. S. Association, "Comparison of structural design in stainless steel and carbon steel." www.bssa.org.uk/topics.php?article=125, nd. Accessed: 2015-11-16.

[128] S. Fare, Q. Ge, M. Vedani, G. Vimercati, D. Gastaldi, F. Migliavacca, L. Petrini, and S. Trasatti, "Evaluation of material properties and design requirements for biodegradable magnesium stents," *Materia (Rio de Janeiro)*, vol. 15, no. 2, pp. 96–103, 2010.

[129] B. Rajani, "Nonlinear stress–strain characterization of cast iron used to manufacture pipes for water supply," *Journal of Engineering Materials and Technology*, vol. 134, no. 4, p. 041005, 2012.

[130] P. W. Serruys and M. J. Kutryk, *Handbook of Coronary Stents*. London: Martin Dunitz Ltd, 2011, 2011.

[131] R. Bonita, R. Beaglehole, and T. Kjellström, *Basic Epidemiology*. World Health Organization, 2006.

[132] U. F. D. Administration, "Us food & drug administration," 2015.

[133] G. Sarno, N. Bruining, Y. Onuma, S. Garg, S. Brugaletta, S. De Winter, E. Regar, L. Thuesen, D. Dudek, S. Veldhof, *et al.*, "Morphological and functional evaluation of the bioresorption of the bioresorbable everolimus-eluting vascular scaffold using ivus, echogenicity and vasomotion testing at two year follow-up: a patient level insight into the absorb a clinical trial," *The International Journal of Cardiovascular Imaging*, vol. 28, no. 1, pp. 51–58, 2012.

[134] F. Amin, M. N. Ali, U. Ansari, M. Mir, M. A. Minhas, and W. Shahid, "Auxetic coronary stent endoprosthesis: fabrication and structural analysis.," *Journal of Applied Biomaterials & Functional Materials*, vol. 13, no. 2, 2015.

[135] J. Raamachandran and K. Jayavenkateshwaran, "Modeling of stents exhibiting negative poisson's ratio effect," *Computer Methods in Biomechanics and Biomedical Engineering*, vol. 10, no. 4, pp. 245–255, 2007.

[136] S. Fabregues, K. Baijens, R. Rieu, and P. Bergeron, "Hemodynamics of endovascular prostheses," *Journal of Biomechanics*, vol. 31, no. 1, pp. 45–54, 1997.

[137] J. Dodge, B. G. Brown, E. L. Bolson, and H. T. Dodge, "Lumen diameter of normal human coronary arteries. influence of age, sex, anatomic variation, and

left ventricular hypertrophy or dilation.," *Circulation*, vol. 86, no. 1, pp. 232–246, 1992.

[138] G. J. Hall and E. P. Kasper, "Comparison of element technologies for modeling stent expansion," *Journal of Biomechanical Engineering*, vol. 128, no. 5, pp. 751–756, 2006.

[139] B. Engineering, "Balloon expandable stent crimpers," 2016.

[140] A. Version, "6.13 documentation (abaqus), 2013," *Abaqus Users Guide*.

[141] N. Debusschere, P. Segers, P. Dubruel, B. Verhegghe, and M. De Beule, "A finite element strategy to investigate the free expansion behaviour of a biodegradable polymeric stent," *Journal of Biomechanics*, vol. 48, no. 10, pp. 2012–2018, 2015.

[142] Arterious. personal communication 2016-06-03.

[143] S. Zhao, L. Gu, and S. R. Froemming, "On the importance of modeling stent procedure for predicting arterial mechanics," *Journal of Biomechanical Engineering*, vol. 134, no. 12, p. 121005, 2012.

[144] H.-M. Hsiao and Y.-H. Chiu, "Assessment of mechanical integrity for drug-eluting renal stent with micro-sized drug reservoirs," *Computer Methods in Biomechanics and Biomedical Engineering*, vol. 16, no. 12, pp. 1307–1318, 2013.

[145] W. T. Huck, "Artificial skins: hierarchical wrinkling," *Nature Materials*, vol. 4, no. 4, pp. 271–272, 2005.

[146] K. Efimenko, M. Rackaitis, E. Manias, A. Vaziri, L. Mahadevan, and J. Genzer, "Nested self-similar wrinkling patterns in skins," *Nature Materials*, vol. 4, no. 4, pp. 293–297, 2005.

[147] M. Kücken and A. C. Newell, "A model for fingerprint formation," *EPL (Europhysics Letters)*, vol. 68, no. 1, p. 141, 2004.

[148] J. A. Rogers, T. Someya, and Y. Huang, "Materials and mechanics for stretchable electronics," *Science*, vol. 327, no. 5973, pp. 1603–1607, 2010.

[149] R.-H. Kim, D.-H. Kim, J. Xiao, B. H. Kim, S.-I. Park, B. Panilaitis, R. Ghaffari, J. Yao, M. Li, Z. Liu, *et al.*, "Waterproof alingap optoelectronics on stretchable substrates with applications in biomedicine and robotics," *Nature Materials*, vol. 9, no. 11, pp. 929–937, 2010.

[150] R. J. Hamers, "Flexible electronic futures," *Nature*, vol. 412, no. 6846, pp. 489–490, 2001.

[151] Q. Wang and X. Zhao, "A three-dimensional phase diagram of growth-induced surface instabilities," *Scientific Reports*, vol. 5, 2015.

[152] P. Ball and N. R. Borley, *The self-made tapestry: pattern formation in nature*, vol. 198. Oxford University Press Oxford, 1999.

[153] D. W. Thompson *et al.*, *On growth and form*. Cambridge University Press, 1942.

[154] J. B. Bard and J. Bard, *Morphogenesis: the Cellular and Molecular Processes of Developmental Anatomy*, vol. 23. Cambridge University Press, 1992.

[155] A. K. Harris, P. Wild, D. Stopak, *et al.*, "Silicone rubber substrata: a new wrinkle in the study of cell locomotion," *Science*, vol. 208, no. 4440, pp. 177–179, 1980.

[156] M. Guvendiren and J. A. Burdick, "The control of stem cell morphology and differentiation by hydrogel surface wrinkles," *Biomaterials*, vol. 31, no. 25, pp. 6511–6518, 2010.

[157] S. F. Ahmed, G.-H. Rho, K.-R. Lee, A. Vaziri, and M.-W. Moon, "High aspect ratio wrinkles on a soft polymer," *Soft Matter*, vol. 6, no. 22, pp. 5709–5714, 2010.

[158] T. Okayasu, H.-L. Zhang, D. G. Bucknall, G. A. D. Briggs, *et al.*, "Spontaneous formation of ordered lateral patterns in polymer thin-film structures," *Advanced Functional Materials*, vol. 14, no. 11, pp. 1081–1088, 2004.

[159] D. Terwagne, M. Brojan, and P. M. Reis, "Smart morphable surfaces for aerodynamic drag control," *Advanced Materials*, vol. 26, no. 38, pp. 6608–6611, 2014.

[160] C. M. Stafford, C. Harrison, K. L. Beers, A. Karim, E. J. Amis, M. R. VanLandingham, H.-C. Kim, W. Volksen, R. D. Miller, and E. E. Simonyi, "A buckling-based metrology for measuring the elastic moduli of polymeric thin films," *Nature Materials*, vol. 3, no. 8, pp. 545–550, 2004.

[161] J. Huang, M. Juszkiewicz, W. H. De Jeu, E. Cerda, T. Emrick, N. Menon, and T. P. Russell, "Capillary wrinkling of floating thin polymer films," *Science*, vol. 317, no. 5838, pp. 650–653, 2007.

[162] V. G. Veselago, "The electrodynamics of substances with simultaneously negative values of ϵ and μ," *Soviet Physics Uspekhi*, vol. 10, no. 4, p. 509, 1968.

[163] R. Lakes, "Foam structures with a negative poisson's ratio," *Science*, vol. 235, no. 4792, pp. 1038–1040, 1987.

[164] R. H. Baughman, S. Stafström, C. Cui, and S. O. Dantas, "Materials with negative compressibilities in one or more dimensions," *Science*, vol. 279, no. 5356, pp. 1522–1524, 1998.

[165] T. Mary, J. Evans, T. Vogt, and A. Sleight, "Negative thermal expansion from 0.3 to 1050 kelvin in zrw2o8," *Science*, vol. 272, no. 5258, p. 90, 1996.

[166] B. P. Timko, T. Cohen-Karni, G. Yu, Q. Qing, B. Tian, and C. M. Lieber, "Electrical recording from hearts with flexible nanowire device arrays," *Nano Letters*, vol. 9, no. 2, pp. 914–918, 2009.

[167] J. Viventi, D.-H. Kim, L. Vigeland, E. S. Frechette, J. A. Blanco, Y.-S. Kim, A. E. Avrin, V. R. Tiruvadi, S.-W. Hwang, A. C. Vanleer, *et al.*, "Flexible, foldable, actively multiplexed, high-density electrode array for mapping brain activity in vivo," *Nature Neuroscience*, vol. 14, no. 12, pp. 1599–1605, 2011.

[168] D.-H. Kim, N. Lu, R. Ma, Y.-S. Kim, R.-H. Kim, S. Wang, J. Wu, S. M. Won, H. Tao, A. Islam, *et al.*, "Epidermal electronics," *Science*, vol. 333, no. 6044, pp. 838–843, 2011.

[169] P. Kim, M. Abkarian, and H. A. Stone, "Hierarchical folding of elastic membranes under biaxial compressive stress," *Nature materials*, vol. 10, no. 12, pp. 952–957, 2011.

[170] N. Bowden, S. Brittain, A. G. Evans, J. W. Hutchinson, and G. M. Whitesides, "Spontaneous formation of ordered structures in thin films of metals supported on an elastomeric polymer," *Nature*, vol. 393, no. 6681, pp. 146–149, 1998.

[171] H. Vandeparre, M. Piñeirua, F. Brau, B. Roman, J. Bico, C. Gay, W. Bao, C. N. Lau, P. M. Reis, and P. Damman, "Wrinkling hierarchy in constrained thin sheets from suspended graphene to curtains," *Physical Review Letters*, vol. 106, p. 224301, Jun 2011.

[172] F. Iacopi, S. Brongersma, and K. Maex, "Compressive stress relaxation through buckling of a low-k polymer-thin cap layer system," *Applied Physics Letters*, vol. 82, no. 9, pp. 1380–1382, 2003.

[173] T. R. Hendricks and I. Lee, "Wrinkle-free nanomechanical film: control and prevention of polymer film buckling," *Nano Letters*, vol. 7, no. 2, pp. 372–379, 2007.

[174] T. R. Hendricks, W. Wang, and I. Lee, "Buckling in nanomechanical films," *Soft Matter*, vol. 6, no. 16, pp. 3701–3706, 2010.

[175] B. Tian, J. Liu, T. Dvir, L. Jin, J. H. Tsui, Q. Qing, Z. Suo, R. Langer, D. S. Kohane, and C. M. Lieber, "Macroporous nanowire nanoelectronic scaffolds for synthetic tissues," *Nature Materials*, vol. 11, no. 11, pp. 986–994, 2012.

[176] R. Gatt, L. Mizzi, J. I. Azzopardi, K. M. Azzopardi, D. Attard, A. Casha, J. Briffa, and J. N. Grima, "Hierarchical auxetic mechanical metamaterials," *Scientific Reports*, vol. 5, 2015.

[177] E. Cerda, K. Ravi-Chandar, and L. Mahadevan, "Thin films: Wrinkling of an elastic sheet under tension," *Nature*, vol. 419, no. 6907, pp. 579–580, 2002.

[178] A. Bhaskar. personal communication 2016-10-03.

[179] F. Ursell, "Edge waves on a sloping beach," in *Proceedings of the Royal Society of London A: Mathematical, Physical and Engineering Sciences*, vol. 214, pp. 79–97, The Royal Society, 1952.

[180] D. Evans, "Edge waves over a sloping beach," *The Quarterly Journal of Mechanics and Applied Mathematics*, vol. 42, no. 1, pp. 131–142, 1989.

[181] C. Chapman, "Energy paths in edge waves," *Journal of Fluid Mechanics*, vol. 426, pp. 135–154, 2001.

[182] A. Holst and D. Vassiliev, "Edge resonance in an elastic semi-infinite cylinder," *Applicable Analysis*, vol. 74, no. 3-4, pp. 479–495, 2000.

[183] J. D. Kaplunov, L. Y. Kossovich, and M. V. Wilde, "Free localized vibrations of a semi-infinite cylindrical shell," *The Journal of the Acoustical Society of America*, vol. 107, no. 3, pp. 1383–1393, 2000.

[184] R. Sinclair and R. Stephens, "Velocity dispersion of waves propagating along the edge of a plate," *Acta Acustica united with Acustica*, vol. 24, no. 3, pp. 160–165, 1971.

[185] J. B. Lawrie and J. Kaplunov, "Edge waves and resonance on elastic structures: an overview," *Mathematics and Mechanics of Solids*, vol. 17, no. 1, pp. 4–16, 2012.

[186] W. Wong and S. Pellegrino, "Wrinkled membranes ii: analytical models," *Journal of Mechanics of Materials and Structures*, vol. 1, no. 1, pp. 27–61, 2006.

[187] J. P. Benthem, "A laplace transform method for the solution of semi-infinite and finite strip problems in stress analysis," *The Quarterly Journal of Mechanics and Applied Mathematics*, vol. 16, no. 4, pp. 413–429, 1963.

[188] MatBase, "Matbase," 2016.